

**EXCITON FORMATION DYNAMICS
IN SEMICONDUCTOR QUANTUM WELLS**

by

Sangam Chatterjee

A Dissertation Submitted to the Faculty of the
COMMITTEE ON OPTICAL SCIENCES (GRADUATE)

In Partial Fulfillment of the Requirements
For the Degree of

DOCTOR OF PHILOSOPHY

In the Graduate College

THE UNIVERSITY OF ARIZONA

2003

UMI Number: 3108892

INFORMATION TO USERS

The quality of this reproduction is dependent upon the quality of the copy submitted. Broken or indistinct print, colored or poor quality illustrations and photographs, print bleed-through, substandard margins, and improper alignment can adversely affect reproduction.

In the unlikely event that the author did not send a complete manuscript and there are missing pages, these will be noted. Also, if unauthorized copyright material had to be removed, a note will indicate the deletion.

UMI[®]

UMI Microform 3108892

Copyright 2004 by ProQuest Information and Learning Company.

All rights reserved. This microform edition is protected against unauthorized copying under Title 17, United States Code.

ProQuest Information and Learning Company
300 North Zeeb Road
P.O. Box 1346
Ann Arbor, MI 48106-1346

THE UNIVERSITY OF ARIZONA ®
GRADUATE COLLEGE

As members of the Final Examination Committee, we certify that we have read the dissertation prepared by Sangam Chatterjee entitled Exciton Formation Dynamics in Semiconductor Quantum Wells

and recommend that it be accepted as fulfilling the dissertation requirement for the Degree of Doctor of Philosophy

Hyatt M. Gibbs
Hyatt Gibbs

10-22-03
Date

Rolf Binder

10/22/03
Date

E.M. Wright
Ewan Wright

10/22/03
Date

Date

Date

Final approval and acceptance of this dissertation is contingent upon the candidate's submission of the final copy of the dissertation to the Graduate College.

I hereby certify that I have read this dissertation prepared under my direction and recommend that it be accepted as fulfilling the dissertation requirement.

Hyatt M. Gibbs
Dissertation Director, Hyatt Gibbs

10-23-03
Date

STATEMENT BY AUTHOR

This dissertation has been submitted in partial fulfillment of requirements for an advanced degree at The University of Arizona and is deposited in the University Library to be made available to borrowers under rules of the Library.

Brief quotations from this dissertation are allowable without special permission, provided that accurate acknowledgment of source is made. Requests for permission for extended quotation from or reproduction of this manuscript in whole or in part may be granted by the head of the major department or the Dean of the Graduate College when in his or her judgment the proposed use of the material is in the interests of scholarship. In all other instances, however, permission must be obtained from the author.

SIGNED: 

ACKNOWLEDGEMENTS

It is my pleasure to acknowledge the many people that directly and indirectly helped me manoeuver through the ups and downs of this dissertation.

First, I thank my advisor Hyatt Gibbs for offering me this excellent opportunity to conduct frontier research. In a similar fashion I want to thank Galina Khitrova. Both not only provided challenging problems to study but also the guidance, equipment and world-class samples necessary to succeed.

Claudia Ell has been of great help in discussing and explaining the quite advanced theory involved as well as all other aspects coming up.

This work is the result of a cooperation with Stephan Koch's research group at the Philipps-Universität Marburg. I especially want to thank Walter Hoyer and Mackillo Kira who, with support of many others, modelled many of our experiments.

I also want to thank Heinrich Stolz for experimental support, taking independent data as well as fruitful discussion of the results, and John Prineas for supplying "independent" samples.

Now for my fellow graduate students: Peter Brick introduced me to the pump-probe setup and techniques during the early stages of my research here. The most time I spent with Sorin Mosor and Greg Rupper - discussing experiments, finding sometimes rather creative solutions to experimental challenges and not only as a consequence of the latter just having fun. I want to wish Julian Sweet, Joshua Hendrickson and Benjamin Richards a joyful start and successful research careers. Finally I want to mention Jochen Straub. Though not a member of our group, in any and all optical and mechanical problem he had the answer.

As for my friends here in Tucson, first and foremost I have to thank Jennifer and Tom Davenport for letting me stay at their house for the last few months. And the rest of you for the unforgettable years (in alphabetical order): Alejandra, Alice, Eugenio, Jane, Jennifer, Zac and everybody I forgot: Thank You.

It remains for me to thank all my family for their infinite support.

Für Cosima und Angela

TABLE OF CONTENTS

LIST OF FIGURES	8
LIST OF TABLES	14
LIST OF ABBREVIATIONS	15
ABSTRACT	16
1 INTRODUCTION	18
2 BACKGROUND AND THEORETICAL FUNDAMENTALS . .	21
2.1 Motivation and Background	21
2.2 Theoretical Approach Used for Comparison with the Experiment . .	23
3 SAMPLES AND METHODS OF ANALYSIS	27
3.1 Quantum Well Fundamentals	27
3.2 Sample Selection	30
3.3 Methods of Analysis	34
3.3.1 Carrier Temperature T	34
3.3.2 1s to Continuum Edge Emission Ratio: R	35
3.3.3 β Factor	37
4 EXPERIMENTAL REALIZATION AND SETUP	39
4.1 Absorption	39
4.2 Photoluminescence	44
4.2.1 Photoluminescence with Continuous Wave Excitation	44
4.2.2 Time-Resolved Photoluminescence	45
4.3 Characterization of Excitation Conditions	48

TABLE OF CONTENTS – *Continued*

5	EXPERIMENTAL RESULTS	50
5.1	Absorption Changes after Nonresonant Excitation	50
5.2	Time-Integrated Photoluminescence	54
5.3	Time-Resolved Photoluminescence after Nonresonant Excitation	56
5.3.1	Decay of 1s and Continuum Luminescence	58
5.3.2	Carrier Temperature T and Cooling	63
5.3.3	Ratio 1s to Continuum-Edge Emission: R	65
5.4	β Analysis	69
5.4.1	Density Dependence of β	69
5.5	Dependence on Pump Excess Energy ΔE	74
5.6	Time-Resolved Photoluminescence after Resonant Excitation	76
5.6.1	Decay of 1s and Continuum Luminescence	78
5.6.2	Carrier Temperature T	80
5.6.3	$R(t)$ Analysis	81
5.6.4	β Analysis	83
6	COMPARISON EXPERIMENT - THEORY	85
7	CONCLUSIONS AND OUTLOOK	93
	APPENDIX A. LIST OF DATA	97
	REFERENCES	102

LIST OF FIGURES

2.1 Schematic depiction of the band structure of bulk-GaAs at the Γ -point showing the lowest conduction band (c), heavy-hole (hh), light-hole (lh) and split off (so) valence bands.	22
3.1 Experimental linear absorption spectrum of NMC 5 containing fifty identical 18 nm-wide GaAs quantum wells in between 0.85 nm AlAs and 19 nm $\text{Al}_{0.26}\text{Ga}_{0.74}\text{As}$ barriers, taken at 4 K lattice temperature. . .	28
3.2 Experimental linear absorption spectrum of DBR 42 containing 20 identical 8 nm $\text{In}_{0.06}\text{Ga}_{0.94}\text{As}$ quantum wells (solid) separated by 130 nm GaAs barriers. The absorption of the Wafertech bulk-GaAs substrate under identical conditions is shown dashed for reference. . .	29
3.3 Normalized time-integrated photoluminescence spectra taken with ps excitation. The samples under investigation are (solid lines from top to bottom): DBR 42, DBR 44, DBR 48, DBR 50; their specifications are given in Table 3.1. The curves are offset for clarity. Left: The pump pulse (P) is tuned 8.7 meV energetically above the 1s emission. Right: The pump pulse is set at 1.503 meV. The dashed line shows the emission from the Wafertech bulk-GaAs substrate only. The dotted line shows the photoluminescence of DBR 44 on a piece where the substrate was removed.	31
3.4 Schematic depiction of the definition of derived parameter R . The spectrum shows photoluminescence 1 ns after nonresonant ps excitation 13.2 meV above the exciton resonance for a lattice temperature of 4 K. The estimated carrier density at 1 ns is $2.0 \times 10^{10} \text{ cm}^{-2}$. Dividing the marked data points yields $R(1 \text{ ns}) = 311$	36
3.5 Schematic depiction of the definition of the β -factor. The experimental spectrum (solid) used shows photoluminescence for a lattice temperature of 4 K. It is compared to the KMS result $I_{\text{PL}}^{\text{th, eq}}(\hbar\omega)$ (dashed), i.e. the measured nonlinear αL multiplied by the Boltzmann factor. The photoluminescence is integrated from 0.95 to 1.05 ns after nonresonant ps excitation 13.2 meV above the exciton resonance and with a carrier density $n_{eh} = 4.4 \times 10^8 \text{ cm}^{-2}$	38

LIST OF FIGURES – *Continued*

- 4.1 Schematic drawing of the experimental Setup. The labels are: X, periscope; BS dielectric 90:10 beam splitter; L10, 10 cm lens; L45, 45 cm lens; P polarizer; D variable delay line with multiple passes; S shaker; H hollow retro reflector; L1.5, 1.5 cm lens; W4, quarter wave plate; F, flip mirror; L5, 5 cm lens. 40
- 4.2 Attenuation of the thin film filter introduced in front of the streak camera. The attenuation is specific to each pixel. 46
- 4.3 Spectral response of the streak camera system (S2-ER cathode) on a logarithmic scale. The inset shows the region of interest for the experiments on a linear scale with an expanded energy scale [51]. . . . 47
- 4.4 $\Delta\alpha L$ versus carrier density at 4K. Both carrier density and $\Delta\alpha L$ are shown per quantum well; they are assumed to be the same in each quantum well because pump depletion is negligible. For low carrier densities the curve is extrapolated by linear regression. 48
- 5.1 Top: Nonlinear absorption spectra of DBR42 at 4K lattice temperature for various time delays: The corresponding carrier densities are $2.0 \times 10^{11} \text{ cm}^{-2}$ at 10 ps (dashed) and $2.0 \times 10^{10} \text{ cm}^{-2}$ at 1 ns after nonresonant excitation (dotted). The linear absorption spectrum is shown for comparison (solid). Bottom: Temporal evolution of the peak height for various initial carrier densities: $2.9 \times 10^8 \text{ cm}^{-2}$ (squares), $4.1 \times 10^9 \text{ cm}^{-2}$ (circles), $1.6 \times 10^{10} \text{ cm}^{-2}$ (triangles), $2.9 \times 10^{10} \text{ cm}^{-2}$ (stars), and $2.0 \times 10^{11} \text{ cm}^{-2}$ (pentagons). The lines are guides to the eye. 51
- 5.2 Left: Nonlinear absorption spectra of DBR42 at 4K lattice temperature for short time delays. The initial carrier density is $2.0 \times 10^{11} \text{ cm}^{-2}$. Right: Energetical position of the resonance relative to the peak position of the linear αL versus time for several initial carrier densities: $2.0 \times 10^{11} \text{ cm}^{-2}$ (squares), $1.2 \times 10^{11} \text{ cm}^{-2}$ (circles), $4.0 \times 10^9 \text{ cm}^{-2}$ (triangles), and $1.2 \times 10^9 \text{ cm}^{-2}$ (stars). Note the break in the x-scale. . . . 52
- 5.3 Differential absorption spectra with nonresonant excitation of DBR42 for several time delays. The introduced carrier density is $2.0 \times 10^{11} \text{ cm}^{-2}$. The spectral region -5 meV to -1 meV below the 1s exciton resonance is magnified in the inset. 53
- 5.4 Time-integrated photoluminescence with continuous wave excitation of DBR42 on a semi-logarithmic scale for various excitation power levels. The peak 2.5 meV below the 1s emission is presumed to be impurity emission (c.f. Figure 3.3). 55

LIST OF FIGURES – *Continued*

- 5.5 Experimental photoluminescence spectra on a linear (right) and semi-logarithmic scale (left) for several time delays after nonresonant excitation with an initial carrier density of $9.7 \times 10^9 \text{ cm}^{-2}$ for a lattice temperature of 4 K. The photoluminescence is integrated from $t-0.05 \text{ ns}$ to $t+0.05 \text{ ns}$ for each time step t 57
- 5.6 Temporal evolution of the 1s resonance peak height. The initial carrier densities are (from top to bottom) $2.9 \times 10^8 \text{ cm}^{-2}$, $1.1 \times 10^{10} \text{ cm}^{-2}$, and $1.0 \times 10^{11} \text{ cm}^{-2}$. All data sets are normalized. left: semi-logarithmic scale, data sets are offset by one order of magnitude for clarity. right: linear scale, the data sets are offset for clarity. The lifetimes and peak positions are given in Table 5.2. 59
- 5.7 Temporal evolution of the continuum-edge emission. The data are spectrally integrated from the continuum edge to 0.01 meV above it. The initial carrier densities are (from top to bottom) $2.9 \times 10^8 \text{ cm}^{-2}$, $1.1 \times 10^{10} \text{ cm}^{-2}$, and $1.0 \times 10^{11} \text{ cm}^{-2}$. All data sets are normalized. left: semi-logarithmic scale, data sets are offset by one order of magnitude for clarity. right: linear scale, data sets are offset for clarity. The lifetimes and peak positions are given in Table 5.2. 60
- 5.8 Temporal evolution of the 1s resonance peak height (left) and continuum edge (right) at several lattice temperatures (from top to bottom): 4 K, 30 K, 50 K, 70 K, and 80 K. The initial carrier density is $8.2 \times 10^9 \text{ cm}^{-2}$ for all data sets. The curves are normalized and offset by one order of magnitude for clarity. The decay constants are given in Table 5.3. 62
- 5.9 Temporal evolution of the carrier temperature at a lattice temperature of 4 K. The initial carrier densities are (from top to bottom): $2.0 \times 10^{11} \text{ cm}^{-2}$ (squares), $1.1 \times 10^{10} \text{ cm}^{-2}$ (circles), $7.9 \times 10^8 \text{ cm}^{-2}$ (triangles), and $2.9 \times 10^8 \text{ cm}^{-2}$ (stars). The lines are a guide to the eye. 64
- 5.10 Temporal evolution of the carrier temperature for five different lattice temperatures: 80 K (pentagons) 70 K (stars), 50 K (triangles), 30 K (circles), and 4 K (squares). The initial carrier density for all measurements is $8.2 \times 10^9 \text{ cm}^{-2}$ 65
- 5.11 Temporal evolution of the ratio of 1s to continuum emission edge R for 4 K lattice temperature on a semi-logarithmic scale. The initial carrier densities are $2.0 \times 10^{11} \text{ cm}^{-2}$ (squares), $1.1 \times 10^{10} \text{ cm}^{-2}$ (circles), and $2.9 \times 10^8 \text{ cm}^{-2}$ (triangles). The inset shows the same data on a double-logarithmic scale. 66

LIST OF FIGURES – *Continued*

- 5.12 Temporal evolution of R for higher lattice temperatures: 30 K (bottom), 50 K (middle), and 80 K (top). The graphs show the densities on a semi-logarithmic scale, the insets on a double-logarithmic scale. Note the varying x- and y-scales for each lattice temperature. The carrier densities are given in the corresponding legends in cm^{-2} 68
- 5.13 β factor versus carrier density for different lattice temperatures on a double-logarithmic scale (from top to bottom): 50 K, 30 K, and 4 K. The data set at 4 K contains data points taken 1 ns after nonresonant excitation; the others have data points at various time delays. . . . 70
- 5.14 Temporal evolution of β for 4 different initial carrier densities: $2.0 \times 10^{11} \text{ cm}^{-2}$ (pentagons), $1.1 \times 10^{10} \text{ cm}^{-2}$ (triangles), $7.9 \times 10^8 \text{ cm}^{-2}$ (diamonds), and $2.9 \times 10^8 \text{ cm}^{-2}$ (stars). . . . 72
- 5.15 Low density behavior for β with $T=4$ K. The dashed line shows a linear regression through the 1 ns values (squares). For three initial carrier densities, $7.9 \times 10^8 \text{ cm}^{-2}$ (rhombi), $4.1 \times 10^8 \text{ cm}^{-2}$ (circles), and $2.9 \times 10^8 \text{ cm}^{-2}$ (stars), data points for delay times longer than 1 ns are shown. . . . 73
- 5.16 β versus carrier density for 50 K lattice temperature. Values for all different time delays are shown. . . . 74
- 5.17 Carrier temperature (top) and β factor (bottom) versus time for 4 K lattice temperature. The pump energies are 8.8 meV (squares), 24.3 meV (circles), and 32.2 meV (triangles), the calculated initial carrier density in all cases is $1.2 \times 10^{10} \text{ cm}^{-2}$ 75
- 5.18 Photoluminescence spectra after resonant excitation for several time delays at a lattice temperature of 4 K. The initial carrier density is $1.0 \times 10^{10} \text{ cm}^{-2}$ 77
- 5.19 Temporal evolution of the 1s resonance peak height (left) and continuum edge (right) at several lattice temperatures after resonant excitation (from top to bottom): 30 K, 15 K, and 4 K. The initial carrier density is $1.0 \times 10^{10} \text{ cm}^{-2}$ for all data sets. The curves are normalized and offset by one order of magnitude for clarity. The decay constants of the second, slower decay are given in Table 5.4. . . . 79
- 5.20 Temporal evolution of carrier temperature T after resonant excitation for an initial carrier density of $1.0 \times 10^{10} \text{ cm}^{-2}$ and three different lattice temperature: 4 K (squares), 15 K (circles), and 30 K (triangles). . . . 81

LIST OF FIGURES – *Continued*

- 5.21 Temporal evolution of 1s to continuum emission edge ratio $R(t)$ after resonant excitation for an initial carrier density of $1.0 \times 10^{10} \text{ cm}^{-2}$ and three different lattice temperature: 4 K (squares), 15 K (circles), and 30 K (triangles) on a semi-logarithmic scale. Inset: same on double-logarithmic scale. 82
- 5.22 Temporal evolution of β after resonant excitation for an initial carrier density of $1.0 \times 10^{10} \text{ cm}^{-2}$ and three different lattice temperature: 4 K (squares), 15 K (circles), and 30 K (triangles). 83
- 6.1 β versus carrier density. Full squares refer to experimental values taken at 1 ns after nonresonant excitation at a lattice temperature of 4 K. The densities refer to densities at 1 ns. The theoretical values (dotted line) are calculated using the PL formula (2.4) for a pure e-h plasma with a carrier temperature of (16 ± 2) K. Top: same for 50 K lattice temperature, but data points for all time delays are shown. The density for each time step is calculated according to Chapter 4.3. The extracted e-h plasma temperature is (50 ± 2) K; the theoretical curves are computed for a carrier temperature of 48 K. 86
- 6.2 Theoretical photoluminescence spectra for two carrier densities ($5.0 \times 10^8 \text{ cm}^{-2}$, top and $1.3 \times 10^{10} \text{ cm}^{-2}$, bottom) and a carrier temperature of 16 K: pure plasma (dotted) and including excitons (solid). The exciton contributions used are as shown in Figure 6.4. The KMS result (dashed) is obtained by multiplying the computed nonlinear αL by the Boltzmann factor. 88
- 6.3 β versus carrier density. As in Figure 6.1, the full squares refer to experimental values taken at 1 ns after nonresonant excitation at a lattice temperature of 4 K and the densities refer to densities at 1 ns. The solid line shows a theoretical fit including a $q = 0$ exciton contribution shown in the inset. Top: same for 50 K lattice temperature and extracted e-h plasma temperature of 50 ± 2 K; the theoretical curves are computed for a carrier temperature of 48 K. 88
- 6.4 Top: Phase diagram of $q = 0$ excitonic contributions as a function of the carrier density on a double-logarithmic scale as used in the fit curve shown in Figure 6.3. Bottom: Phase diagram of bright excitons with $q < q_{\text{photon}}^{\text{max}}$ as a function of the carrier density on a double-logarithmic scale as used in the fit curve shown in Figure 6.3 extracted from $\Delta N_X(q = 0)$ and Equation 6.2. 89

LIST OF FIGURES – *Continued*

- 6.5 Possible distribution functions for excitons. The value of $N_X(q)$ given in Figure 6.4 corresponds to the y-axis crossing of the distribution. No hole burning (solid); hole burning down to 10% (dashed). 91
- 7.1 Factor β versus carrier density. Full squares refer to experimental values taken at 1 ns after nonresonant excitation at a lattice temperature of 4 K. The densities refer to densities at 1 ns. The theoretical values (dotted line) are calculated using pure e-h plasma theory with carrier temperatures of 14 K for small and 18 K for elevated carrier densities. The solid line shows a theoretical fit using the luminescence formula 2.4 including a $q = 0$ exciton contribution as shown in the inset. Top: the same for 50 K lattice temperature, but data points for all time delays are shown. The extracted e-h plasma temperature is (50 ± 2) K; the theoretical curves are computed for a carrier temperature of 48 K. Inset: Phase diagram of $q = 0$ excitonic contributions as a function of the carrier density. 94

LIST OF TABLES

3.1	Parameters of samples shown in Figure 3.3	31
4.1	Typical polarizer settings	43
5.1	Approximate β of 1s emission with CW excitation	56
5.2	Photoluminescence lifetimes and time delays of the peaks of the 1s and continuum-edge emission for several initial carrier densities at 4 K lattice temperature, extracted from the time traces shown in Figure 5.6 and Figure 5.7.	60
5.3	Photoluminescence lifetime and time delay for the respective peak of the 1s and continuum-edge emission lifetime for several lattice temperatures, extracted from the time traces shown in Figure 5.8.	62
5.4	Photoluminescence lifetimes of the 1s and continuum-edge emission after resonant excitation for several lattice temperatures, extracted from the time traces shown in Figure 5.19.	79

LIST OF ABBREVIATIONS

MBE:	molecular beam epitaxy
GaAs:	gallium arsenide
AlGaAs:	aluminium gallium arsenide
InGaAs:	indium gallium arsenide
Si:	silicon
MQW:	multiple quantum well
SQW:	single quantum well
PL:	photoluminescence
LO:	longitudinal optical
AR:	anti-reflection
FWHM:	full width at half maximum
CW:	continuous wave
EOM:	electro-optic modulator
ADP:	ammonium dihydrogen phosphate ($\text{NH}_4\text{H}_2\text{PO}_4$)
NA:	numerical aperture
F/#:	F-number
CCD:	charge-coupled device
KMS:	Kubo-Martin-Schwinger
MHz:	Megahertz = 10^6 s^{-1}
THz:	Terahertz = 10^{12} s^{-1}
μm :	micrometer = 10^{-6} m
nm:	nanometer = 10^{-9} m
ns:	nanosecond = 10^{-9} s
ps:	picosecond = 10^{-12} s
fs:	femtosecond = 10^{-15} s

ABSTRACT

Photoluminescence from direct-bandgap semiconductor quantum wells after non-resonant excitation is predominantly observed at energetic position of the 1s exciton resonance. The time evolution of the photoluminescence is generally interpreted as direct monitor of an excitonic population; a rise of the signal is interpreted as a buildup and the decrease as decay of the excitonic population. Recent microscopic calculations, however, have shown that even without an incoherent excitonic population, pure plasma decay yields photoluminescence peaked at the 1s exciton resonance.

Experimental time-resolved photoluminescence spectra are taken across a large region of the parameter space of carrier density and lattice temperature. They are compared to the expected thermal equilibrium spectra, calculated from nonlinear absorption measurements taken under identical conditions. Under none of the experimentally explored parameters is the 1s emission as bright as expected for thermal equilibrium.

To distinguish excitonic and plasma contributions, the deviations from thermal equilibrium at the 1s exciton resonance are then analyzed using a microscopic calculation. The dipole moment is adjusted to reproduce the excitonic binding energy and oscillator strength of the samples under investigation. The carrier densities and carrier temperatures are determined experimentally; no free fit parameters are necessary.

The differences between experimental values and pure plasma calculation are explained with the presence of an incoherent excitonic population. Although at first the emission spectra under all conditions do not vary significantly, a more detailed analysis reveals that the sources of the photoluminescence can be either predominantly excitonic or plasma. For low temperatures and low densities the excitonic emission is extremely sensitive to even minute exciton populations making it possible to extract

a phase diagram for incoherent excitonic populations. The maximum contribution of bright excitons is found at intermediate densities and low lattice temperatures; the absolute number of bright excitons is tiny, less than 0.04% of the total carrier density. However, it is not possible to determine the total number of bright and dark exciton by using photoluminescence.

CHAPTER 1

INTRODUCTION

Almost a century ago, Wolfgang Pauli was said to have contemplated already if semiconductors do exist and whether it would be lucrative at all to work in this field. Nowadays it is hardly possible to imagine how a life without the consequences of the then fundamental research would look like.

Semiconductor optics is an important subdivision of semiconductor physics. Developments in this sector become increasingly important and have brought inventions like light emitting diodes (LED's) and semiconductor lasers into everyday life. The trend in applied research of optical and electronic components seemingly unstoppably goes towards the smaller and the faster, more and more approaching the quantum optical limit. The simultaneous development of ultrafast laser systems has enabled the observations of quantum mechanical processes on sub-picosecond time scales [1] and lately even beyond that limit – in the single cycle regime [2].

More and more sophisticated theoretical descriptions are necessary and being developed to explain these phenomena, made possible at least in part by the ever increasing computational capacities due to more advanced microelectronics – and hence closing the cycle.

The existence of attractive Coulomb interaction leads to the formation of an atom-like series of bound states for an electron-hole pair in semiconductors [3]. These pair states are also known as excitons. Due to the large excitonic binding energy in II-VI semiconductors [4], they can easily be resolved even at room temperature [5].

Accordingly in III-V based semiconductor systems, excitonic resonances cannot be observed as easily due to the smaller excitonic binding energy. In two dimensional systems, the quantum wells, however, the excitonic binding energy is increased [4], and they can be detected in absorption even for room temperature [6, 7].

Traditionally, photoluminescence at the spectral position of the 1s exciton resonance was considered as evidence for the presence of an excitonic population. While the rise of the 1s photoluminescence after nonresonant excitation of a semiconductor was interpreted as its buildup [8, 9, 10, 11, 12, 13, 14], the photoluminescence decay was attributed to exciton recombination [15, 16]. However, recently a microscopic theory predicted that photoluminescence at the 1s exciton resonance does not require excitonic populations but can be due to plasma emission only [17]. As a direct consequence, this means that luminescence at the spectral position of the 1s resonance does not necessarily prove the existence of excitons, and previous interpretations may be in question.

The goal of this dissertation is to reexamine what contributes to the PL emitted at the 1s exciton resonance. The approach chosen to achieve this is to examine the spectral shape of photoluminescence. Therefore it is to take photoluminescence and absorption measurements under identical conditions. For nonresonant picosecond excitation, the parameter space of carrier density and lattice temperature is explored. Results for nonresonant excitation energetically above the 1s exciton resonance are compared to resonant excitation data. A microscopic theory is used for analysis. This way a region where excitonic contributions are present is identified, while plasma emission dominates some of the parameter space. It is further shown that small excitonic populations can dominate the 1s photoluminescence.

This dissertation is organized as follows: In Chapter 2 previous experiments and their interpretation are reviewed, and recent theoretical developments and related experiments are outlined offering new perspectives at exciton dynamics. After a brief look at fundamentals of semiconductor quantum wells, the sample selection criteria and process are covered, and methods of data analysis are introduced in Chapter 3. Then in Chapter 4, the necessary experimental techniques and the resulting setup for this study are explained. An overview of the acquired data is presented in the following chapter; a detailed list can be found in Appendix A. Chapter 5 also gives a first analysis by applying the techniques introduced in Chapter 3. A detailed comparison

of the experimental results with a microscopic theory is given in Chapter 6. Finally the findings are summarized, and future experimental possibilities are shown.

CHAPTER 2

BACKGROUND AND THEORETICAL FUNDAMENTALS

2.1 Motivation and Background

The linear and nonlinear optical properties of semiconductors are strongly affected by excitonic effects in the spectral region close to the fundamental energy gap. The band structure near the Γ -point is shown schematically in Figure 2.1. In particular near the band edge, the absorption spectrum reveals the effects of attractive Coulomb interaction of electron and hole by showing a hydrogen-like series of discrete transition lines below the actual bandgap as well as Coulomb enhancement of the band to band transition edge.

Although an exciton is often regarded as analogous to the hydrogen atom, there is a fundamental difference: In semiconductors, the exciton is created by optical excitation. This causes a finite lifetime; in GaAs based quantum well systems typically the radiative lifetime of 1s excitons is ≈ 13 ps [18] at low temperatures. Optical spectroscopy on atoms typically probes the transitions of electrons between different excited states of an atom. The equivalent in semiconductor systems is spectroscopy between the different excitonic states. The transition energies in semiconductors are much smaller, energetically in the far infrared, or THz regime.

Following the suggestion of Kira et al. [17], such THz measurements [19, 20, 21, 22, 23] have been used to directly monitor exciton formation by observing the build-up of the induced absorption corresponding to the excitonic 1s to 2p transition. These experiments give direct evidence for excitonic populations with formation times on a rather slow time scale of hundreds of picoseconds to nanoseconds. Initially a relatively flat, broadband response is triggered by the continuum. Subsequently over the next several hundreds of picoseconds, a resonance develops, giving a clear indication of the

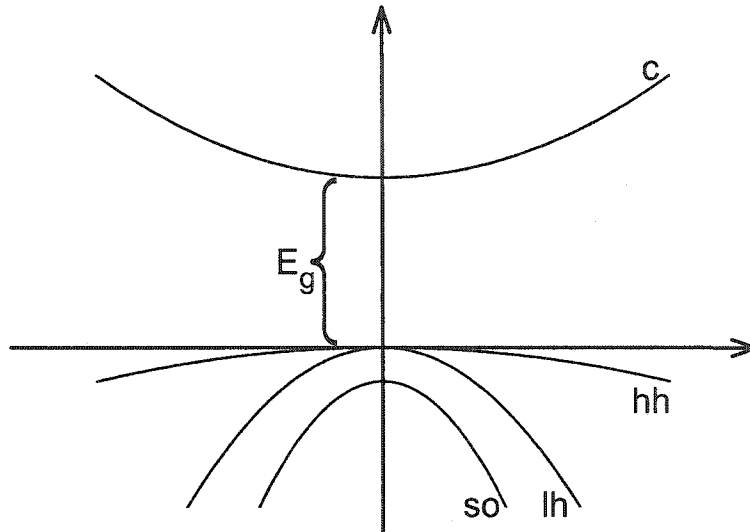


Figure 2.1: Schematic depiction of the band structure of bulk-GaAs at the Γ -point showing the lowest conduction band (c), heavy-hole (hh), light-hole (lh) and split off (so) valence bands.

presence of excitons. However, other recent experiments on THz absorption reported only very small exciton formation rates [24]. Only small changes in the THz signal are observed after nonresonant excitation. Photoluminescence at the 1s resonance, collected after similar nonresonant ps excitation on the same sample, still increases for the investigated time delay. Hence, there is evidence for exciton formation after nonresonant excitation, but the formation times seem to be rather long. This gives a first indication that the photoluminescence dynamics may not track the exciton dynamics.

Also in contradiction to previous interpretations, nonresonantly excited time-resolved photoluminescence measurements show that for 100 K lattice temperature, photoluminescence at the 1s resonance is already developed only a few hundred femtoseconds after nonresonant excitation [25], much faster than any expected exciton formation time. The 1s photoluminescence typically increases during the first hundreds of picoseconds and subsequently decays over several nanoseconds. This is

again in contradiction to THz observations which if at all indicate a formation time of about a nanosecond. Hence, the questions remain if and how excitonic populations influence the photoluminescence, and how to explain the photoluminescence dynamics on this long time scale.

2.2 Theoretical Approach Used for Comparison with the Experiment

The calculations necessary for the comparison of theoretical results and the experiments shown in this dissertation were performed by Dr. Walter Hoyer, Prof. Mackillo Kira, and Prof. S. W. Koch in his group at the Philipps-Universität Marburg, Germany. Here a brief introduction into the utilized formalism is presented. A detailed derivation and explanation of the calculations can be found in [26].

The complex band structure of semiconductors always forces the application of approximations. The easiest and for most practical purposes sufficient approximation is the parabolic (effective mass) approximation of the lowest conduction and highest valence band in the vicinity of the Γ -point. This is applied for the calculations used for comparison with the experiment; the effective masses however are determined in a full $\mathbf{k}\cdot\mathbf{p}$ computation.

Classically, light-matter interaction is described by the Maxwell equation

$$\nabla^2 E - \left(\frac{n}{c}\right)^2 \frac{\partial^2 E}{\partial t^2} = \mu_0 \frac{\partial^2 P}{\partial t^2}, \quad (2.1)$$

and the material response by the polarization

$$P = \sum_k d_{cv}^* p_k + c.c. \quad (2.2)$$

where $p_k = \langle a_{v,k}^\dagger a_{c,k} \rangle$. Here $a_{c,k}$ and $a_{v,k}$ are the annihilation operators of an electron in the conduction and valence band, respectively. Using the Heisenberg equation of motion to derive the equations of motion for the polarization and the carrier distribution functions f_e and f_h for electrons and holes, respectively, yields the semiconductor Bloch equations. They can be seen as an extension of the optical Bloch equations

to systems with Coulomb interaction. They can also be derived using nonequilibrium Green's functions [27] or quantum mechanical projection operators [3]. From the semiconductor Bloch equations, the response of the system to a classical light field is determined. The thus calculated absorption is used as a cross-check for the experimental pump-probe results.

The emission properties of a semiconductor are described using semiconductor luminescence equations [28, 29]. It is again based on Bloch valence and conduction band electrons and their attractive Coulomb interaction; the interaction with phonons is also included. Additionally, the light field is described in second quantization

$$\hat{E} = \sum_{\mathbf{q}} i \varepsilon_{\mathbf{q}} \mathbf{U}_{\mathbf{q}}(\mathbf{r}) \hat{B}_{\mathbf{q}}^{\dagger} + h.c. . \quad (2.3)$$

Here $\varepsilon_{\mathbf{q}} = \sqrt{\frac{\hbar\omega_{\mathbf{q}}}{2\varepsilon_0}}$ is the vacuum field strength with the background dielectric constant ε_0 ; $\mathbf{U}_{\mathbf{q}}(\mathbf{r})$ are plane waves, and $\hat{B}_{\mathbf{q}}^{\dagger}$ is the creation operator of a photon in state q . Applying the Heisenberg equations of motion technique then yields the semiconductor luminescence equations. In the computations, no inhomogeneous broadening is considered.

Recently [17], it has been shown that luminescence at the exciton energy occurs even in Hartree-Fock approximation, i.e. without an excitonic population included in the theory. Meanwhile the theory has been extended to include further higher-order electron-hole correlations, combining the advantage of including the full Fermionic symmetry of the underlying electrons and holes with the possibility to describe correlated electron-hole plasmas [30] and the formation of excitons [31].

The quasi-steady-state photoluminescence is then given by $I_{\text{PL}}(\omega) \equiv \frac{\partial}{\partial t} \langle B^{\dagger} B \rangle$. The equations of motion for $\langle B^{\dagger} B \rangle$ couple to the photon-assisted polarization $\langle B^{\dagger} a_{\mathbf{v}}^{\dagger} a_{\mathbf{c}} \rangle$. The fully dynamic solution including incoherent exciton formation with arbitrary center-of-mass momentum and exciton-phonon-coupling is only possible for one-dimensional systems (quantum wires) with current computer resources. Here, in order to compute results for quantum wells, the fact that the carrier system changes

slowly with carrier density and temperature is used such that an adiabatic solution of the photon assisted polarizations is justified. In this limit, the quasi-steady-state luminescence spectrum is obtained from

$$I_{\text{PL}}(\omega) \propto \frac{|d_{\text{cv}}^2| \omega}{\varepsilon_{\text{bg}}} \text{Im} \left[\sum_{\nu} \frac{\phi_{\nu}^r(r=0)}{E_{\nu} - \hbar\omega - i\gamma_{\nu}} \sum_{k,k'} (\phi_{\nu}^l(k))^* \langle a_{c,k'}^{\dagger} a_{c,k} a_{v,k'} a_{v,k}^{\dagger} \rangle \right], \quad (2.4)$$

by introducing an excitonic basis for the photon-assisted polarization. The prefactor in Equation (2.4) is determined by the square of the dipole matrix element $|d_{\text{cv}}|^2$ and the background dielectric constant ε_{bg} . The calculations are performed for finite quantum well widths and infinite barrier heights. The effective well width is adjusted such that the calculations reproduce the experimentally measured exciton binding energy. Using $\mathbf{k} \cdot \mathbf{p}$ theory, $m_h/m_e = 3$ is determined. The other material parameters cancel out of the β analysis used in this dissertation; see Section 3.3.3 and Chapter 6. The exciton basis is not the usual low-density exciton basis, but includes also the phase-space filling factor and the scattering from excitation induced dephasing [32, 30]. Both the eigenenergies E_{ν} and the broadenings γ_{ν} are frequency dependent. Therefore, the scattering rates are also frequency dependent and computed such that the exciton basis functions, energies and relaxation rates differ from frequency to frequency.

The energy denominator in Equation (2.4) shows that the emission is always peaked at the excitonic energies, regardless whether the source term $\langle a_{c,k'}^{\dagger} a_{c,k} a_{v,k'} a_{v,k}^{\dagger} \rangle$ describes true excitons and/or a correlated plasma. This four-operator expectation value contains a single-particle contribution $\delta_{k,k'} f_k^e f_k^h$, which leads to non-vanishing luminescence as soon as electrons and holes are excited in the quantum well.

In order to get the full luminescence spectrum, the remaining correlated part of the source including Coulomb scattering is also computed. In this approach, all scattering processes which do not mix different center-of-mass momenta are included on a second-Born level for electron-hole correlations. This way the pure plasma emission of a correlated electron-hole plasma is obtained. Results of these computations are shown later in Figure 6.2.

To get a better understanding of Equation 2.4, it can be further simplified by approximating the microscopic scattering of photon assisted polarizations and electron-hole correlations by a simple decay constant γ . This approximation is however only valid in the ultra-low-density case. The equation for the four-point correlations can then be solved in the same exciton basis as the photon-assisted polarization, yielding this simplified luminescence description:

$$I_{\text{PL}}(\omega) \propto \frac{|d_{\text{cv}}^2| \omega}{\varepsilon_{\text{bg}}} \text{Im} \left[\sum_{\nu} \frac{|\phi_{\nu}(r=0)|^2}{\hbar\omega - E_{\nu} + i\gamma} (\langle N_{\nu} \rangle_{\text{HF}} + \Delta \langle N_{\nu} \rangle) \right] \quad (2.5)$$

with the Hartree-Fock exciton number $\langle N_{\nu} \rangle_{\text{HF}} = \sum_k |\phi_{\nu}(k)|^2 f_k^e f_k^h$ and in addition possible excitons $\Delta \langle N_{\nu} \rangle$. Equation (2.5) is reminiscent of the famous Elliott formula for bandgap absorption [33]:

$$\alpha(\omega) \propto |d_{\text{cv}}^2| \text{Im} \left[\sum_{\nu} \frac{|\phi_{\nu}(r=0)|^2}{\hbar\omega - E_{\nu} + i\gamma} + \Theta(\omega) \right]. \quad (2.6)$$

$\Theta(\omega)$ describes continuum contributions to the absorption. Both formulae contain a sum over excitonic states which shows that luminescence peaks at the same excitonic energies as the absorption. In contrast to absorption, however, the strength of the photoluminescence is not only determined by the exciton dipole moment $d_{\text{cv}}^2 |\phi_{\nu}(r=0)|^2$ but also by the occupation number $\langle N_{\nu} \rangle_{\text{HF}} + \Delta \langle N_{\nu} \rangle$.

CHAPTER 3

SAMPLES AND METHODS OF ANALYSIS

3.1 Quantum Well Fundamentals

From the second half of the last century, GaAs-based semiconductors played an important role in the advances of micro-electronics, computers and other “high-tech” devices. The next milestone in semiconductor technology was the invention of precise growth technologies such as MBE, allowing for controlled depositions of thin layers of material with accuracy down to a single atomic monolayer. This led to the development of layered structures such as quantum wells.

Two main semiconductor materials are used for GaAs based quantum well structures. To take advantage of the almost identical lattice constants, a thin GaAs well, on the order of a few nanometer thickness, is sandwiched between AlGaAs or AlAs barriers. The 1s transition energy is dependent on the thickness of the GaAs quantum well. A smaller well thickness shifts the 1s resonance to a higher energy. Thick quantum wells act bulk-like; with increasing size, the quantum well resonances are shifted towards, and ultimately overlap, the absorption of the bulk substrate the sample is grown on.

The oscillator strength of the 1s exciton, in the case of an ideal system, that is without any disorder, is $\propto |d_{cv}|^2 |\phi(r=0)|^2$, where d_{cv} is the dipole moment and $\phi(r=0)$ the respective wave function at $r=0$. In this case the line is purely homogeneously broadened. In real systems however, disorder is present, and for most samples even dominant.

For thin wells, the linewidth is limited by interface fluctuations causing localization of electrons and holes. These localized excitonic states have slightly different energies, depending on their respective sizes and depths. The resulting splitting of the resonance can be observed in high-resolution low-intensity photoluminescence

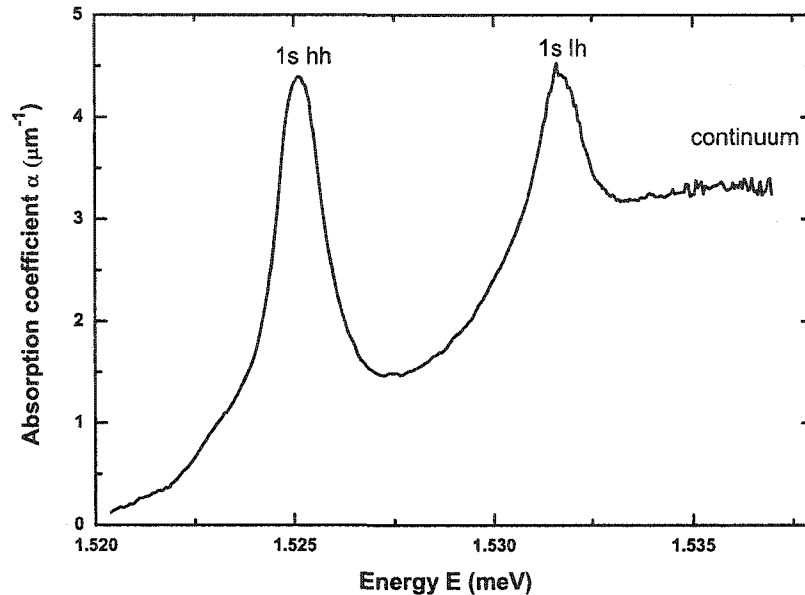


Figure 3.1: Experimental linear absorption spectrum of NMC5 containing fifty identical 18nm-wide GaAs quantum wells in between 0.85nm AlAs and 19nm $\text{Al}_{0.26}\text{Ga}_{0.74}\text{As}$ barriers, taken at 4 K lattice temperature.

experiments [34] as well as in transmission measurements [35]. The emission is often observed to come predominantly from lower energetic states, energetically below where the main oscillator strength lies [36, 37]. Thicker well sizes typically do not show this behavior because the energetical separation of the monolayers becomes negligible. They can show very narrow absorption lines [38].

Due to substrate absorption, GaAs samples either make it necessary to remove the substrate, which typically broadens the absorption line [39, 40], or to work in reflection. In addition GaAs quantum wells have a small heavy-hole–light-hole splitting; see Figure 3.1. This makes it virtually impossible to detect the heavy-hole continuum emission without distortion as needed to determine the plasma temperature; c.f. Chapter 4.2.

Alternatively a small fraction of indium can be added to several monolayers of GaAs to form an InGaAs quantum well, typically of 8 nm thickness, in between GaAs barriers [39, 40]. The lattice mismatch created by introduction of the indium atoms

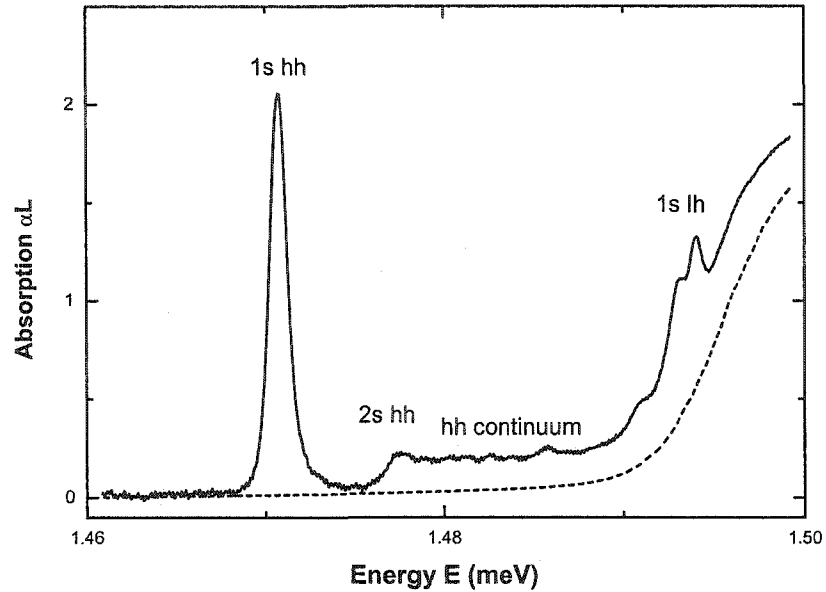


Figure 3.2: Experimental linear absorption spectrum of DBR 42 containing 20 identical 8 nm $\text{In}_{0.06}\text{Ga}_{0.94}\text{As}$ quantum wells (solid) separated by 130 nm GaAs barriers. The absorption of the Wafertech bulk-GaAs substrate under identical conditions is shown dashed for reference.

into the lattice, introduces strain into the sample. This increases the heavy-hole–light-hole splitting to a much larger value than for GaAs quantum wells; therefore continuum emission can be detected undistorted over several meV; see Figure 3.2. The lower band edge of the indium compound shifts the 1s resonance of InGaAs quantum wells to lower energies, below the bulk-GaAs absorption. The indium concentration and thickness of the well determine the energetic position of the resonances [39, 40]. This enables the growth of a sample suited for photoluminescence experiments. Another advantage of InGaAs-based quantum wells is the possibility to work in transmission geometry; the residual substrate absorption is typically negligible or small and smooth enough to be easily measured and subtracted (Figure 3.2).

3.2 Sample Selection

All samples in the experiments presented in this dissertation are MBE-grown on semi-insulating, undoped [100]-oriented GaAs substrates from Wafertech using a Riber 32P system. During growth, the samples were mounted indium free; all substrates were rotated during the deposition process, thus yielding a radially symmetric thickness variation across the sample. The samples were chosen not to show pronounced light-coupling effects [41, 42, 43, 44]; they are typically grown thicker than Bragg spacing at growth center. When the wells are separated by barriers of exactly $\lambda/2$, where λ is the wavelength in the medium, the samples satisfy the Bragg spacing, exhibiting strongest constructive light coupling. Sample pieces close to growth center were chosen, because of their superior quality and homogeneity. Two samples, 1a1124 and 1a1125, were grown in a different MBE system and used as a cross check to exclude sample and machine specific effects.

It is preferable, for reflection and transmission measurements, to use samples with as narrow as possible linewidth - unless of course in disorder studies. The situation for photoluminescence measurements is somewhat different. While narrow linewidth and large oscillator strength of the exciton resonances are still desirable, additional requirements come into play. Though having very low oscillator strength and thus hardly ever distorting absorption measurements, impurities usually have distinct signatures in emission. Both their spectral features as well as their time evolution can distort the actual quantum well photoluminescence under investigation.

Figure 3.3 shows typical emission spectra of several candidate samples. The photoluminescence is collected time-integrated; c.f. Section 4.2. On the left hand side the samples are pumped $\Delta E = 8.7$ meV energetically above the 1s exciton resonance using a 3 ps pulse at 80 MHz repetition rate. The spectra on the right hand side are taken similarly, but the excitation pulse is kept at 1.5029 eV.

All unetched samples show very pronounced impurity emission at 1.4920 eV. This is the dominant impurity contribution to all spectra pumped above this energy; see the right hand side of Figure 3.3. However, it cannot be seen in the dotted curve

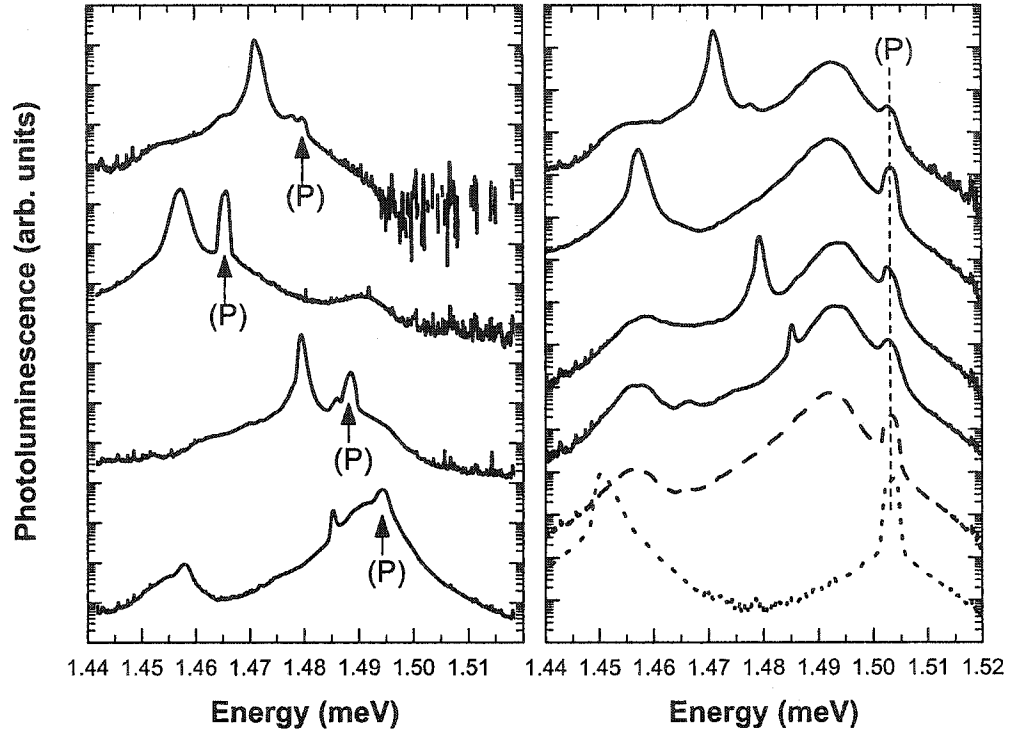


Figure 3.3: Normalized time-integrated photoluminescence spectra taken with ps excitation. The samples under investigation are (solid lines from top to bottom): DBR 42, DBR 44, DBR 48, DBR 50; their specifications are given in Table 3.1. The curves are offset for clarity. Left: The pump pulse (P) is tuned 8.7 meV energetically above the 1s emission. Right: The pump pulse is set at 1.503 meV. The dashed line shows the emission from the Wafertech bulk-GaAs substrate only. The dotted line shows the photoluminescence of DBR 44 on a piece where the substrate was removed.

sample	# of wells	1s energy (eV) at 4 K	substrate removed
DBR 42	20	1.471	no
DBR 44	2	1.4569	yes
DBR 48	4	1.4795	no
DBR 50	4	1.4848	no

Table 3.1: Parameters of samples shown in Figure 3.3

showing photoluminescence from DBR 44. This sample consists of two InGaAs quantum wells grown with an AlAs etch stop. The substrate on one piece was removed by selective chemical etching. This allows to distinguish whether emission from impurities emanates from the bulk substrate or from traps in the MBE-grown material. The pump for this measurement was also tuned to 1.503 meV. The broad wings down two orders of magnitude below the peak of the scattered pump light are the tails of the pump spectrum itself. Consequently, the impurity at 1.4920 eV must come primarily from the substrate only. By its emission energy, it is identified as carbon. Unwanted carbon contaminates the bulk-GaAs substrates during the manufacturing process; i.e. it is present in substrates specified as “undoped”. Currently, substrates that do not show this signature are not available. The carbon doping emission distorts the quantum wells photoluminescence if the 1s transition energy lies nearby.

Hence it is necessary to avoid the carbon doping emission, if the substrate is not removed. Substrate removal usually broadens the exciton resonances and degrades the surface quality, since chemically etched surfaces are not as smooth as MBE-grown ones.

As a consequence of the above findings, the 1s resonance energy is tailored to meet the above requirement. For samples with very low indium concentration, the linewidths are typically very much narrower. While introducing fewer of the lattice-mismatched indium atoms reduces the strain, it also reduces the heavy-hole light-hole splitting. Also for these samples, the heavy-hole continuum already lies completely on top of the low energy tail of the bulk-GaAs substrate absorption. This forces the sample to be mounted with the substrate towards the detection lens, to ensure that the pump light is not absorbed in the substrate and reaches the wells; this is necessary for a meaningful absolute density calibration. The photoluminescence then has to be corrected using the absorption in order to measure its correct spectral dependence.

From the above, it can be concluded that the carbon impurity determines the upper limit of the much weaker continuum emission and pump energy. Other impurity states are observed at 1.4552 eV and 1.4655 eV; the latter is not present in the grown material. The 1s emission wavelength should therefore be at about 1.477 eV or above. Such a sample allows several meV of continuum emission to be detected undistorted from “unwanted” impurity emission. The lower energy tail of the substrate absorption is negligible below 1.4884 eV (Figure 3.2). However the detector quantum efficiency (Figure 4.3) and tuning range of the fs-laser give an upper limit of about 1.459 eV. Increasing the indium concentration from 0.04 or less to 0.06 shifts the 1s resonance to the most favorable energy region; the tradeoff is an almost double absorption linewidth (FWHM) due to increased disorder.

The principal sample (DBR42) consists of twenty $\text{In}_{0.06}\text{Ga}_{0.94}\text{As}$ quantum wells. Each is 8 nm thick and grown in between 130 nm GaAs barriers. A typical absorption spectrum is shown in Figure 3.2. The indium concentration and well thickness are chosen to place the 1s exciton resonance at 1.471 eV at 4 K lattice temperature; its exciton linewidth is 0.96 meV full width at half maximum. This sample permits the detection of about 13 meV of emission above the 1s resonance, undistorted by substrate absorption and impurities. At the same time the 1s transition energy is high enough to work well within the operating range of laser and detector.

Both sides of the sample were anti-reflection coated to reduce Fabry-Pérot interference fringes. The AR-coating was designed to eliminate the reflectivity of the sample. When the reflection signal from the sample is negligibly small, it is possible to extract the absorption from the transmitted signal through the sample only; see Section 4.1. This is experimentally desirable; it requires one less measurement. Another advantage of AR-coatings is reduced scatter of pump and probe light from the front surface of the sample. When an AR-coating is applied, the physical roughness ρ of the air-semiconductor interface stays the same. The refractive index $n > 1$ of the AR-coating, however, reduces the effective roughness to ρ/n .

When the applied coating does not reduce the reflectivity enough to completely eliminate the Fabry-Pérot fringes or when no AR-coating is used, the visibility of the fringes can be reduced by changing the spectral resolution: Convoluting the fringes with a relatively broad Gaussian instrument response function smoothes the spectral shape. Using a spectrally too wide resolution function will broaden the line and hence distort the line shape, so this needs to be done carefully.

3.3 Methods of Analysis

The absorption spectra are taken with 100 fs pulses, hence giving an ultrafast snapshot at precisely the selected time delay. For photoluminescence the situation is quite different. It is taken continuously using a streak camera, all times in a single experiment, only quantized by the finite pixel width. The time resolution of the streak camera however is much larger than a single pixel; therefore spectra are integrated for ± 50 ps at every time delay. This also ensures a sufficient signal to noise ratio within the already long integration times. For the β analysis explained later in this chapter, each absorption spectrum is divided by the nonlinear absorption taken at the same time delay. Especially for long time delays, when cooling has mostly concluded and the change in the absorption peak is small, this averaging does not have a significant effect.

3.3.1 Carrier Temperature T

To describe the thermal state of the system, the carrier temperature T is extracted from the continuum emission. In thermodynamic equilibrium, the Kubo-Martin-Schwinger (KMS) relation [45, 46]

$$PL^{th.eq.}(\hbar\omega) \propto g(\hbar\omega - \mu)\alpha(\hbar\omega) \quad (3.1)$$

is generally used to establish the relation between the absorption coefficient α and the photoluminescence. Here,

$$g(\hbar\omega - \mu) = \frac{1}{e^{\frac{\hbar\omega - \mu}{k_B T}} - 1} \quad (3.2)$$

is the Bose distribution function, and μ is the joint chemical potential of the electrons and holes.

For low enough densities and temperatures, the Bose function can be approximated by a Boltzmann distribution function. The continuum absorption is spectrally flat for several meV above the band edge; see Figure 3.2. Therefore its emission decreases exponentially above the band edge, located 8 meV above the 1s exciton resonance. Due to experimental noise a small spectrally and temporally flat background may be present in the data; it is subtracted in all data shown. The data are therefore fit to

$$A \times \exp\left[-\frac{\Delta E}{k_B T}\right], \quad (3.3)$$

using a least mean square fit for the variables, amplitude A and carrier temperature T , with the corresponding standard deviations σ_A and σ_T . ΔE is the energy relative to the 1s exciton resonance. The errors given for the extracted temperatures are statistical. In order to get a small standard deviation for the temperature values, it is necessary to detect several meV of continuum emission; this requires four to five orders of magnitude dynamic range. Being only extracted from the continuum emission, the carrier temperature T by itself contains no information about the dynamics at the 1s exciton resonance.

3.3.2 1s to Continuum Edge Emission Ratio: R

To compare a large number of spectra as a function of density and lattice temperature, it is convenient to define a parameter to describe each spectrum. Ideally it is unambiguous and clearly explains all main features easily and comprehensibly. During the data analysis, characteristic parameters are introduced for this purpose.

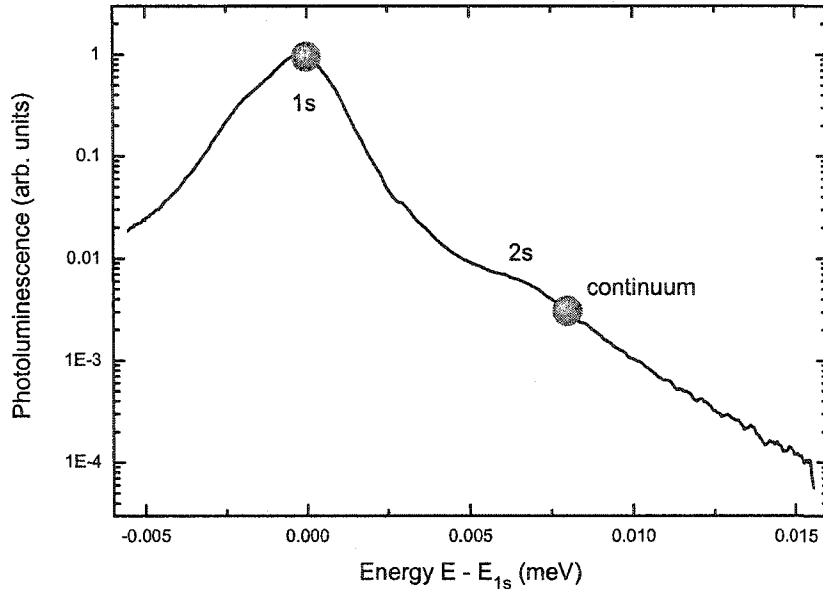


Figure 3.4: Schematic depiction of the definition of derived parameter R . The spectrum shows photoluminescence 1 ns after nonresonant ps excitation 13.2 meV above the exciton resonance for a lattice temperature of 4 K. The estimated carrier density at 1 ns is $2.0 \times 10^{10} \text{ cm}^{-2}$. Dividing the marked data points yields $R(1 \text{ ns}) = 311$.

For this study, the two main points of interest are the 1s resonance peak and the band edge. While 1s emission can be caused by both excitons and plasma, continuum emission is solely attributed to plasma decay. To connect the two, here their relative dynamics are considered.

Accordingly, the definition of R as ratio of 1s to continuum-edge emission is straight forward. It collapses the whole spectral shape into a single number, describing its main features. Due to its large oscillator strength, the 1s resonance dominates the emission spectrum. Its peak is normalized by the value at the continuum edge, 8 meV above as shown in Figure 3.4. This number is independent of any ambiguities common to photoluminescence such as integration time, collection efficiency, detected solid angle, and coupling efficiency. Its value is typically much larger than 1, tracking the dominance of the 1s emission in the spectrum. But does it give some

measure for excitonic contributions? R does not take into account any effects different temperatures have on the spectrum. The combination of R and the carrier temperature T , as well as correction for different oscillator strengths of the exciton resonances, leads to the introduction of another parameter: β .

3.3.3 β Factor

The attenuation factor β is defined as follows:

$$\beta = \frac{I_{\text{PL}}(1\text{s})}{I_{\text{PL}}^{\text{th. eq.}}(1\text{s})}. \quad (3.4)$$

$I_{\text{PL}}(1\text{s})$ is the measured or calculated photoluminescence at the 1s energy; $I_{\text{PL}}^{\text{th. eq.}}(1\text{s})$ gives the expected thermal equilibrium value. This definition of β not only relates R and the carrier temperature T but also divides out the dipole matrix element.

The definition is based on the KMS-relation Equation 3.1 presented above and motivated by a concept used in [47]. There, photoluminescence peak heights at the 1s and 2s resonances were compared via a Boltzmann function, and a suppression of the 1s emission was observed. However, in this dissertation β relates the 1s peak to the continuum emission [48]. $I_{\text{PL}}^{\text{th. eq.}}(\hbar\omega)$ is found by multiplying the measured nonlinear αL by a Boltzmann factor to approximate the Bose function, using the temperature T extracted as described above in Chapter 3.3.1. It is then normalized to agree with the measured continuum photoluminescence; the dashed line in Figure 3.5 shows $I_{\text{PL}}^{\text{th. eq.}}(\hbar\omega)$. Thus the parameter β quantifies how the 1s emission of a given spectrum differs from that expected from the measured absorption assuming thermodynamic equilibrium. In addition, it also gives a handle on the relative emission strength, corrected for the respective dipole matrix elements and oscillator strengths. Consequently, while the height of the 1s resonance is not as important anymore as in R , the temperature T , due to the exponential factor, is dominating.

The statistical error σ_β for β is calculated from the errors in the least mean square fit for the temperature. It is given by $\sigma_\beta \equiv \beta \times A / \sigma_A$. Note that σ_β does not explicitly depend on the carrier temperature T but only on the amplitude A and

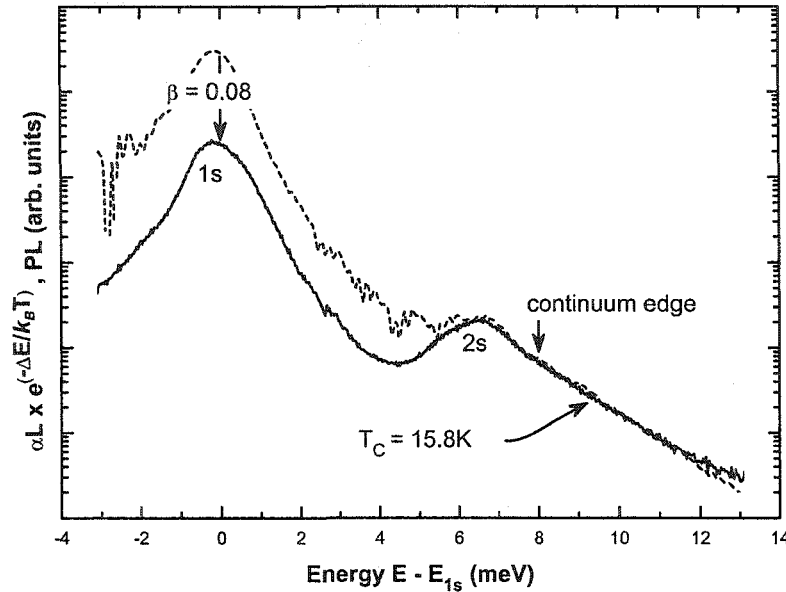


Figure 3.5: Schematic depiction of the definition of the β -factor. The experimental spectrum (solid) used shows photoluminescence for a lattice temperature of 4 K. It is compared to the KMS result $I_{\text{PL}}^{\text{th, eq.}}(\hbar\omega)$ (dashed), i.e. the measured nonlinear αL multiplied by the Boltzmann factor. The photoluminescence is integrated from 0.95 to 1.05 ns after nonresonant ps excitation 13.2 meV above the exciton resonance and with a carrier density $n_{ch} = 4.4 \times 10^8 \text{ cm}^{-2}$.

its error σ_A from Equation 3.3. The temperature dependence of the statistical error is hence the same as for β . This is because the zero of energy in Equation 3.3 is taken at the 1s resonance; were it taken at the continuum edge, A would be a small number, and σ_T would enter in projecting it back to the 1s resonance.

CHAPTER 4

EXPERIMENTAL REALIZATION AND SETUP

In order to investigate the problems as outlined in the previous chapters, it is necessary to perform photoluminescence and nonlinear absorption measurements under identical conditions. Here the necessary methodologies are described, and the realization of the experimental setup is presented.

4.1 Absorption

The linear and nonlinear absorption of the sample under investigation is measured with the setup schematically shown in Figure 4.1. Both pump and probe pulses are generated by an actively mode-locked Titanium:Sapphire laser with a fixed repetition rate of 80 MHz and a maximum time-integrated output power of 2 W. It is pumped by a diode-pumped, intra-cavity frequency-doubled Nd:YAG laser at 2.4122 eV with 9.5 W CW. The spectrally broad 100 fs pulses are tunable using a birefringent filter; the peak wavelength is typically centered at the heavy-hole continuum edge.

The long photoluminescence lifetimes of several nanoseconds require a reduction of the laser repetition rate from 80 MHz (12.5 ns period). For the experiments presented it is reduced by a factor of 40 to 2 MHz (0.5 μ s period) unless stated otherwise. The reason is to eliminate carrier accumulation effects in the sample. Also the maximum detection speed of the streak camera is 2 MHz in trigger mode; faster excitation is therefore not detected in time-resolved photoluminescence measurements; c.f. Section 4.2. The reduction in repetition rate is realized by using an electro-optic modulator (EOM) outside the cavity, making use of the electro-optical effect in an ammonium dihydrogen phosphate (APD) crystal. When applying a voltage, the polarization of transmitted light is rotated by 90 degrees. The light is then analyzed

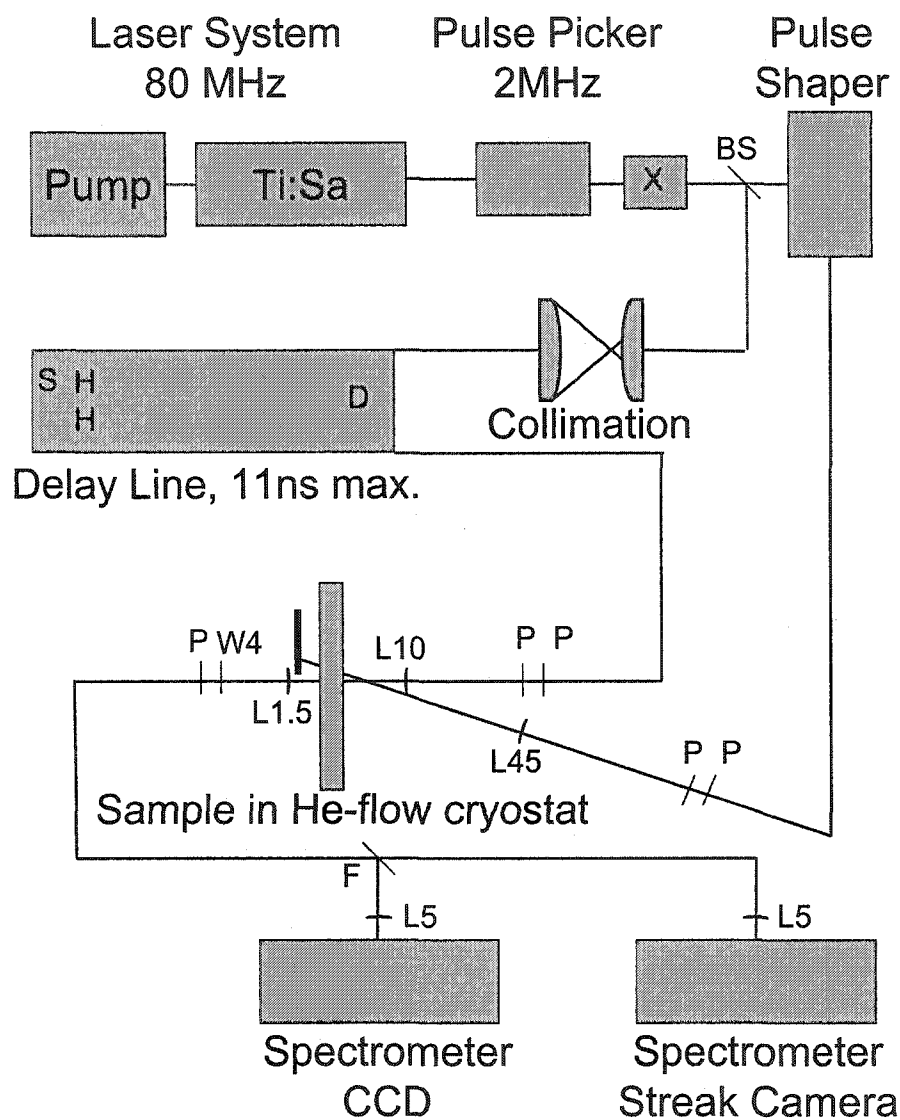


Figure 4.1: Schematic drawing of the experimental Setup. The labels are: X, periscope; BS dielectric 90:10 beam splitter; L10, 10 cm lens; L45, 45 cm lens; P polarizer; D variable delay line with multiple passes; S shaker; H hollow retro reflector; L1.5, 1.5 cm lens; W4, quarter wave plate; F, flip mirror; L5, 5 cm lens.

using a Glan-Thompson polarizer, only allowing correctly polarized pulses to pass through. Typical extinction ratios of better than 300:1 are achieved. Due to the relatively long switching times of the EOM, on the order of 10 ns, limited by the electronics, it is not possible to extinguish all pulses equally; one pulse has to be suppressed less. Generally, the less suppressed pulse hits the sample immediately after the unsuppressed pulse to avoid accumulation effects.

After the EOM, the laser beam is raised to the operating height of 13.5 cm with the periscope X; the height is predetermined by the entrance slit height of the streak camera. Here also the polarization is rotated from vertical (s) to parallel (p) to get better diffraction efficiency in the pulse shaper. Using a periscope eliminates chromatic effects always present in wave plates. It is consecutively split up into two beams using a dielectric 90:10 beamsplitter; its substrate is wedged and the rear surface AR-coated to eliminate unwanted reflections.

The weaker probe beam is put through a collimation unit consisting of two 0.1 NA microscope objectives. This also increases the probe pulse diameter to $2r = 5$ mm, completely filling the collimator's exit pupil. The large diameter and corresponding large Rayleigh-range $z_R(r) = r^2/\lambda_0$ enable the beam to remain collimated over very long distances. The probe is then propagated across a stepping-motor-driven 1 m delay line. To realize a delay between pump and probe pulse of up to 11 ns, it is necessary to use four passes. On top of the delay line, two hollow corner-cube retro reflectors are used to guide the beam. One of them is mounted on a shaker to easier find temporal overlap when using a cross-correlation technique between pump and probe. Although corner cubes return the incident beam satisfactorily, hollow right-angle-prism retro reflectors would be preferable; unlike the corner cubes, they cannot cause a high offset and have one less reflection.

The majority of the light, 90 % of its power, is split off into a grating pulse shaper. A detailed description of its setup can be found in [49]. For selective excitation, a spectrally narrower tunable 3 ps pulse is generated in a grating pulse shaper. Unless

stated otherwise, the spectral width of the pump pulse is 2 meV (FWHM). For completeness, ΔE , i.e. the spectral position of the pump relative to the 1s heavy-hole resonance, is given in Appendix A for all data sets.

The sample is held in a cold finger cryostat with small window separation, allowing for detection within large solid angles. The windows are broadband AR-coated on both sides. The system is evacuated using an oil-free turbo pumping stand and a liquid-nitrogen-cooled cryogenic pump. The first reaches a lower end pressure, while the latter has a greater pumping speed for water vapor. During operation, the cryostat is held under vacuum with an ion pump to avoid any vibrations and to allow for long cold times with limited condensation, caused by inevitable leakage through diffusion.

The pump and probe pulse are focussed onto the sample using two different lenses for individual focussing. To ensure spatial overlap, the front side of the sample is imaged onto a CCD camera using a 0.1 NA objective and 100x magnification. The fine adjustment is done by maximizing the bleaching of the 1s resonance for small time delays of about 10 ps. Temporal overlap is achieved by detecting both probe and scattered pump light with the streak camera. For a better time resolution, the shape of the differential absorption can be used as a measure for time delay. A pair of linear polarizers in both the pump and probe beam is used to set their respective polarizations and powers.

The probe signal is detected in transmission geometry. Another linear polarizer is used as an analyzer in the beam; introducing an optional quarter-wave plate can be used to further suppress scattered pump light. All experiments are conducted in cross linear polarization geometry; the polarizer settings are given in Table 4.1.

All but one mirror before the sample are ultrafast broadband dielectric mirrors used at 45° incidence angle. Their reflectivity is above 99.9% for both s and p polarization. Only the mirror steering the probe at a slight angle is metallic, protected gold, to avoid dispersion effects. Though having a slightly lower reflectivity, and thus sacrificing signal intensity, metallic mirrors are used on the detection side exclusively.

beam	polarizer setting
pump	parallel
probe	vertical
detection	vertical

Table 4.1: Typical polarizer settings

The extremely flat reflectivity of gold in the wavelength range of interest ensures an undistorted signal.

The transmission is spectrally resolved using a $f = 50$ cm imaging grating monochromator using a 600 lines/mm grating blazed at $1 \mu\text{m}$ and $50 \mu\text{m}$ entrance slit width; it is detected with a back-illuminated liquid-nitrogen-cooled Si CCD with $12 \mu\text{m} \times 24 \mu\text{m}$ pixels. This resolution is matched to the one achieved with the streak camera, limited by its limited number of pixels and therefore small spectral window; c.f. Section 4.2. The CCD chip is back illuminated. While yielding a higher quantum efficiency than front illuminated models, this leads to interference fringes for coherent (laser) light inside the CCD itself. This does, however not affect the αL measurements. As can be seen from Equation 4.3 and Equation 4.4, the Fabry-Pèrot fringes are divided out when calculating αL ; the signal intensities are much larger than the respective subtracted background intensities. Since the photoluminescence is intrinsically incoherent, these measurements are not affected.

In order to calculate the absorption αL of a weakly absorbing sample it is necessary to know both I_R , the reflected, and I_T , the transmitted, intensities [50]:

$$\alpha L \simeq -\ln \left(\frac{I_T}{(1 - I_R)^2} \right). \quad (4.1)$$

However, when the reflectivity approaches zero, as for an AR-coated system, Equation 4.1 is reduced to:

$$\alpha L \simeq -\ln(I_T). \quad (4.2)$$

In order to extract absorption $\alpha L(\lambda, \Delta\tau, T)$ and differential absorption $\Delta\alpha L(\lambda, \Delta\tau, T)$ from the actually recorded transmitted probe signal $I_t(\lambda, \Delta\tau, T)$, the following corrections need to be made:

$$\alpha L(\lambda, \Delta\tau, T) = -\ln \left(\frac{I_t(\lambda, \Delta\tau, T) - \text{BG}(\lambda)}{I_0(\lambda, \Delta\tau, T) - \text{BG}(\lambda)} \right) \quad (4.3)$$

$$\Delta\alpha L(\lambda, \Delta\tau, T) = -\ln \left(\frac{I_t(\lambda, \Delta\tau, T)|_{\text{pump on}} - \text{PL}(\lambda)}{I_t(\lambda, \Delta\tau, T)|_{\text{pump off}} - \text{BG}(\lambda)} \right) \quad (4.4)$$

Here I_0 is the spectrum of the incident light, $\text{PL}(\lambda)$ the photoluminescence and scattered pump light: i.e. the detected signal with pump light on only, no probe. $\text{BG}(\lambda)$ is the signal from the CCD, acquired when both pump and probe beams are blocked. Because the samples are AR-coated on both sides and not investigated at Bragg spacing, the extraction of the absorption from the transmission is valid [50].

4.2 Photoluminescence

4.2.1 Photoluminescence with Continuous Wave Excitation

Photoluminescence with continuous wave excitation is essentially taken in the same way as the pump-probe measurements described above, of course without any probe light. The main difference is that the pulsed Titanium:Sapphire laser is forced to run CW. This is achieved as follows: The active mode-locker is usually disabled, alternatively it can be driven out of phase with the cavity to further suppress mode locking. Setting the wavelength of emission requires several steps. The glass in the dispersion compensator is removed until the laser emission nearly ceases. Then the desired mode is selected with the birefringent filter in the cavity. If the correct wavelength cannot be reached, some glass is again added to the cavity. This process is repeated iteratively until the desired emission wavelength and mode characteristics are reached. It is important not to change any mirrors in the cavity because this changes the beam path through the rest of the setup. The beam path of the CW light is, similar to the pump pulse, through the pulse shaper onto the sample, and

the alignment is identical to the pump-probe experiment. The spatial overlap of pump beam and detection area is then aligned as for the pump-probe experiments. To eliminate heating effects, the pulse picker can be driven by a pulse generator to produce flat-top 100 ns pulses with a low duty cycle.

The detection is again similar to the pump-probe experiment. The only correction necessary is the subtraction of the camera background. The spectral resolution can be increased by using a 1800 lines/mm grating and further narrowing of the slit width. While absorption measurements are absolute and any spectral features are divided out, it is necessary to consider the energy dependence of the response function for the photoluminescence. However the spectral response of Si can be considered as flat at 1.476 eV over the range of ± 15 meV under investigation.

4.2.2 Time-Resolved Photoluminescence

The time-resolved luminescence measurements pose the greatest experimental challenge. In order to detect as large a solid angle as possible – and therefore the most signal – an AR-coated 1” diameter $f=1.5$ cm plano-convex lens is used for collection. The center of the pump spot is then imaged onto the entrance slit of a second identical 50 cm imaging monochromator.

The photoluminescence is detected with a Hamamatsu streak camera with a slow sweep unit. The use of a streak camera after a monochromator enables the simultaneous detection of spectral behavior and temporal evolution, ultimately limited by the time-frequency uncertainty relation. The streak camera is used in peak single photon counting mode, i.e. when more than one camera pixel per photon incident reads a signal above the set threshold, only the largest of neighboring pixels is counted. While photon counting enables the use of the full dynamic range of the streak camera, the signal has to be attenuated enough not to lose counts on multi-photon events. Each photon event on the camera triggers a signal, but once its amplitude surpasses the set threshold, additional photons are not counted within the readout-cycle time. As

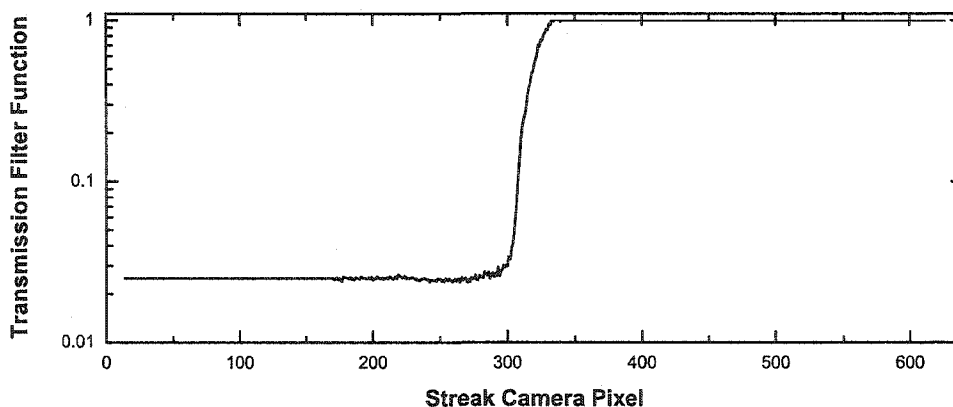


Figure 4.2: Attenuation of the thin film filter introduced in front of the streak camera. The attenuation is specific to each pixel.

a rule of thumb, fewer than 3% of the pump pulses should result in a photon count per channel, if distortion is to be avoided.

To even better utilize the dynamic range of the streak camera, a film neutral density filter is placed at the exit plane of the monochromator reducing the fluence by 40 for all energies < 1.474 eV. This is extremely helpful because a partial goal of this study is to detect several meV of continuum emission which is intrinsically four to five orders of magnitude lower than the emission peak at the 1s resonance. The latter itself decays after reaching a peak shortly after excitation. The transmission curve of the spectrometer-filter system can be seen in Figure 4.2. The relatively slow filter cutoff is due to edge diffraction. All data presented in this dissertation have been multiplied by this factor to present them undistorted. The spectral response of the streak camera system is plotted in Figure 4.3. It is dominated by the rapid drop off of the multichannel plate at low and high wavelength. The small window under investigation makes the correction negligible.

The slow sweep unit allows for detection of temporal windows of 3.8 ns and 8 ns, amongst others. A time resolution of 90 ps is measured for the spectrometer-streak camera system, using a 100 fs pulse. This value is mainly due to timing jitter in the pulse picker during long integration times of up to 36 hours; an output from pulse picker electronics is used as a trigger input for the streak camera. To adjust the time

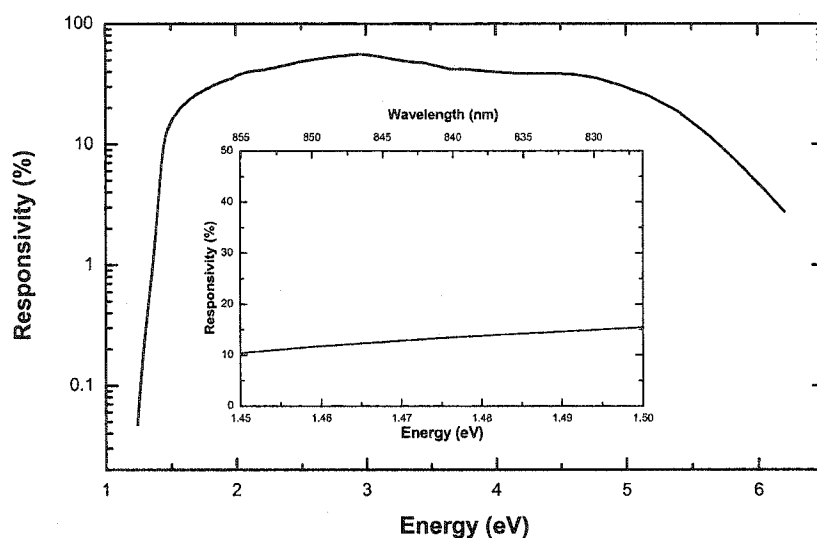


Figure 4.3: Spectral response of the streak camera system (S2-ER cathode) on a logarithmic scale. The inset shows the region of interest for the experiments on a linear scale with an expanded energy scale [51].

zero occurrence in the time window detected, an analog delay box is used; unlike digital delays, adding cable does not add additional jitter.

The magnification of the imaging system on the detection side was chosen to be 1:4, to match the $F/\#$ of the monochromator as well as to limit the field of view to $12.5 \mu\text{m}$ on the sample. The latter is limited horizontally by the entrance slit of the monochromator and vertically by the entrance slit of the streak camera. The latter also partially determines the temporal resolution. When the entrance slit of the streak camera is opened further than $50 \mu\text{m}$, its temporal resolution decreases. A smaller slit width, however, does not improve the temporal resolution, but limits the number of photons passing through the slit and hence reduces the signal amplitude.

It is also possible to take data with time resolutions as fast as 2 ps by running the streak camera using a synchro-scan plug-in at 80 MHz repetition rate. In this case, dispersion introduced by the monochromator has to be taken into account. The signal gets distorted, because the time axis of the streak camera is different for different

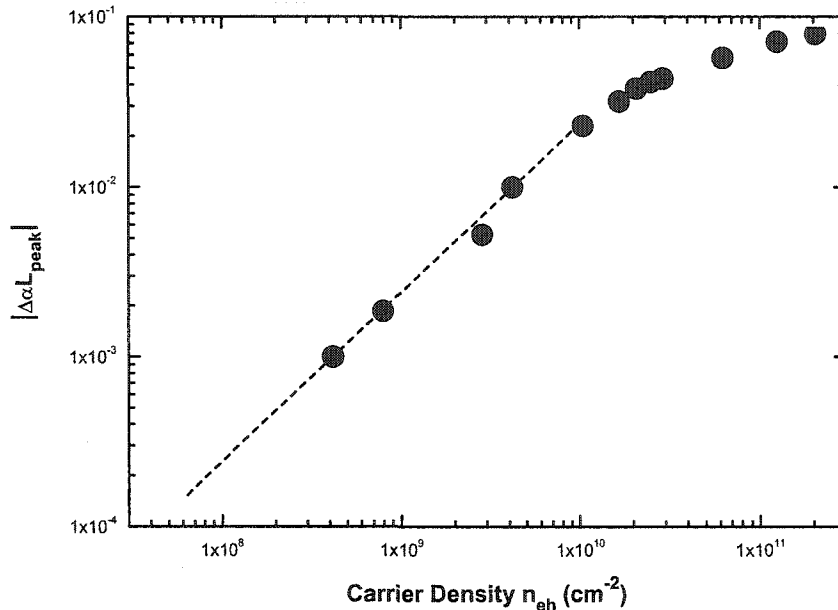


Figure 4.4: $\Delta\alpha L$ versus carrier density at 4 K. Both carrier density and $\Delta\alpha L$ are shown per quantum well; they are assumed to be the same in each quantum well because pump depletion is negligible. For low carrier densities the curve is extrapolated by linear regression.

wavelengths. This distortion can be corrected numerically; then dispersion in the monochromator used to spectrally resolve the signal determines the time resolution.

4.3 Characterization of Excitation Conditions

To ensure absolutely equal conditions of all measurements the physical positions of the spots need to be well defined. The pump spot size needs to be chosen several times larger than the probed area, so only the uniformly illuminated center section is probed. Accordingly a $f=10$ cm lens for the probe and $f=45$ cm lens for the pump were used. Because of different beam diameters at the respective lenses, the measured Gaussian spot profiles are $20 \mu\text{m}$ FWHM and $60 \mu\text{m}$ FWHM respectively.

Pump depletion is neglected in the density calculation. Therefore the carrier density can be seen as identical in each quantum well. Using the above parameters, the initial carrier density introduced into the each quantum well can be calculated

as follows:

$$n_{eh} = \frac{1}{A} (1 - e^{-\alpha L}) \frac{P_0}{\hbar\omega \cdot f_{rep}} \quad (4.5)$$

Here αL is the absorption value at the pump energy per quantum well, that is the measured value divided by the number of wells; α is measured to be 1 per micron in the heavy-hole continuum (see Figure 3.2). The time-integrated power is given by P . The pump pulse value P_0 in Equation 4.5 can be found by correcting for the imperfect pulse suppression; $\hbar\omega$ is the photon energy of the pump, f_{rep} the repetition rate. Together $\frac{P}{f_{rep} \cdot \hbar\omega}$ gives the number of photons per pulse. The number of absorbed photons is then normalized by the pump area $A = 2\pi \int_0^{d_{probe}^{FWHM}/2} I_{Pump}(r) r dr$, when assuming circular symmetry. Here d_{probe}^{FWHM} is the probe diameter (FWHM), and $I_{Pump}(r)$ is the intensity distribution of the pump. The area of the pump spot cancels from Equation 4.5.

To estimate the carrier density during the decay at longer times, it is assumed to be linearly proportional to the change in absorption $\Delta\alpha L$. A calibration curve showing maximal bleaching of the nonlinear absorption at 10 ps versus the calculated initial carrier density (Figure 4.4). From it the carrier density at any time delay can be read off using the corresponding $\Delta\alpha L$. The carrier density $n(t)$ may consist of both electrons and holes as well as excitons or $n = n_{eh} + n_X$. The influence of excitons on the absorption αL , $\frac{\delta\alpha L}{\delta n_X}$, may be smaller than that for free electrons and holes, $\frac{\delta\alpha L}{\delta n_{eh}}$. However, assuming both as equal should give an error of less than a factor of two. Hence conclusions drawn later in Chapter 6 would not change significantly, especially since $n_X \ll n_{eh}$ for many conditions.

CHAPTER 5

EXPERIMENTAL RESULTS

In this chapter an overview of the acquired data is given. It is an attempt to structure the results by showing exemplary spectra and explain dependencies in the parameter space of time delay, excitation density, lattice temperature and excess energy of the pump relative to the 1s exciton resonance ΔE .

All data presented here were taken on DBR 42; due to its superior quantum efficiency, it yielded the best signal to noise ratio. Mostly CW data taken on other samples, amongst them a single quantum well, are noisier but exhibited a similar behavior, thus excluding significant radiative coupling [41, 42, 43, 44] and reabsorption [29] as well as sample specific effects. A detailed list of data and excitation conditions as well as other parameters of the experiment such as integration times and excess energy of the pump is given in Appendix A.

5.1 Absorption Changes after Nonresonant Excitation

As pointed out several times before, the absorption measurements play a critical role. They are necessary for a meaningful density calibration. To get a better understanding of the density range covered in these experiments, Figure 5.1 shows exemplary nonlinear absorption spectra for the largest initial carrier density with nonresonant excitation at 4K lattice temperature. For the experiment with the largest excitation density realizable, immediately after excitation the 1s resonance is bleached to less than one fourth of its original height (dashed). The estimated initial carrier density is $2.0 \times 10^{11} \text{ cm}^{-2}$. The band edge is significantly red-shifted; the 2s state is no longer bound. With increasing time delay, the exciton resonance begins to recover. 1 ns after excitation, the exciton peak has already regained 75 % of its

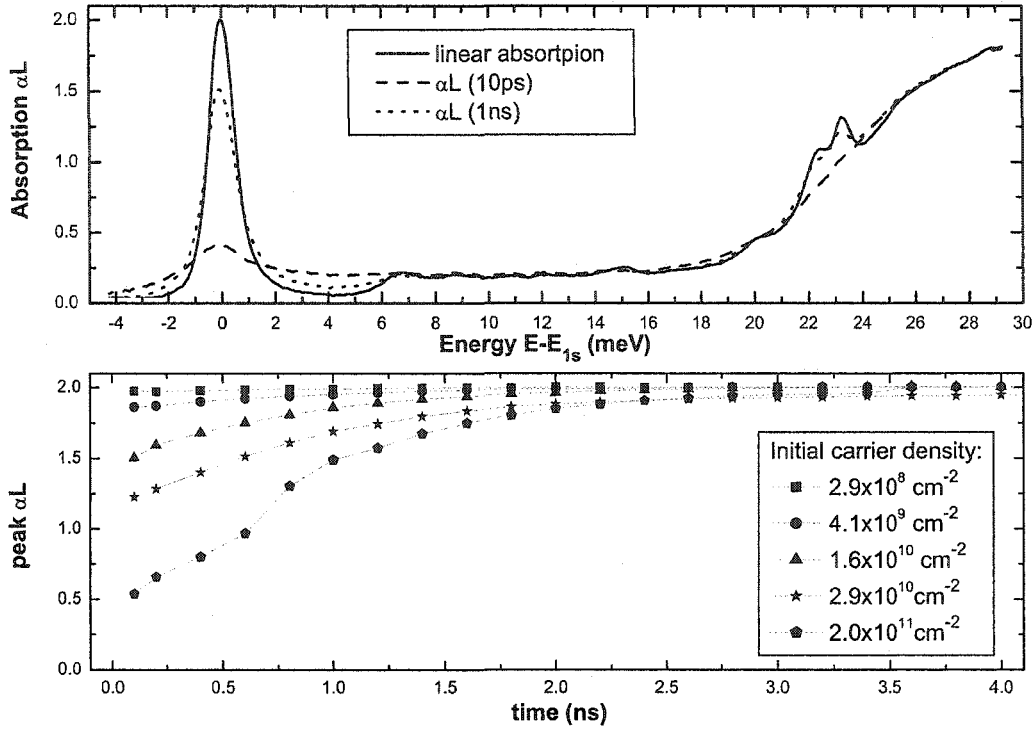


Figure 5.1: Top: Nonlinear absorption spectra of DBR42 at 4K lattice temperature for various time delays: The corresponding carrier densities are $2.0 \times 10^{11} \text{ cm}^{-2}$ at 10 ps (dashed) and $2.0 \times 10^{10} \text{ cm}^{-2}$ at 1 ns after nonresonant excitation (dotted). The linear absorption spectrum is shown for comparison (solid). Bottom: Temporal evolution of the peak height for various initial carrier densities: $2.9 \times 10^8 \text{ cm}^{-2}$ (squares), $4.1 \times 10^9 \text{ cm}^{-2}$ (circles), $1.6 \times 10^{10} \text{ cm}^{-2}$ (triangles), $2.9 \times 10^{10} \text{ cm}^{-2}$ (stars), and $2.0 \times 10^{11} \text{ cm}^{-2}$ (pentagons). The lines are guides to the eye.

linear value (solid). According to Figure 4.4, this corresponds to a carrier density of about $2.0 \times 10^{10} \text{ cm}^{-2}$.

To examine the temporal behavior of the nonlinear absorption in greater detail, the lower panel of Figure 5.1 shows the peak height of the differential absorption $\Delta\alpha L$ versus time for several excitation densities. With larger initial carrier density, the exciton resonance is bleached further. It recovers on a nanosecond time scale; 5 ns after excitations the deviations to the linear value are much less than 1%. This makes

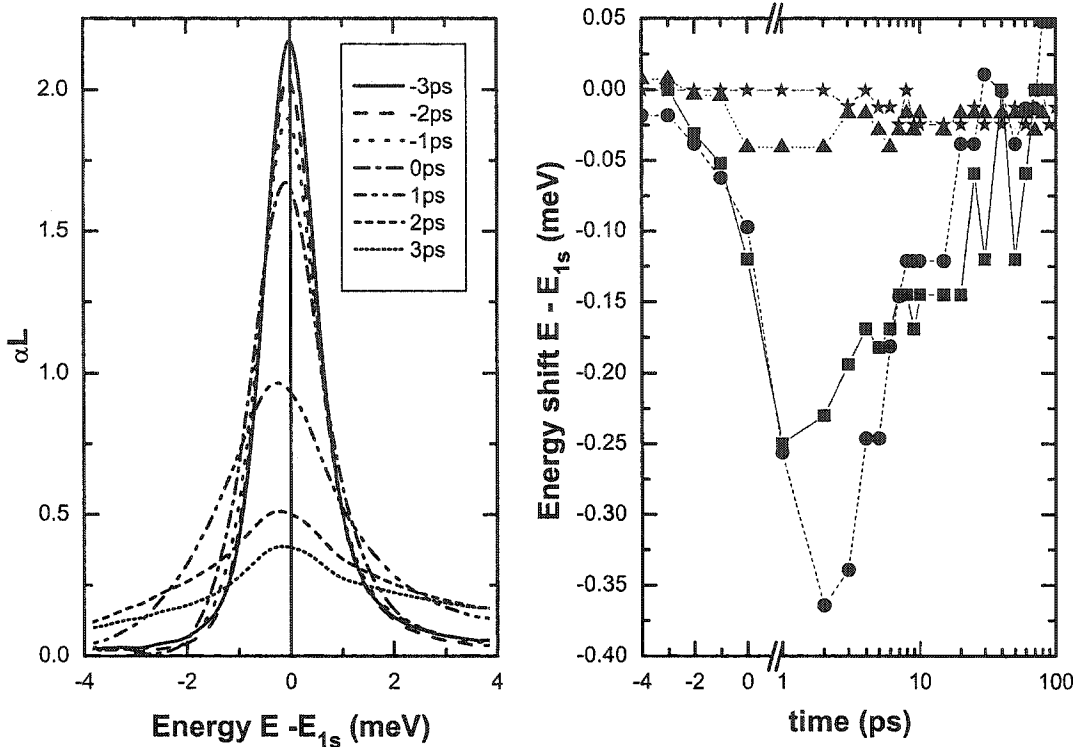


Figure 5.2: Left: Nonlinear absorption spectra of DBR42 at 4 K lattice temperature for short time delays. The initial carrier density is $2.0 \times 10^{11} \text{ cm}^{-2}$. Right: Energetical position of the resonance relative to the peak position of the linear αL versus time for several initial carrier densities: $2.0 \times 10^{11} \text{ cm}^{-2}$ (squares), $1.2 \times 10^{11} \text{ cm}^{-2}$ (circles), $4.0 \times 10^9 \text{ cm}^{-2}$ (triangles), and $1.2 \times 10^9 \text{ cm}^{-2}$ (stars). Note the break in the x-scale.

very accurate differential absorption measurements necessary to ensure a meaningful density calibration at low densities.

At the same time the energetical position of the resonance shifts, depending on both time delay and carrier density [52, 53, 54, 55]. This effect is even more pronounced for shorter times than shown in Figure 5.1. On the left hand side of Figure 5.2, nonlinear absorption spectra for pump-probe delays of -3 ps to 3 ps are plotted. The maximum induced carrier density for the data set shown is $2.0 \times 10^{11} \text{ cm}^{-2}$. The largest blue shift is reached at about 1 ps, roughly coinciding with the end of the pump pulse. Subsequently, the 1s resonance shifts back, recovering its “linear position” on a nanosecond time scale.

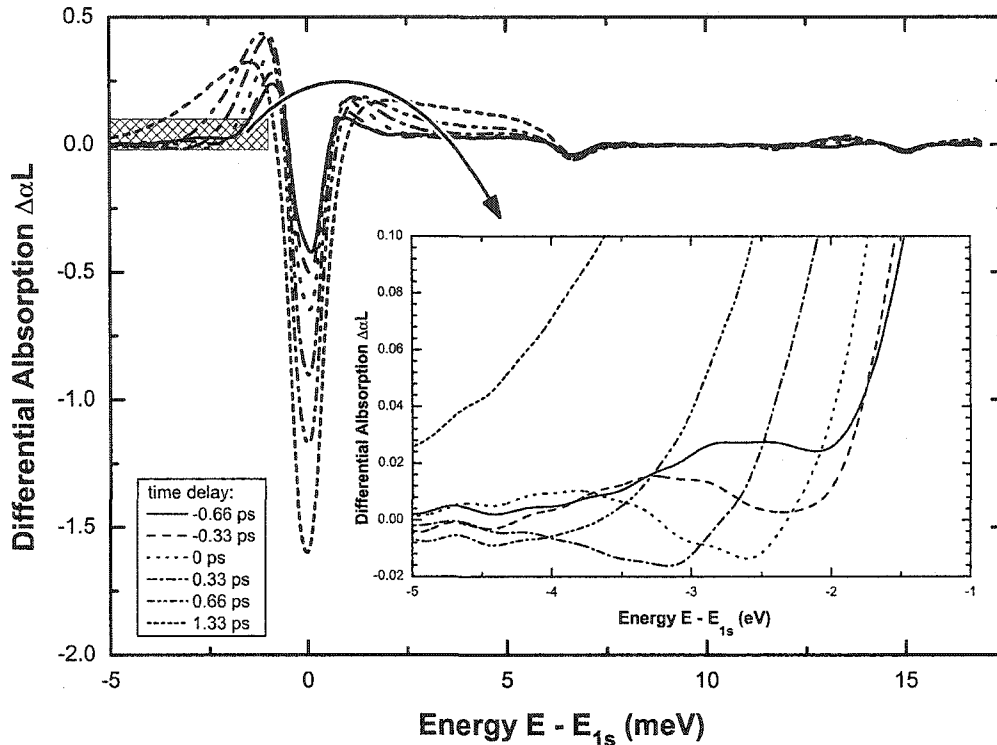


Figure 5.3: Differential absorption spectra with nonresonant excitation of DBR 42 for several time delays. The introduced carrier density is $2.0 \times 10^{11} \text{ cm}^{-2}$. The spectral region -5 meV to -1 meV below the $1s$ exciton resonance is magnified in the inset.

The time evolution of the blue shift and its magnitude are shown on the right hand side of Figure 5.2. Note the break in the x-scale: for -4 ps to 1 ps time delay the x-scale is shown linearly, above 1 ps the plot is semi-logarithmic to show better short positive time delays. For elevated carrier densities, the resonance starts to shift to larger energies during the pump pulse.

The largest shift is found for elevated densities ($1.2 \times 10^{11} \text{ cm}^{-2}$, circles), except at the highest carrier density introduced ($2.0 \times 10^{11} \text{ cm}^{-2}$, circles). This is consistent with [54], where a saturation behavior of the blue shift above $5 \times 10^{10} \text{ cm}^{-2}$ is observed. For decreasing densities, the shift is less pronounced ($4.0 \times 10^9 \text{ cm}^{-2}$, triangles). Eventually for low enough densities, no shift is observed at all ($1.2 \times 10^9 \text{ cm}^{-2}$, stars).

In prior work, a blue shift for nonresonant excitation has been interpreted as excitonic signature [52]. The magnitude of the shift was later found to be well-width dependent [53], only clearly observable in thin quantum wells and decreasing with increasing well thickness. In light of findings in this dissertation (c.f. Chapter 6), prior interpretations need to be reexamined.

Taking a closer look at the low energy side of the differential absorption reveals traces of induced gain. Figure 5.3 shows differential absorption spectra for 0 ps time delay, that is while the pump pulse is present. The inset magnifies the criss-crossed area as indicated, 1 meV to 5 meV below the exciton resonance. Here the y-scale is magnified by about a factor 4.5. For the duration of the pump pulse, induced gain develops below the resonance. At early times it is situated at 2.1 meV below the resonance, reaching the maximum gain at the end of the pulse. Subsequently, the lineshape recovers, and the line becomes broadened by induced absorption above and below the resonance. The origin of this phenomenon is not yet understood.

5.2 Time-Integrated Photoluminescence

While the main goal of the experiments is to examine photoluminescence and absorption under identical conditions, already some information can be deduced from the photoluminescence itself. A first classification of the samples' emission characteristics can be obtained by studying time-integrated PL with continuous wave excitation (Figure 5.4). If one extrapolates the continuum tail to the 1s exciton resonance, one can calculate the ratio of this value to the 1s luminescence peak and then divide it by the 1s to continuum ratio of the linear absorption. For all samples, this gives the PL ratio lower than the absorption ratio implying a β of less than one. The error introduced by considering the linear absorption only is small; the density range for the CW experiments is similar to the pulsed experiments.

Generally, the carrier temperatures are very hot in the CW experiments: The carriers are introduced typically 13.7 meV above the 1s; this corresponds to 6 meV excess energy in the conduction band or 70 K. The extracted carrier temperature is

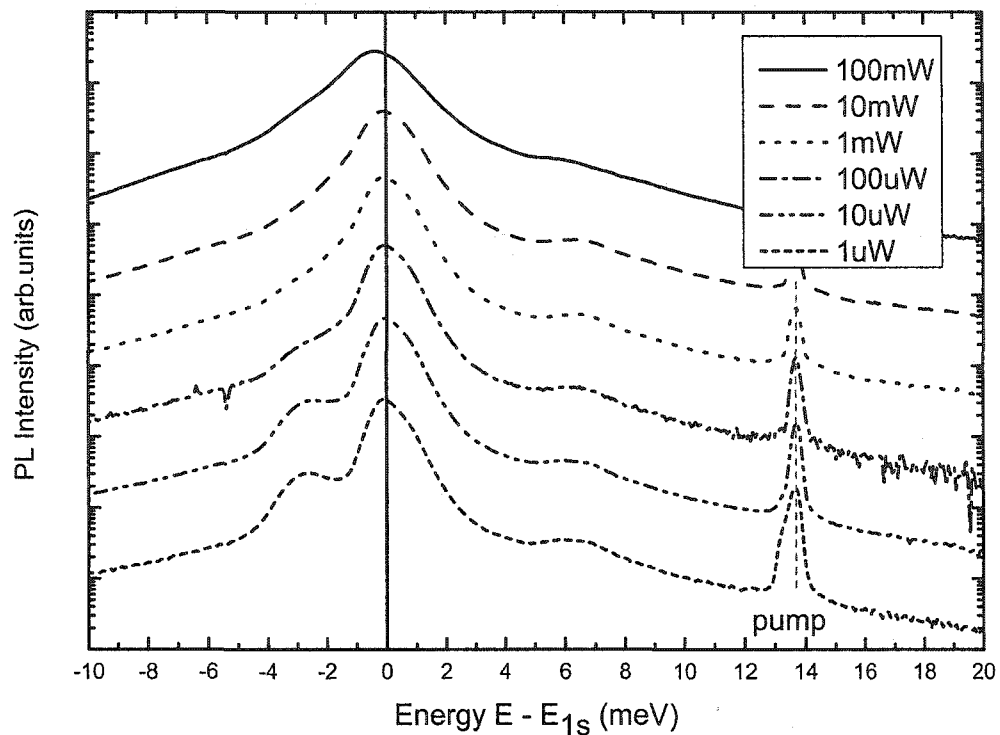


Figure 5.4: Time-integrated photoluminescence with continuous wave excitation of DBR 42 on a semi-logarithmic scale for various excitation power levels. The peak 2.5 meV below the 1s emission is presumed to be impurity emission (c.f. Figure 3.3).

40 K, significantly higher than the lattice temperature of 4 K. The excitation energy is slightly higher than in the ps excitation experiments; the exact same energy could not be achieved with the laser due to its large cavity length. The narrow band CW laser line is broadened by the spectral resolution to 0.8 meV. The signal detected from scatter in CW experiments is relatively high compared with the ps excitation experiments presented in the next section; the ps pump is short in duration, shut off after 3 ps and then remains zero for a comparably long time while in CW experiments the pump is always on.

The linewidth (FWHM) of the emission is broader for higher excitation density. Even at the largest excitation density the 2s resonance is still somewhat resolved. With the current heat sink, it is not possible to take even higher densities with CW

sample	DBR 42	DBR 13	1a1124	DBR 18
Approximate β	0.5	0.14	0.2 – 0.7	0.4

Table 5.1: Approximate β of 1s emission with CW excitation

excitation because localized heating due to the pump shifts the resonance to lower energies. Traces of this effect can be seen in the 100 mW curve where the peak emission is already slightly red-shifted.

Impurity emission is relatively more important for time-integrated photoluminescence measurements with CW excitation than for ps excitation. The reason is the much longer lifetime of impurities, several tens to hundreds of ns compared to only a few ps for the quantum wells. CW excitation experiments therefore even allow for a crude classification of the factor β of 1s emission as described above. Typical approximate β values for different samples are given in Table 5.2.

5.3 Time-Resolved Photoluminescence after Nonresonant Excitation

For the time-resolved photoluminescence after nonresonant picosecond excitation the carriers are introduced into the sample in a very short time; typically the durations of the pump pulse is 3 ps. The rise and subsequent decay of the luminescence are detected time-resolved; c.f. Chapter 4.2.2. A representative set of emission spectra can be seen in Figure 5.5, shown on a semi-logarithmic (left) and linear (right) scale. The emission is peaked at the 1s resonance. The spectra are integrated from $t-0.05$ ns to $t+0.05$ ns around each time point. The scattered pump spectrum is still visible in the spectrum with the shortest time delay (0.1 ns). Despite being integrated nominally from 50 ps to 150 ps after excitation and the cross-linear polarization geometry of the setup, some residual scatter can be seen due to the limited time resolution of the system which broadens the 3 ps pump pulse to 90 ps effectively. The total scatter is low compared to the photoluminescence; time-integrated its peak is lower than the 2s emission.

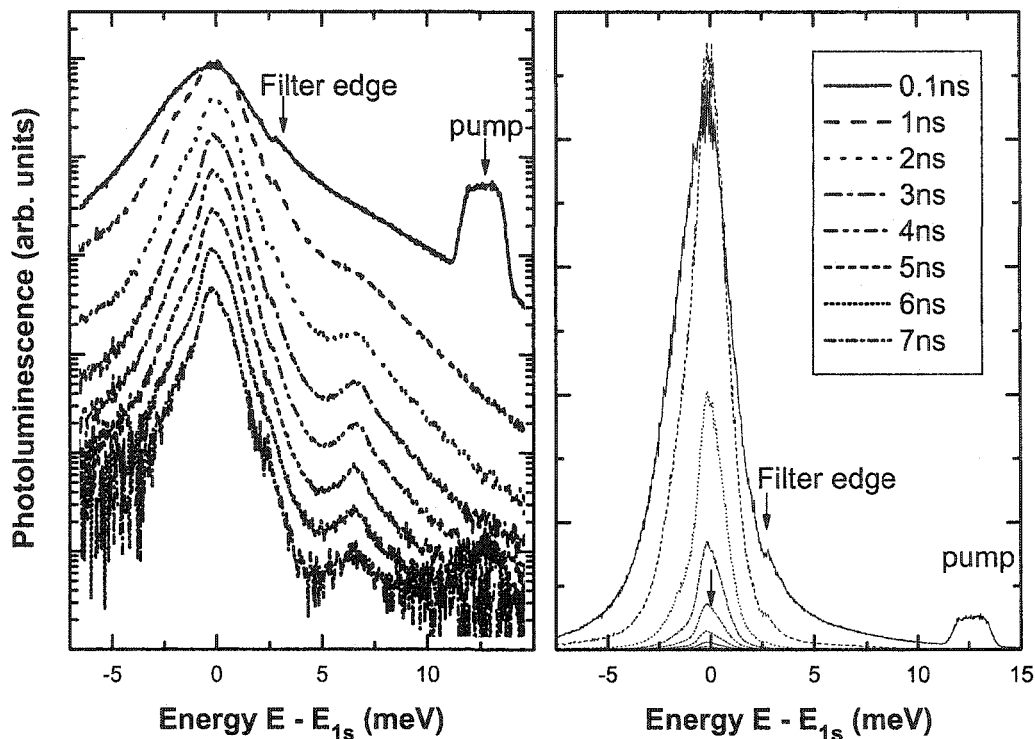


Figure 5.5: Experimental photoluminescence spectra on a linear (right) and semi-logarithmic scale (left) for several time delays after nonresonant excitation with an initial carrier density of $9.7 \times 10^9 \text{ cm}^{-2}$ for a lattice temperature of 4 K. The photoluminescence is integrated from $t-0.05 \text{ ns}$ to $t+0.05 \text{ ns}$ for each time step t .

The small discontinuity on the high energy slope 3 meV above the peak is due to the imperfect correction of the attenuator used for higher energies. For time-resolved experiments, the impurity emission below the 1s peak emission is much smaller at early times than in the CW experiments (Figure 5.4). The buildup of the impurity states occurs on a much longer time scale than the one under investigation. Generally, the absorption in the substrate, despite its much larger thickness, is smaller than the quantum well absorption at the excitation energy.

The initial elevated carrier density broadens the emission line significantly. As the carrier density decays, the linewidth decreases. After about 1 ns the 2s resonance starts to become clearly resolved. At the same time the system cools down towards the lattice temperature. This is manifested in an increasing slope of the continuum

emission. A detailed description of the cooling behavior is given in Section 5.3.2. The large carrier density broadens the line; when such broadening overcomes the intrinsic inhomogeneous broadening, the lineshape becomes predominantly Lorentzian. As the density decays the inhomogeneous broadening becomes dominant, and the line becomes very asymmetric.

Also the peak amplitude changes with time delay. The first curve, after 0.1 ns, is lower than the 1 ns curve. The maximum peak height is not reached until several hundreds of picoseconds after the end of the excitation pulse. A detailed description of the 1s peak dynamics with time and carrier density is given in Section 5.3.1.

5.3.1 Decay of 1s and Continuum Luminescence

The time evolution of the 1s emission can be studied in several ways. It is possible to spectrally integrate between the FWHM points or all energies below the midpoint between 1s and 2s. Alternatively, the peak of the emission spectrum can be traced. Here the spectrum is integrated 0.05 meV around the peak of the linear absorption spectrum. The results for the other methods of analysis do not change the results significantly.

The left hand side of Figure 5.6 shows the 1s peak luminescence versus time on a semi-logarithmic scale. Each data set is normalized to its maximum. The data sets are offset one order of magnitude for clarity. The largest density, shown in the bottom curve, has the fastest photoluminescence decay; a single-exponential fit to the decay yields a 1 ns lifetime. The lowest density shown at the top has a much longer photoluminescence lifetime of 2.6 ns. Its low signal level only allowed for detection of about 3.5 ns after excitation with reasonable signal to noise ratio, even with an integration time of 36 hours.

The linear plot on the right hand side of Figure 5.6 clearly shows the dynamics of the peak of the 1s emission. The values are again normalized to the respective maximum. The emission continues to increase after the end of the excitation pulse. For lower excitation densities, the peak is reached about 0.8 ns after excitation. With

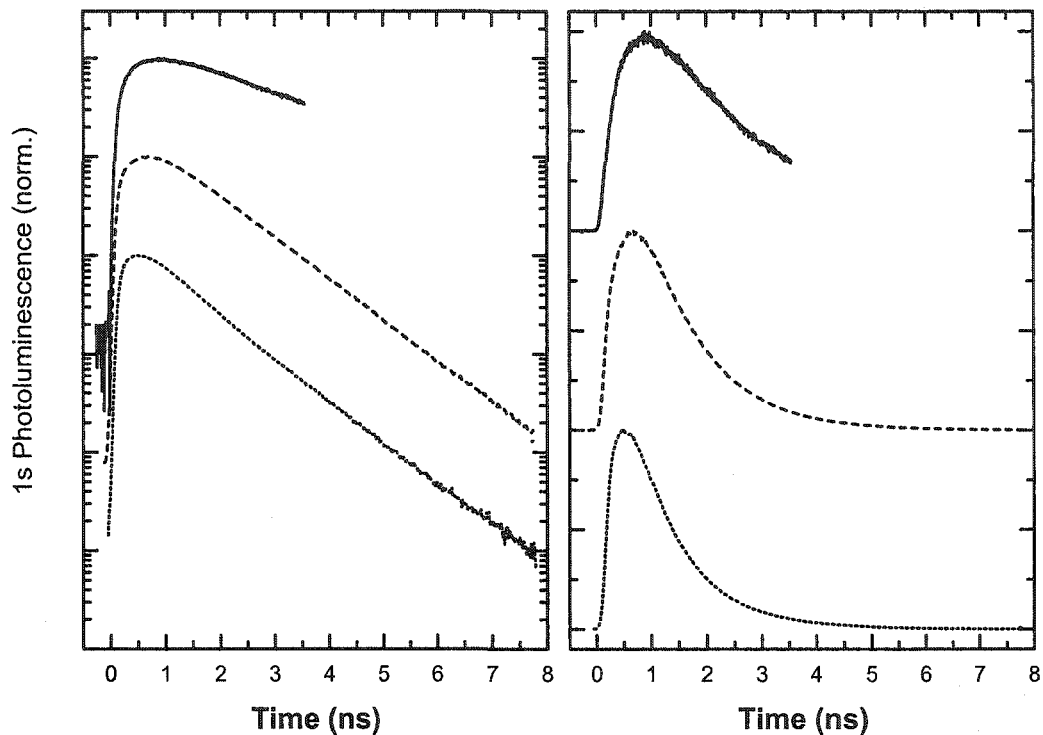


Figure 5.6: Temporal evolution of the 1s resonance peak height. The initial carrier densities are (from top to bottom) $2.9 \times 10^8 \text{ cm}^{-2}$, $1.1 \times 10^{10} \text{ cm}^{-2}$, and $1.0 \times 10^{11} \text{ cm}^{-2}$. All data sets are normalized. left: semi-logarithmic scale, data sets are offset by one order of magnitude for clarity. right: linear scale, the data sets are offset for clarity. The lifetimes and peak positions are given in Table 5.2.

increasing carrier densities, it occurs at earlier times. The highest density shows an even faster rise, peaking after 0.4 ns.

Similar temporal behavior has been observed in previous experiments also. The buildup of the photoluminescence after nonresonant excitation has been interpreted as buildup of an incoherent excitonic population [8, 9, 10, 11, 12, 13, 14]. The subsequent decay was taken as evidence for this population decaying [15, 16]. However in light of findings presented later in this dissertation, *c.f.* Chapter 6, interpretations using a purely excitonic picture need to be reviewed carefully.

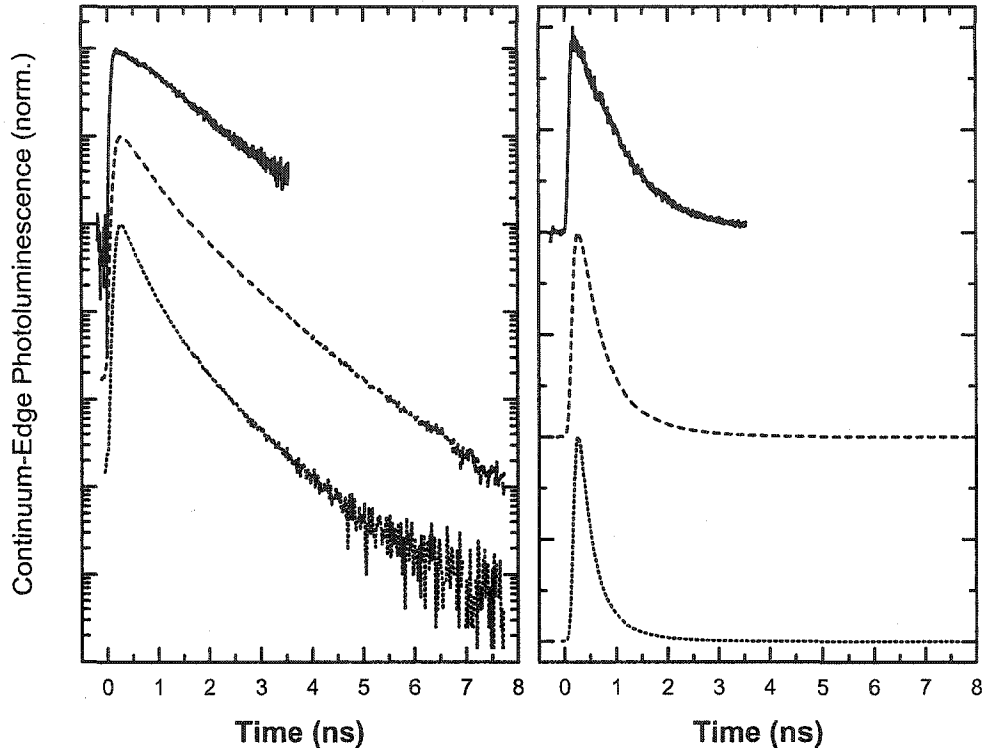


Figure 5.7: Temporal evolution of the continuum-edge emission. The data are spectrally integrated from the continuum edge to 0.01 meV above it. The initial carrier densities are (from top to bottom) $2.9 \times 10^8 \text{ cm}^{-2}$, $1.1 \times 10^{10} \text{ cm}^{-2}$, and $1.0 \times 10^{11} \text{ cm}^{-2}$. All data sets are normalized. left: semi-logarithmic scale, data sets are offset by one order of magnitude for clarity. right: linear scale, data sets are offset for clarity. The lifetimes and peak positions are given in Table 5.2.

initial carrier density	1s lifetime	1s peak	continuum lifetime	continuum peak
$2.9 \times 10^8 \text{ cm}^{-2}$	2.3 ns	0.9 ns	0.85 ns	<0.1 ns
$1.1 \times 10^{10} \text{ cm}^{-2}$	1.1 ns	0.65 ns	0.7 ns	<0.1 ns
$1.0 \times 10^{11} \text{ cm}^{-2}$	0.95 ns	0.5 ns	0.6 ns	<0.1 ns

Table 5.2: Photoluminescence lifetimes and time delays of the peaks of the 1s and continuum-edge emission for several initial carrier densities at 4 K lattice temperature, extracted from the time traces shown in Figure 5.6 and Figure 5.7.

Recent THz experiments also question a purely excitonic interpretation [24]. The observed photoluminescence dynamics are similar to the results presented here, showing a clear rise after the pump pulse. The THz absorption signal of the 1s to 2p transition however shows no significant increase within the first 400 ps. This clearly denies the possibility for a buildup of a significant incoherent excitonic population. However, the signal to noise ratio in THz experiments is much worse than in optical spectroscopy. Hence the sensitivity limits the actually detectable excitonic contribution.

The dynamics of the continuum emission for the same conditions are plotted in Figure 5.7. The main emphasis in this section is on the continuum edge; the slope and hence the temperature dynamics are described in the following section. The data are spectrally integrated across a narrow range, from the band edge to $10 \mu\text{eV}$ above it, to achieve an acceptable signal to noise ratio. The decay of the continuum emission, especially at elevated densities, cannot be fit by a single-exponential function as well as the 1s emission decay. At low densities, the decay time is on the order of 1 ns similar to the high density value of the 1s emission. Generally, the decay of the continuum shows a less pronounced density dependence; it is faster for higher densities. The peak of the continuum luminescence is reached directly after the end of the excitation across the density range under investigation.

While the carriers are introduced only across the narrow energy range of the pump pulse, Coulomb scattering causes the electrons and holes to thermalize to Fermi-Dirac distributions with a carrier temperature T on a sub-picosecond time scale [56, 57]; the carrier temperature T is usually much hotter than the lattice temperature T_L . Within the achieved time resolution, this can be regarded as instantaneous. After the redistribution, carriers are also present in states with much larger energies than the pump energies. Subsequently, the plasma can directly decay across the whole energy range.

The dependence of the decay times on the lattice temperature is shown in Figure 5.8 in a semi-logarithmic plot. For an initial carrier density of $8.2 \times 10^9 \text{ cm}^{-2}$, the

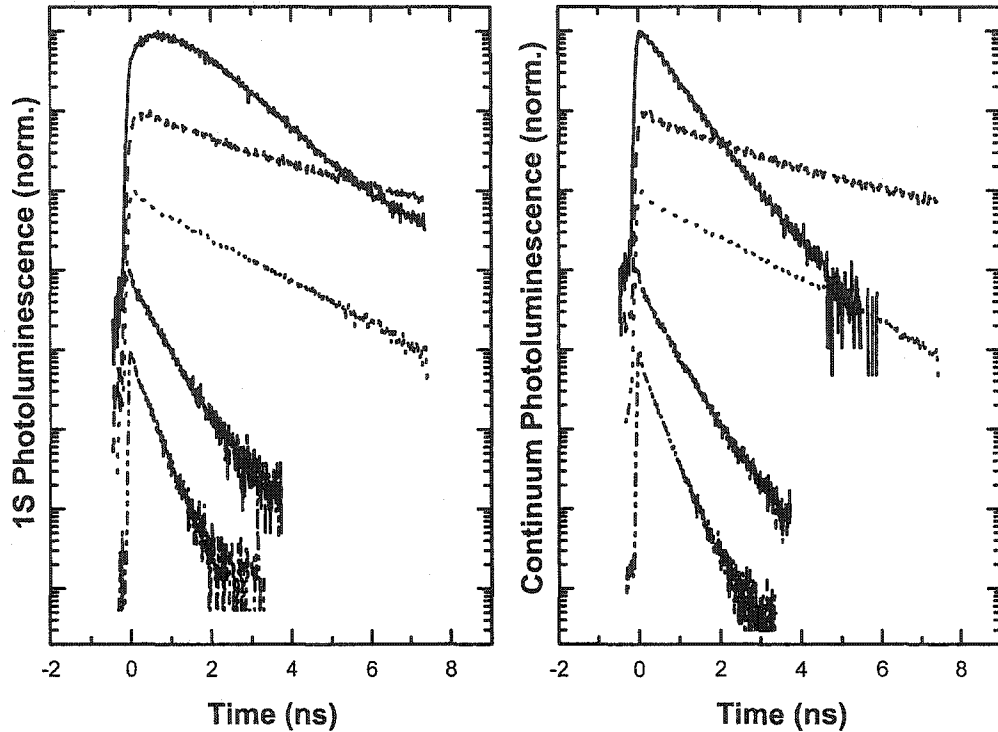


Figure 5.8: Temporal evolution of the 1s resonance peak height (left) and continuum edge (right) at several lattice temperatures (from top to bottom): 4 K, 30 K, 50 K, 70 K, and 80 K. The initial carrier density is $8.2 \times 10^9 \text{ cm}^{-2}$ for all data sets. The curves are normalized and offset by one order of magnitude for clarity. The decay constants are given in Table 5.3.

lattice temperature	1s lifetime	1s peak	continuum lifetime	continuum peak
4 K	1.0 ns	0.75 ns	0.76 ns	<0.1 ns
30 K	2.7 ns	0.3 ns	2.4 ns	<0.1 ns
50 K	1.7 ns	0.1 ns	1.7 ns	<0.1 ns
70 K	0.5 ns	<0.1 ns	0.5 ns	<0.1 ns
80 K	0.36 ns	<0.1 ns	0.36 ns	<0.1 ns

Table 5.3: Photoluminescence lifetime and time delay for the respective peak of the 1s and continuum-edge emission lifetime for several lattice temperatures, extracted from the time traces shown in Figure 5.8.

lattice temperature is varied from 4 to 80 K. As the temperature is increased, the lifetimes of both the 1s resonance and the continuum edge increase. Above about 30 K lattice temperature, the lifetimes begin to decrease. Also, the lifetimes become more similar, being identical for 50 K and higher temperatures. The extracted values are given in Table 5.3.

The decrease of the photoluminescence lifetime for even higher lattice temperatures can be at least partially explained by carriers escaping from the quantum well. The energy of the quantum well is roughly 44 meV below the bulk GaAs band edge. The carriers are injected by nonresonant optical pumping with an energy 13 meV above the quantum well energy. The fast redistribution from the pump energy into a Fermi-Dirac distribution causes some carriers to scatter to higher energies than this; his effect is stronger, the broader the distribution function. Hence more and more carriers are no longer caught in the well and easily scatter out; subsequently they may decay nonradiatively, emit PL at the bulk GaAs 1s resonance, or lose energy and fall back into the quantum well.

5.3.2 Carrier Temperature T and Cooling

The carrier temperature is extracted from the slope of the continuum emission as described in Section 3.3.1. The temporal evolution of the extracted carrier temperature is shown in Figure 5.9 on a semi-logarithmic scale; exemplarily, four carrier densities, $2.0 \times 10^{11} \text{ cm}^{-2}$ (squares), $1.1 \times 10^{10} \text{ cm}^{-2}$ (circles), $7.9 \times 10^8 \text{ cm}^{-2}$ (triangles), and $2.9 \times 10^8 \text{ cm}^{-2}$ (stars) are shown.

Even though the carriers are injected with the same excess energy for all experiments, already the first experimental values vary: The higher the density, the higher the temperature. The functional form of the following decay behavior is similar for all densities: An exponential fit of the form $C_1 + C_2 \times \exp(-t/\tau)$ with C_1 and C_2 constants, a decay constant $\tau \approx 0.5 \text{ ns}$ is found. Hence the temperature at each specific time are lower for smaller densities than for elevated densities. However, under no circumstances is the lattice temperature of 4 K reached [58, 47, 59]. The lowest

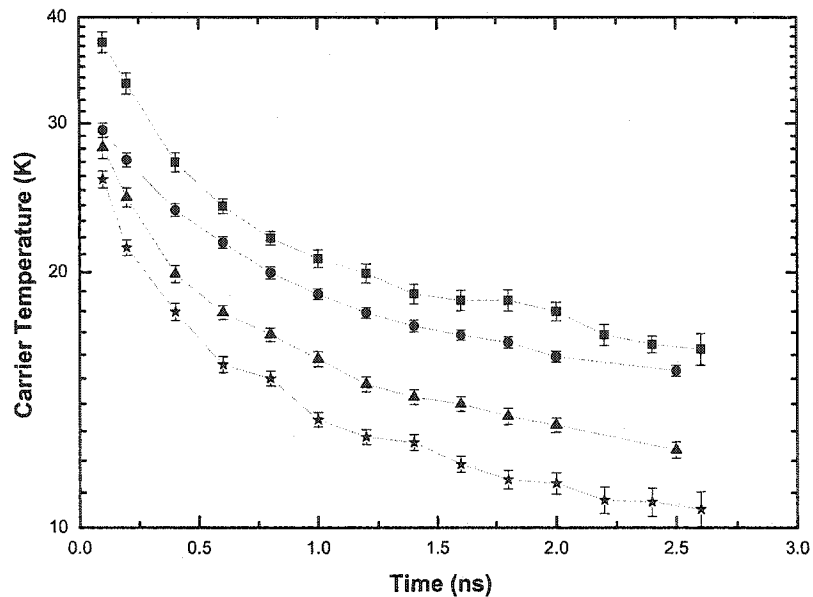


Figure 5.9: Temporal evolution of the carrier temperature at a lattice temperature of 4 K. The initial carrier densities are (from top to bottom): $2.0 \times 10^{11} \text{ cm}^{-2}$ (squares), $1.1 \times 10^{10} \text{ cm}^{-2}$ (circles), $7.9 \times 10^8 \text{ cm}^{-2}$ (triangles), and $2.9 \times 10^8 \text{ cm}^{-2}$ (stars). The lines are a guide to the eye.

experimental value determined here is $10.5 \pm 0.5 \text{ K}$, 2.8 ns after excitation with an initial carrier density $n_{\text{eh}} = 2.9 \times 10^8 \text{ cm}^{-2}$.

An initially hot distribution cools towards the lattice temperature by scattering with acoustic and for larger excess energies ($>36 \text{ meV}$) also longitudinal-optical (LO) phonons. The typical scattering times are on the order of several hundreds of picoseconds [60] and below 100 fs [61], respectively. However apparently in contradiction to that, for 4 K, the lattice temperature is never reached. This behavior can be at least partially explained when considering the decay of free carriers through the channel of the 1s exciton resonance. It lies 8 meV below the band edge. Energy conservation requires this energy difference, corresponding to 96 K, to be accounted for. It is absorbed by the remaining free carriers, heating the remaining plasma.

For higher lattice temperatures, the carrier temperature equilibrates with the lattice. Exemplary cooling curves are shown in Figure 5.10, all taken with an initial

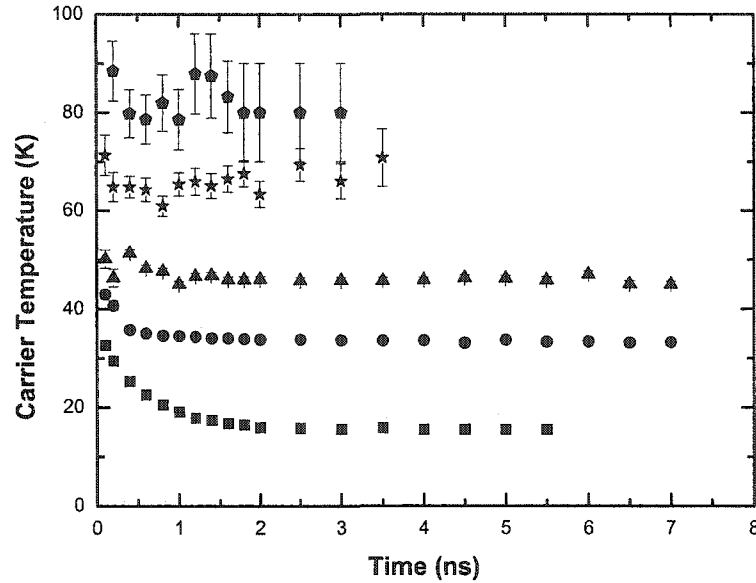


Figure 5.10: Temporal evolution of the carrier temperature for five different lattice temperatures: 80 K (pentagons) 70 K (stars), 50 K (triangles), 30 K (circles), and 4 K (squares). The initial carrier density for all measurements is $8.2 \times 10^9 \text{ cm}^{-2}$.

carrier density of $8.2 \times 10^9 \text{ cm}^{-2}$. For 80 K (pentagons), 70 K (stars), and 50 K (triangles), the carriers equilibrate very rapidly with the lattice; for 30 K this takes about 1 ns. The 4 K curve is shown for completeness (squares). Due to the shorter luminescence lifetimes at high temperature, the temperatures can only be extracted up to 3.5 ns or 3 ns after excitation for 70 K and 80 K lattice temperature, respectively.

5.3.3 Ratio 1s to Continuum-Edge Emission: R

Studying the ratio of 1s to continuum-edge emission as a description for each spectrum presents a possibility to examine dependencies of the photoluminescence from a purely experimental point of view. Emission above the bandgap energy can be attributed to the continuum emission of free carrier plasma. At the 1s exciton resonance however both bound incoherent excitons as well as the plasma contribute.

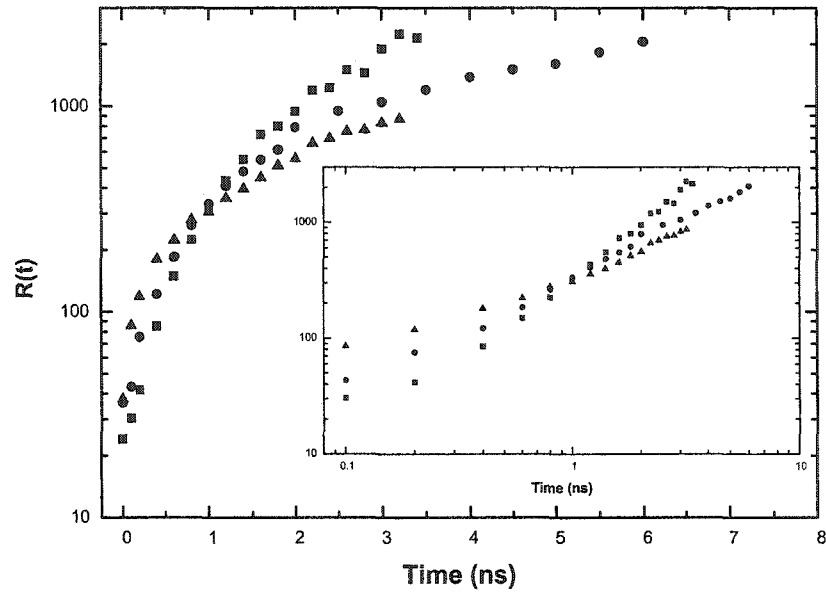


Figure 5.11: Temporal evolution of the ratio of 1s to continuum emission edge R for 4 K lattice temperature on a semi-logarithmic scale. The initial carrier densities are $2.0 \times 10^{11} \text{ cm}^{-2}$ (squares), $1.1 \times 10^{10} \text{ cm}^{-2}$ (circles), and $2.9 \times 10^8 \text{ cm}^{-2}$ (triangles). The inset shows the same data on a double-logarithmic scale.

The two are connected by calculating their ratio and studying its dynamics; a detailed description of the concept is given in Section 3.3.2.

Time Dependence of R : $R(t)$

The natural approach to R is to study its variation with evolution of time. In a first step, only data taken at 4 K lattice temperature are considered. Exemplary curves for various initial carrier densities are shown in Figure 5.11. While, depending on the carrier density injected, the peak emission at the 1s resonance rises for at least a few hundreds picoseconds and then starts to decay, $R(t)$ shows a monotonous increase. The functional shape of the $R(t)$ curve however is in itself dependent on the initial carrier density. At high excitation densities, where the spectrum is dominated by plasma emission (see Chapter 6), $R(t)$ slowly rises from roughly ten to several thousand. For lower densities, initially after excitation $R(t)$ starts out a factor of

two higher than for the high densities. At about 1 ns, curves for all densities cross at about $R(1 \text{ ns}) \approx 400$.

On the double-logarithmic scale, $R(t)$ has approximately a linear functional form for all initial carrier densities. The slope decreases with carrier density; the crossing at 1 ns can again be seen very clearly. While the semi-logarithmic scale appears to suggest that lower densities approach saturation, the double-logarithmic plot does not indicate such a behavior.

Temperature Dependence of $R(t)$

At elevated lattice temperatures, $R(t)$ shows significantly less dynamics. In Figure 5.12, the temporal evolution of R is shown for 30 K (bottom), 50 K (middle) and 80 K (top) lattice temperatures for several different initial carrier densities. The plots are similar to Figure 5.11, and the insets again show the same data sets on a log-log scale. Note the different time scales for the plots; due to the different decay times (see Section 5.3.1), the data are taken only for short time delays with increasing temperature.

Initially, the values are between ten to twenty for all elevated lattice temperatures, similar to the low temperature case. For longer time delays however, the values of R are much smaller than for 4 K. At 30 K lattice temperature, $R(t)$ saturates at ≈ 60 within 2 ns. For even higher densities the saturation is reached faster and at a lower value, $R(t) \approx 23$ for 50 K. At 80 K the long-time limit is $R(t) \approx 12$. Here $R(t)$ shows hardly any dynamics. This is consistent with the fact that the carrier temperatures are also similar at early time; especially for cold lattices, they are much larger than the lattice temperature. While at 4 K lattice temperature, the $R(t)$ curves are very density dependent, this also becomes less pronounced with increasing lattice temperature.

The R analysis suggests that the system dynamics are different at 4 K than for the elevated lattice temperatures. Initially after excitation into the continuum, a hot plasma is created; the corresponding R values are between ten and twenty for

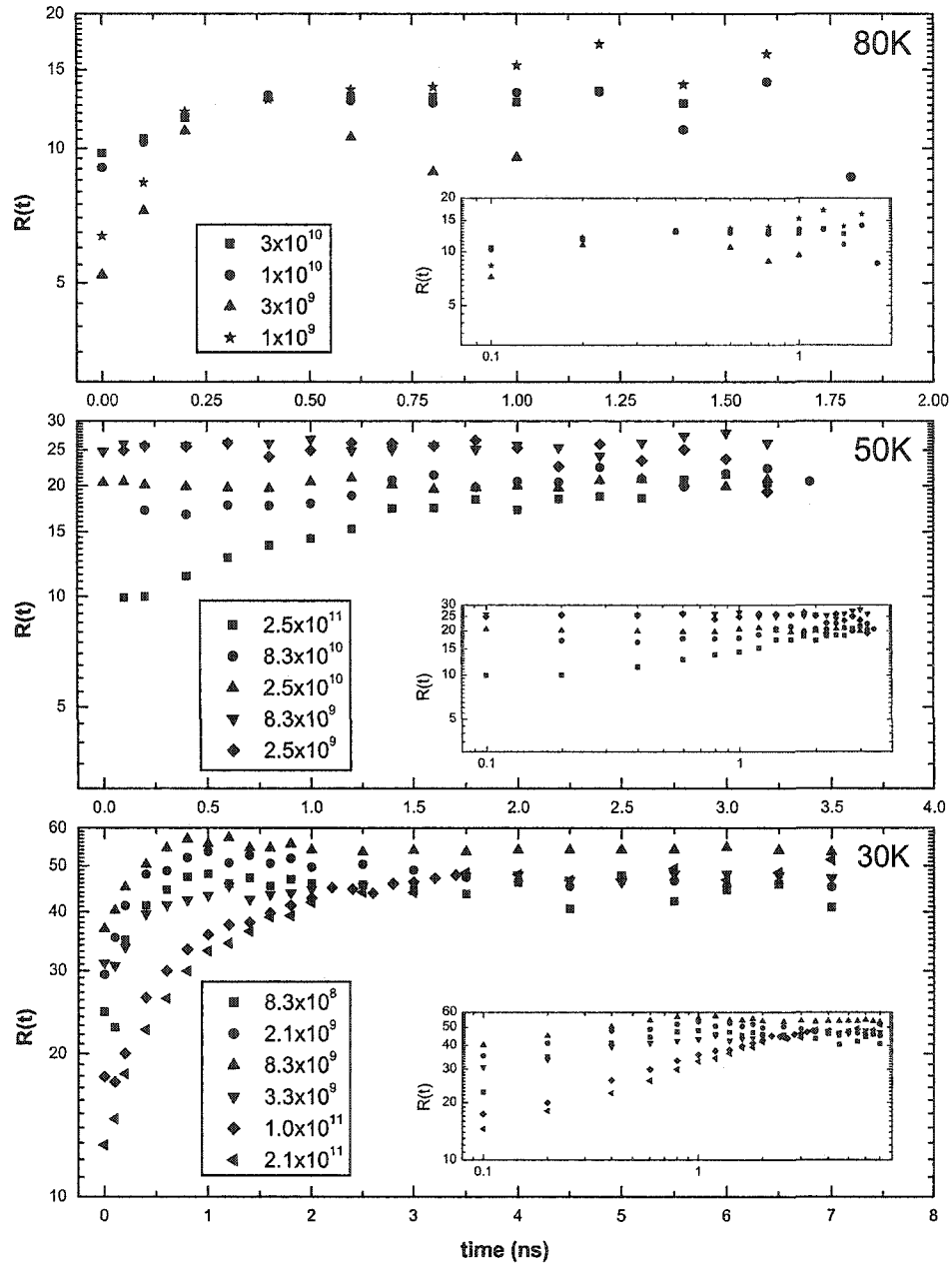


Figure 5.12: Temporal evolution of R for higher lattice temperatures: 30 K (bottom), 50 K (middle), and 80 K (top). The graphs show the densities on a semi-logarithmic scale, the insets on a double-logarithmic scale. Note the varying x- and y-scales for each lattice temperature. The carrier densities are given in the corresponding legends in cm^{-2} .

all carrier densities. For 80 K lattice temperatures the R values are in the same range for all delay times, implying an exclusive decay of the free plasma without any excitons. The analysis in Chapter 6 suggests that significant amounts of excitons only contribute at the lowest lattice temperature. Under these conditions the largest R values are reached. Hence it may be concluded that also for the other lattice temperatures hardly any excitons are present in the system. However, R also shows a decreasing trend with lattice temperature. Therefore no conclusive statements are possible without considering temperature effects.

5.4 β Analysis

The combination of absorption and photoluminescence measurements leads to the extraction of the β factor as described in Section 3.3.3. The calculations used for comparison presented in Chapter 6 rely on thermodynamic equilibrium considerations. Therefore it is necessary that quasi-equilibrium can be assumed. Especially for short time delays after excitation, cooling effects are very pronounced [58], and the interpretation has to be done carefully keeping this in mind. For this reason, although the experimental β is shown for short time delays also, the main emphasis of the analysis lies on time delays of 1 ns or greater.

5.4.1 Density Dependence of β

In order to make a meaningful comparison of the β values amongst themselves, their behavior versus carrier density is studied. For this purpose, the values 1 ns after the excitation are chosen.

On the face of it, the choice of 1 ns may seem completely arbitrary. However it proves to be a convenient choice. For shorter time delays, the carrier temperature is still very much hotter than the lattice at 4 K. By 1 ns, most of the cooling has occurred [58], reaching values between 13.5 K at the lowest and 20.7 K at the highest density; see Figure 5.9 and Figure 5.10. Although the temperatures across the whole

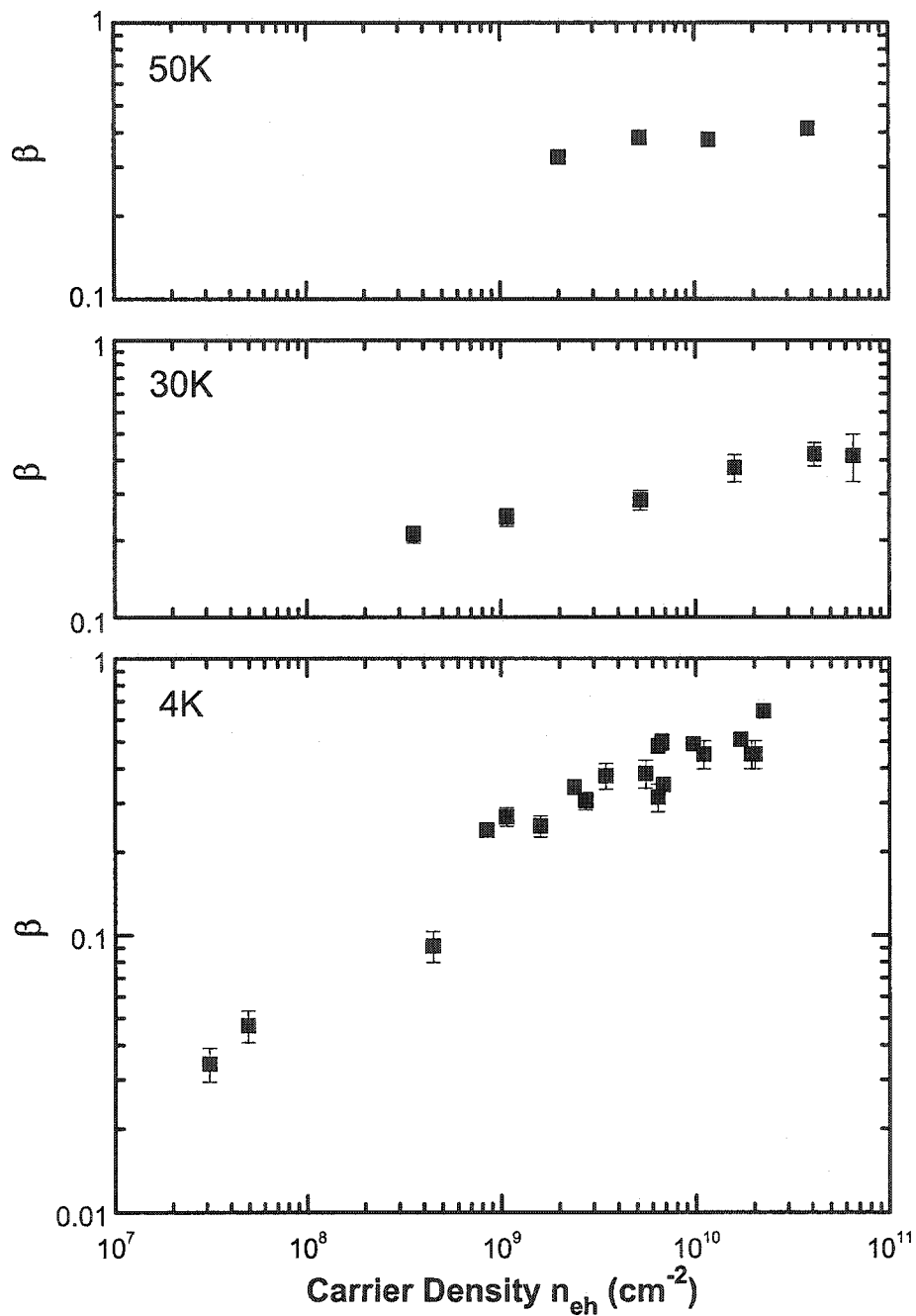


Figure 5.13: β factor versus carrier density for different lattice temperatures on a double-logarithmic scale (from top to bottom): 50 K, 30 K, and 4 K. The data set at 4 K contains data points taken 1 ns after nonresonant excitation; the others have data points at various time delays.

density range under investigation vary by 8 K, this difference does not decrease for longer times.

Also, the theory used for comparison in the following chapter avoids numerical restrictions by making use of an adiabatic approximation. Therefore, times shortly after excitation cannot be interpreted with the approach used in Chapter 6 of this thesis, so only longer time delays are considered. This results in lower signal amplitudes and hence also worse signal-to-noise ratios; especially the continuum fit is less reliable for increasing time delays. Furthermore the density calibration is less accurate. For low densities, the carrier-induced change in absorption is small again making noise more significant.

Consequently, Figure 5.13 shows β values, taken at a time delay of 1 ns, versus carrier density, corresponding to 1 ns after nonresonant excitation. Both graphs are plotted on double-logarithmic scales. The data were taken for different lattice temperatures, 4 K (bottom), 30 K (middle), and 50 K (top). In addition, a complete set of data was taken at 80 K lattice temperature. Here, the density conversion using corresponding $\Delta\alpha L$ values starts to fail; therefore under these conditions, meaningful β versus carrier density is not possible.

At the lowest lattice temperature, $\beta(1\text{ ns})$ is taken over four orders of magnitude in density. Its dynamics covers slightly over one order of magnitude. At low and intermediate densities, β increases with density. For elevated densities the curve approaches saturation; above $\sim 3 \times 10^9\text{ cm}^{-2}$, β is more or less constant (see also Figure 6.1).

The dynamics of the data taken at 50 K and 30 K lattice temperature is much smaller, about a factor of two. The overall lower signal intensity of the photoluminescence limits the accessible density range within reasonable integration times. The slower decay as well as the energetic position of the laser spectrum allow for carrier densities larger than at 4 K lattice temperature. For both cases the carrier temperatures have equilibrated with the respective lattice temperatures.

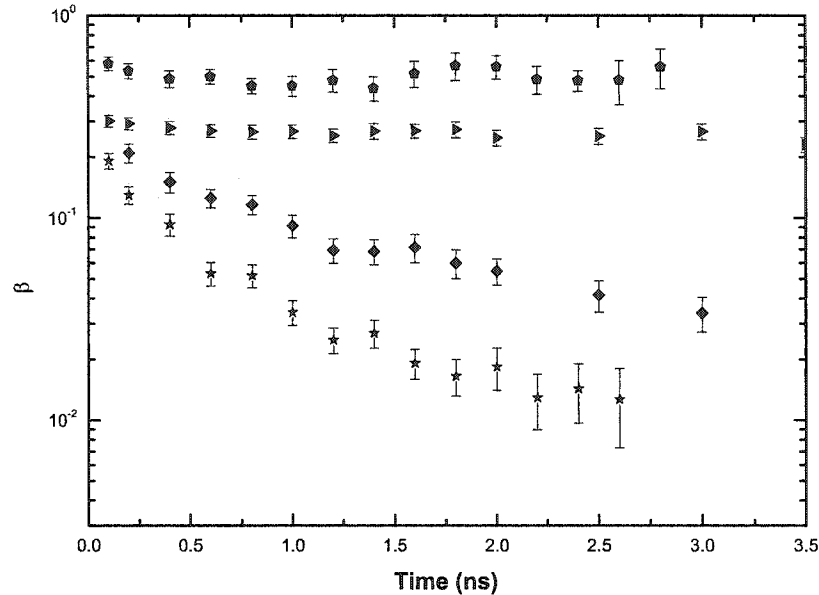


Figure 5.14: Temporal evolution of β for 4 different initial carrier densities: $2.0 \times 10^{11} \text{ cm}^{-2}$ (pentagons), $1.1 \times 10^{10} \text{ cm}^{-2}$ (triangles), $7.9 \times 10^8 \text{ cm}^{-2}$ (diamonds), and $2.9 \times 10^8 \text{ cm}^{-2}$ (stars).

The decay of β with density is slower for higher lattice temperatures. The high density values do not vary; for densities of about $5 \times 10^{10} \text{ cm}^{-2}$, β is ~ 0.5 . Deviations are found for lower carrier densities. Already at an intermediate density of $2 \times 10^9 \text{ cm}^{-2}$, cooling from 50 K to 18 K reduces β by a factor of two.

In these experiments, the density dependence can be further investigated by studying the temporal evolution of β as shown in Figure 5.14. β is plotted versus time delay after nonresonant excitation in the continuum on a semi-logarithmic scale for four different initial carrier densities: $2.0 \times 10^{11} \text{ cm}^{-2}$ (pentagons), $1.1 \times 10^{10} \text{ cm}^{-2}$ (triangles), $7.9 \times 10^8 \text{ cm}^{-2}$ (diamonds), and $2.9 \times 10^8 \text{ cm}^{-2}$ (stars). These are representative across the density range covered in the experiments with a lattice temperature of 4 K. Because of the pulsed nature of the experiment, the carrier density in the system decays with time.

For intermediate and elevated initial carrier densities, β shows only very little dynamics with time, as can be seen from the top two data sets in Figure 5.14. It stays

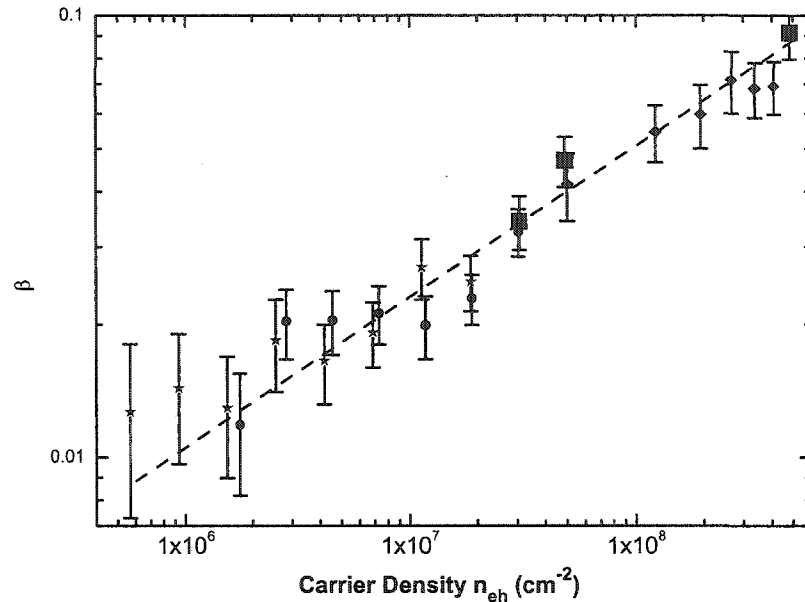


Figure 5.15: Low density behavior for β with $T=4$ K. The dashed line shows a linear regression through the 1 ns values (squares). For three initial carrier densities, $7.9 \times 10^8 \text{ cm}^{-2}$ (rhombi), $4.1 \times 10^8 \text{ cm}^{-2}$ (circles), and $2.9 \times 10^8 \text{ cm}^{-2}$ (stars), data points for delay times longer than 1 ns are shown.

almost constant, maybe decaying slightly, thus implying that a quasi steady-state has been reached. The initial values however are larger for higher densities. With decreasing densities, β decays with time; data sets with lower initial carrier density have a slightly steeper slope.

Figure 5.15 shows β versus carrier density for 4 K lattice temperature and low densities on a double-logarithmic scale; in addition to the 1 ns data (squares), β values at several time delays are also shown. To reduce cooling related effects, values for delay times smaller than 1 ns are excluded. The functional behavior follows an interpolated curve through the 1 ns values, as indicated by the dotted line. Here the decay of β is thus fully parameterized by the density decay. This shows that the values of β depend upon the excitation density and temperature, not past history. Thus a comparison with quasi steady-state theories is possible. This is important since thermodynamic equilibrium in the KMS sense discussed above is never reached:

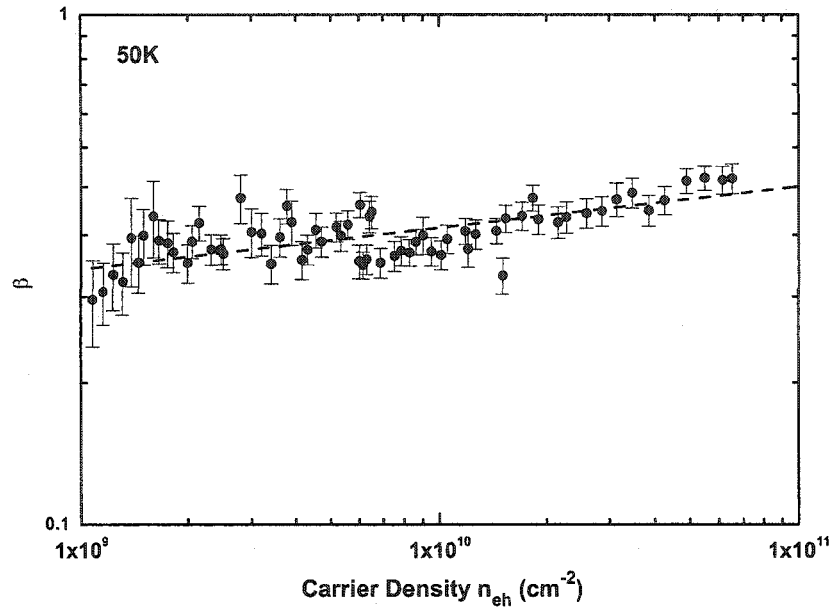


Figure 5.16: β versus carrier density for 50 K lattice temperature. Values for all different time delays are shown.

β is always considerably less than unity at all times for which the photoluminescence is measurable. The 1s emission is always weaker than that predicted by KMS.

For higher lattice temperatures, a similar parameterization can be applied. In Figure 5.16, β is shown for all time delays after nonresonant excitation and a lattice temperature of 50 K. For each time step, the density values are calculated using Figure 4.4. Cooling effects are much less pronounced at these higher densities (see Figure 5.3.2), therefore justifying the use of delays < 1 ns.

5.5 Dependence on Pump Excess Energy ΔE

ΔE describes the excess energy of the pump relative to the 1s resonance $\Delta E = E_{\text{pump}} - E_{1s}$. All excess energies presented here are larger than the excitonic binding energy. For different excess energies ΔE , the absorption at the pump energies varies. In order to measure the influence the different excess energies have on the system, especially on β , comparable carrier densities need to be achieved; the

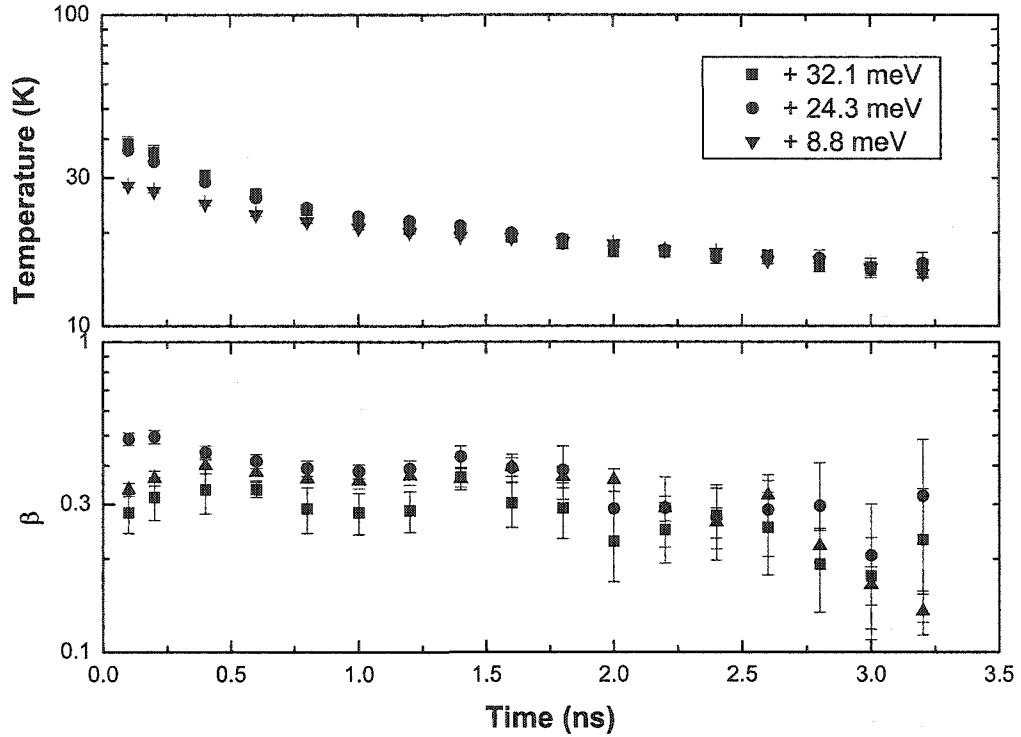


Figure 5.17: Carrier temperature (top) and β factor (bottom) versus time for 4K lattice temperature. The pump energies are 8.8 meV (squares), 24.3 meV (circles), and 32.2 meV (triangles), the calculated initial carrier density in all cases is $1.2 \times 10^{10} \text{ cm}^{-2}$.

time-integrated pump power must be adjusted accordingly. Especially for large excess energies this is difficult since the substrate distorts the quantum well absorption and other resonances like the 1s light-hole come into play.

The most straight-forward effect of different pump energies are different initial carrier temperatures. Increasing excess energy means larger excess energy and hence hotter carriers. However on the time scales of interest, the influence of the initial hotter carrier temperature is small. The extracted carrier temperature for three different excess energies, $\Delta E = 8.8 \text{ meV}$ (squares), $\Delta E = 24.3 \text{ meV}$ (circles), and $\Delta E = 32.2 \text{ meV}$ (triangles), are shown in the top graph in Figure 5.17 on a semi-logarithmic scale. Only at very early times, much shorter than 1 ns, is a difference

observed. For time delays larger than 1 ns, the evolution of the carrier temperature is similar for all pump energies.

For β , no significant influence of the pump energy could be observed either, as can be seen from the bottom of Figure 5.17; here corresponding β values are shown, also on a semi-logarithmic scale. Only the β factor for the largest pump energy appears to be slightly lower. However the uncertainty of the density calibration decreases with pump excess energy and is hence largest in this region. A small overestimation of the carrier density can also explain the small deviation.

5.6 Time-Resolved Photoluminescence after Resonant Excitation

Naively, resonant excitation could be considered as a special case of the excess energy dependence; the pump energy is changed in comparison to previously presented experiments. However, in this case the excitation is not at all into the band, but directly into, literally “in resonance with”, the 1s state. In addition the dynamics in the semiconductor is changed.

Resonant excitation introduces a coherent polarization at $q \approx 0$ in the semiconductor. It virtually instantaneously starts to decay and dephase. The latter causes an incoherent excitonic population at all q to build up. Subsequently, the population itself decays.

It should be stressed again that the spectra are taken in cross linear polarization geometry. Nevertheless the signal in the detector rises instantaneously within the achieved time resolution. This can be seen as an indicator of fast dark to bright scattering of excitonic states.

The spectrum of the 3 ps pump pulse is slightly wider than the 1s absorption line. To ensure no higher energy states are excited, the pump spectrum is detuned slightly below the exciton resonance. Multi-photon processes offer an additional nonresonant channel for nonresonant excitation. In GaAs based systems, they are significantly less efficient than direct excitation by a factor $\approx 10^{-7}$ [62].

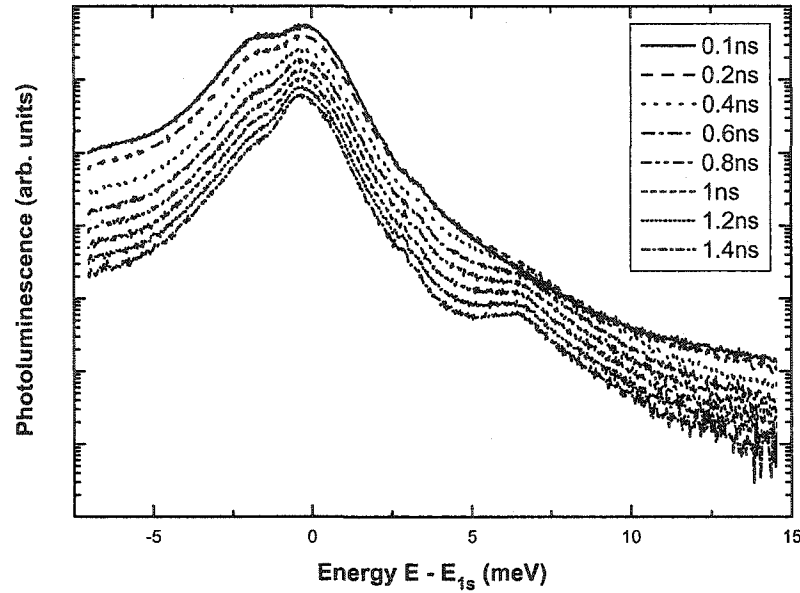


Figure 5.18: Photoluminescence spectra after resonant excitation for several time delays at a lattice temperature of 4 K. The initial carrier density is $1.0 \times 10^{10} \text{ cm}^{-2}$.

Typical emission spectra are shown in Figure 5.18. At a lattice temperature of 4 K, the sample is excited resonantly with a carrier density of about $1.0 \times 10^{10} \text{ cm}^{-2}$. The most prominent feature is the 1s emission peak at zero on the renormalized energy scale. At early times, the emission is very broad, and the high energy tail is Lorentzian in shape. An impurity state causes a second peak 2 meV below the resonance (c.f. Chapter 3). Since it is also resonantly pumped, the emission rises much faster than when fed after nonresonant excitation.

After about 0.4 ns the density has decayed enough for the 2s resonance to be resolved. Continuum emission can be detected instantaneously within the time resolution of the system. However for 4 K lattice temperature, its amplitude is about two orders of magnitude lower than for nonresonant excitation into the continuum itself. This difference decreases with increasing lattice temperature; at 30 K the spectra are already very similar.

5.6.1 Decay of 1s and Continuum Luminescence

Another significant difference between resonant and nonresonant excitation can be found in the luminescence dynamics. For early times, the 1s luminescence overshoots (see left hand side of Figure 5.19). This is partially due to scatter of the resonant excitation pulse; also the polarization reradiates fast [63]. The second, slower decay is still faster than in the nonresonant case. For 4 K lattice temperature it is about twice as fast, 0.66 ns. This value increases with lattice temperature, similar to the nonresonant case, reaching 2.0 ns at 30 K. Here the deviation is much smaller.

The decay of the polarization is quasi-instantaneous on the time scales considered. The polarization partially reradiates and partially creates incoherent excitons in all momentum states. Bright excitons, that is excitons with momentum states $q_x \leq q_{\text{photon}}^{\text{max}}$, decay fast, with a lifetime of 13 ps. The decay of the whole population is then dominated by the dark to bright scattering rates, which is still slightly faster than the plasma decay [64, 66, 67, 65]. For elevated lattice temperatures, the excitonic population can also decay into a free electron hole plasma via acoustic-phonon coupling. This decays slowly, hence lengthening the lifetime, ultimately towards the nonresonant excitation limit.

The temporal evolution of the continuum luminescence is shown on the right hand side of Figure 5.19. It does not peak immediately, but after a few hundreds of picoseconds at low temperatures. Especially at early times the Lorentzian tails of the 1s emission are still prominent at the continuum edge, 8 meV above the resonance. Since the emission measured at the continuum edge is about two orders of magnitude smaller than in the nonresonant excitation experiments, the influence of the 1s tail is much larger. It is experimentally impossible to distinguish the two. This is a possible explanation for the earlier peak time at 4 K than at 15 K.

At 30 K the decay starts instantaneously within the time resolution. Here also the lifetime of 2.0 ns is the same as the 1s lifetime at resonant excitation as well as similar to the continuum decay in the nonresonant case. The numbers do not

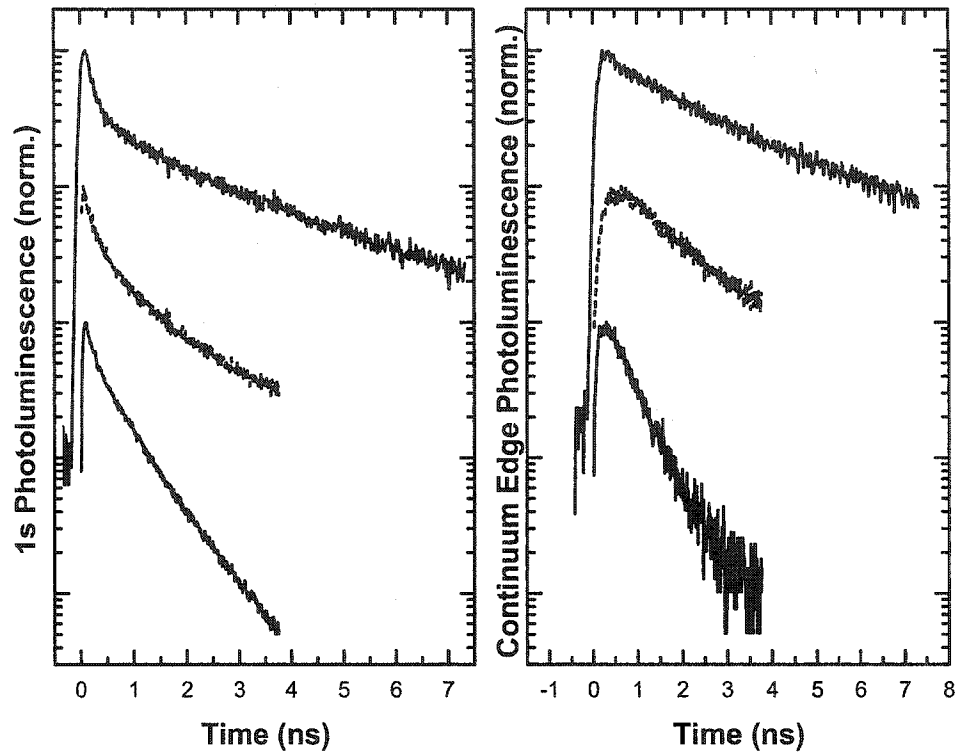


Figure 5.19: Temporal evolution of the 1s resonance peak height (left) and continuum edge (right) at several lattice temperatures after resonant excitation (from top to bottom): 30 K, 15 K, and 4 K. The initial carrier density is $1.0 \times 10^{10} \text{ cm}^{-2}$ for all data sets. The curves are normalized and offset by one order of magnitude for clarity. The decay constants of the second, slower decay are given in Table 5.4.

lattice temperature	1s lifetime	continuum luminescence
4 K	0.66 ns	0.55 ns
15 K	0.99 ns	1.34 ns
30 K	2.0 ns	2.0 ns

Table 5.4: Photoluminescence lifetimes of the 1s and continuum-edge emission after resonant excitation for several lattice temperatures, extracted from the time traces shown in Figure 5.19.

rigorously agree with those given in Table 5.3; the carrier densities vary as well. The decay times for the experiments with resonant excitation are given in Table 5.4.

5.6.2 Carrier Temperature T

The temperature dynamics for resonant excitation is different from interband excitation. The carriers are injected cold; the excitation wavelength is tuned directly on the absorption resonance hence eliminating all excess energy.

Figure 5.20 shows the extracted carrier temperature versus time for three different lattice temperatures: 4 K (squares), 15 K (circles), and 30 K (triangles). The decay times are much faster at lower temperatures, for 4 K the fits only yield reliable results during the first 1.5 ns. This time increases to 7 ns for 30 K lattice temperature.

Most curiously, at a lattice temperature of 4 K (squares), the temperature dynamics after resonant excitation show a cooling behavior. Initially after excitation, the continuum slope yield a temperature of ~ 30 K, rapidly cooling by 10 K in the next few hundred picoseconds. This can be seen as some evidence for two-photon absorption of the pump pulse; the nonresonantly excited carriers subsequently cool. Additionally, as some cold excitons are converted into free electron-hole plasma, the system cools. The observed cooling should therefore be regarded as significant and not an artefact. However, for resonant excitation the continuum emission is generally even weaker than for nonresonant excitation. Its low amplitude may make it sensitive to influence from the 1s resonance: The homogeneous broadening of the 1s resonance is manifested in an underlying Lorentzian contribution to the lineshape. The resulting high and low energy tails, though small, may significantly distort a signal of equal or lesser strength. A linear fit to a Lorentzian line $\frac{2}{\pi} \frac{\omega}{4x^2 - \omega^2}$, 8 meV and above yields temperatures in a similar range. It should again be noted that the continuum emission is very weak, so that these findings may be slightly distorted and not too much attention should be paid to the local minimum 0.6 ns after excitation.

For higher lattice temperature, the cooling dynamics are inverted. The temperature rises with time, reaching its steady state value by 1 ns. The carriers never

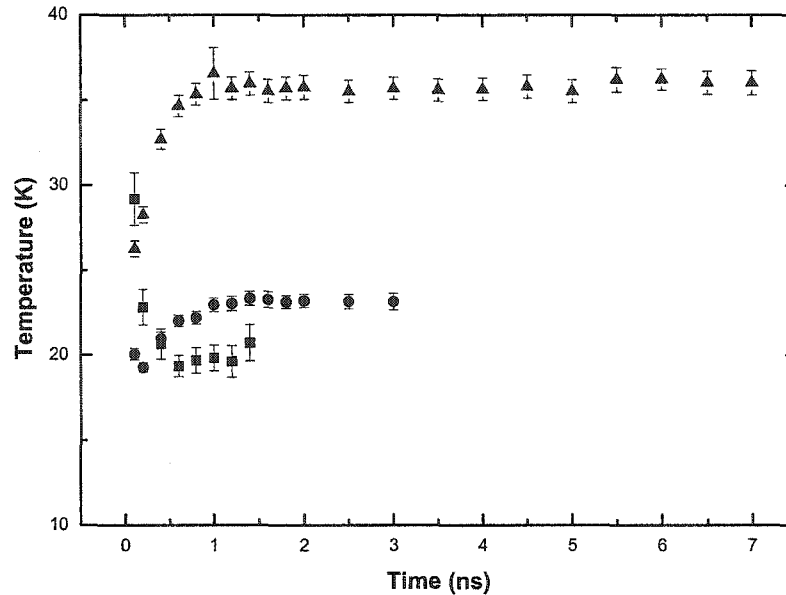


Figure 5.20: Temporal evolution of carrier temperature T after resonant excitation for an initial carrier density of $1.0 \times 10^{10} \text{ cm}^{-2}$ and three different lattice temperature: 4 K (squares), 15 K (circles), and 30 K (triangles).

equilibrate with the lattice temperature. At both 15 K and 30 K, larger values are reached. In the latter case the continuum tail converges towards 36 K, very similar to the nonresonant case (c.f. Section 5.3.2).

5.6.3 $R(t)$ Analysis

Analogous to the nonresonant excitation case (Section 5.3.3), the comparing the 1s peak emission to the continuum-edge luminescence is an attempt to identify variations in their dynamics. The ratio R is plotted versus time in Figure 5.21 for three different lattice temperatures 4 K, 15 K and 30 K and an initial carrier density of $1.0 \times 10^{10} \text{ cm}^{-2}$ for all cases. The inset shows the same data in a double-logarithmic plot. The shorter delay times accessible at low temperatures are again due to the faster decay limiting the signal amplitude and signal to noise.

For lower lattice temperatures, the ratio R is larger. Although the curves are clearly offset with respect to each other, their functional form is somewhat similar,

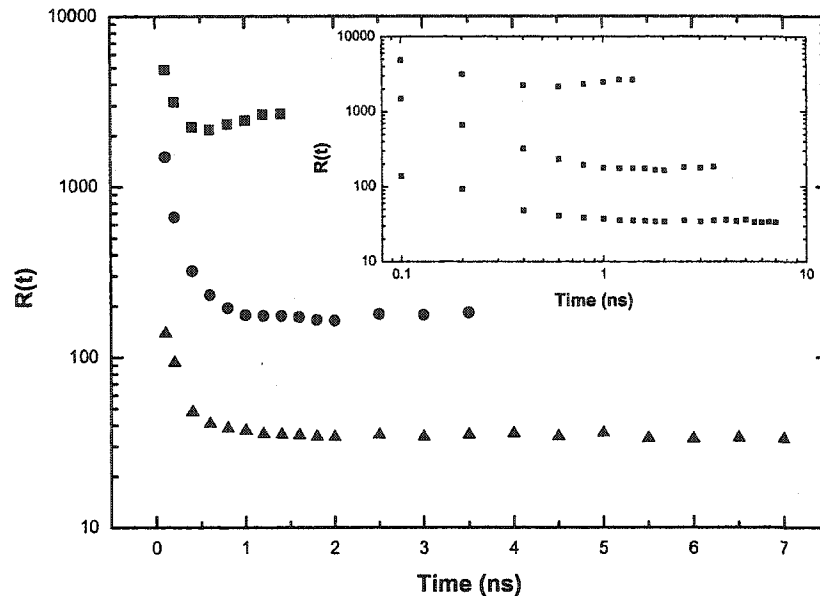


Figure 5.21: Temporal evolution of 1s to continuum emission edge ratio $R(t)$ after resonant excitation for an initial carrier density of $1.0 \times 10^{10} \text{ cm}^{-2}$ and three different lattice temperature: 4 K (squares), 15 K (circles), and 30 K (triangles) on a semi-logarithmic scale. Inset: same on double-logarithmic scale.

as can be seen in the inset. After an initial fast decay, R reaches a steady state value by 1 ns. This is in sharp contrast to the dynamics of R for nonresonant excitation described in Chapter 5.3.3. For 4 K lattice temperature, the values at early times are much larger in the case of resonant excitation; also in the nonresonant case, no steady state is reached in the time range investigated.

For 30 K lattice temperatures, R values for both resonant and nonresonant excitation converge towards $R \approx 30$. Here the main difference is the early-time dynamics. While $R(t)$ increases for short time delays of about 1 ns, the resonant data starts out higher and then decreases. The results taken for the intermediate lattice temperature of 15 K lie in between the two other curves. Starting out at about $R \approx 1300$, R has fallen below $R \approx 200$ within 1 ns, reaching a steady state.

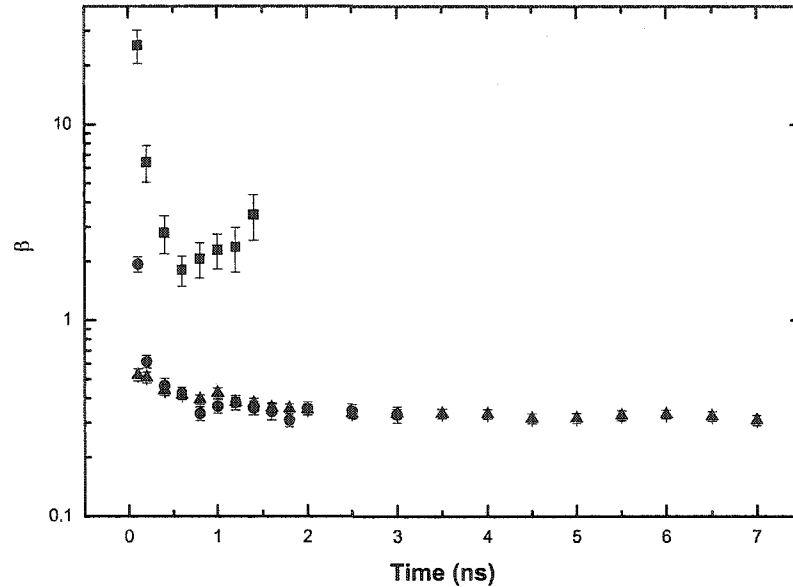


Figure 5.22: Temporal evolution of β after resonant excitation for an initial carrier density of $1.0 \times 10^{10} \text{ cm}^{-2}$ and three different lattice temperature: 4 K (squares), 15 K (circles), and 30 K (triangles).

5.6.4 β Analysis

As shown in the two previous sections, the dynamics of both the carrier temperature and R for resonant excitation deviate significantly from the nonresonant case. Again, now the β factor is used for comparison, combining the two as well as eliminating effects due to the varying oscillator strength. A definition and detailed explanation of β can be found in Section 3.3.3.

The temporal evolution of β is shown in Figure 5.22 on a semi-logarithmic scale. For an initial carrier density of $1.0 \times 10^{10} \text{ cm}^{-2}$, three different lattice temperatures are examined; data points taken at 4 K are shown as squares, 15 K as circles and 30 K as triangles. The different time spans for which β is extracted are due to the decay times, which decrease with lattice temperature, in the range under investigation.

The most important observation is that for the first time β values larger than one are found. For 4 K lattice temperature, β starts out at $\beta \approx 30$ immediately after

excitation; within 0.5 ns, it has fallen to $\beta \approx 2$, but stays larger than one for all times.

When arguing in thermal equilibrium terms, this means that too many 1s excitons are still present in the system relative to the value expected for thermal equilibrium. While for nonresonant excitation free carriers are created by optically exciting into the band, the resonantly excited polarization has already completely dephased within 100 ps and an incoherent population remains. Of course, this conclusion automatically implies that too few excitons form after nonresonant excitation to give thermal equilibrium; this question will be addressed in the following chapter.

With increasing lattice temperature, the functional form of the β versus time curve approaches the nonresonant data presented above. For 15 K, only the first value, 0.1 ns after excitation, is larger than unity, all others converge towards $\beta = 0.33$. The largest lattice temperature of 30 K completely resembles the β behavior for nonresonant excitation. Intriguingly, β decays with time for all cases, although only at the lowest lattice temperature cooling is observed, while for 15 K and 30 K the temperature actually rises. Therefore it can be concluded that for longer times the system always tries to reach a plasma-dominated state.

CHAPTER 6

COMPARISON EXPERIMENT - THEORY

The experimental findings are explained with a microscopic theory. The calculations presented here were performed by Dr. Walter Hoyer, Prof. Mackillo Kira and Prof. S.W.Koch in his research group at the Philipps-Universität Marburg in Germany.

The main goal of the analysis is to evaluate the influence of excitonic contributions on the 1s photoluminescence. The attenuation factor β is used to compare experimental and theoretical results. It describes the suppression of the ratio of photoluminescence and absorption taken under identical conditions relative to the value expected from KMS. The definition of β (Section 3.3.3) eliminates the influence of the dipole-matrix-element of the 1s exciton resonance. Inhomogeneous broadening is not considered and only the main features in the line shape of photoluminescence and absorption spectra are reproduced.

The experimental β as a function of density and temperature is compared to theoretical values. Unlike in the experiment, it is possible in the theory to clearly distinguish between plasma and excitonic contributions to the photoluminescence emitted at the 1s resonance. In a first step, using solely sample specific parameters such as dipole matrix element and excitonic binding energy, the pure plasma value for β is calculated. Then if necessary for agreement with the experiment, excitonic contributions are included. It should be again stressed that no free fitting parameters are necessary or included in the analysis.

Initially, the question is whether the experimental findings can be explained using a pure plasma source. Therefore in Figure 6.1, the β factor extracted from the experiment is compared to the pure plasma calculation. The data shown on top are taken at a lattice temperature of 50 K. The carrier temperatures extracted from the experimental continuum tail for all data points shown are (50 ± 2) K; all

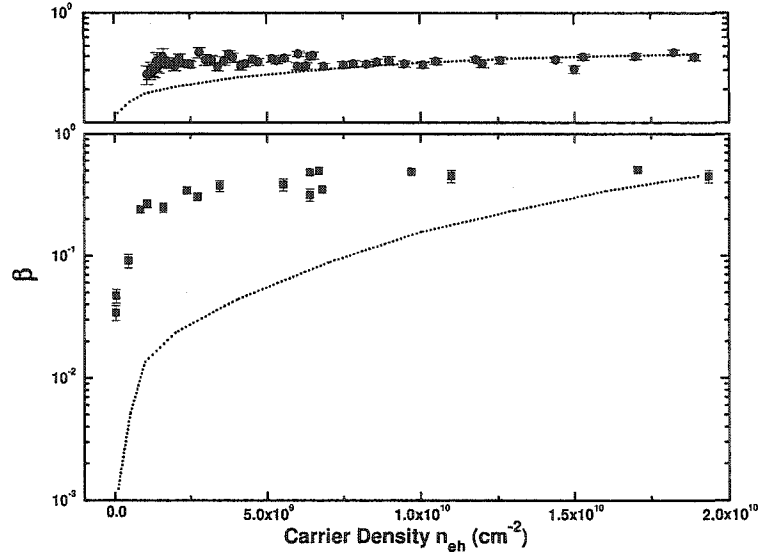


Figure 6.1: β versus carrier density. Full squares refer to experimental values taken at 1 ns after nonresonant excitation at a lattice temperature of 4 K. The densities refer to densities at 1 ns. The theoretical values (dotted line) are calculated using the PL formula (2.4) for a pure e-h plasma with a carrier temperature of (16 ± 2) K. Top: same for 50 K lattice temperature, but data points for all time delays are shown. The density for each time step is calculated according to Chapter 4.3. The extracted e-h plasma temperature is (50 ± 2) K; the theoretical curves are computed for a carrier temperature of 48 K.

cooling has occurred in the first 100 ps after excitation (Figure 5.10). β values for several time delays are shown in one graph. As shown in Section 5.6.4, the β versus density relation is fully parameterized by the density at this temperature. The carrier density for each measurement was extracted from the calibration curve as described in Section 4.3. The carrier temperature used for the calculations is 48 K. Over most of the density range under investigation, good agreement between the pure plasma calculation and the experiment is found.

The situation is different at a lattice temperature of 4 K. The experimental data and pure plasma calculation β are shown in the bottom part of Figure 6.1. Here only experimental values 1 ns after excitation are shown as a function of density, c.f. Section 5.4.1. The extracted carrier temperatures vary from 13.5 K at the lowest density to 20.7 K at the highest density. The theoretical curve is calculated using

carrier temperatures between 14 K and 18 K. Even at a low lattice temperature of 4 K, the high density results agree with the pure plasma calculation; note that at the high density under investigation, the exciton absorption is still very pronounced with the peak reduced by only 25 % (Figure 5.1). At lower densities β is considerably lower, i.e. deviations from KMS (see Section 3.3.3) around the 1s-exciton resonance are even larger than in the experiment.

This is consistent with the findings in Section 5.3.1. The 1s emission lifetime in the plasma dominated density regime is identical to the continuum decay at 4 K. At the same time the 1s decay is different, i.e. slower, for lower densities.

This comparison shows that, under suitable conditions, the 1s photoluminescence can be completely dominated by plasma emission, and the spectra can be explained by applying a pure plasma theory. This is the case for all investigated densities at high temperatures as well as more surprisingly at low temperatures for high densities. However, it is also evident that at 4 K and low to intermediate densities, the pure plasma calculation underestimates β . The stronger measured 1s emission is attributed to the presence of incoherent bound exciton populations $\Delta\langle N_X \rangle$.

To test this assumption, optically active $q=0$ excitons are added in the theory. The changes in the spectral shape of the emission can be seen in Figure 6.2. Exemplary calculated photoluminescence spectra for two different carrier densities are shown. All spectra are calculated for a carrier temperature of 16 K. The dashed line shows the KMS result, the theoretical absorption spectrum multiplied by $\exp\{-\Delta E/(k_B \cdot 16 \text{ K})\}$. The pure plasma calculation is shown as a dotted line. The solid line gives the emission spectrum for the combined pure plasma and excitonic contributions.

As can clearly be seen, the 1s photoluminescence can be strongly enhanced by the addition of excitons. An excellent theory-experiment agreement for β for all densities is obtained, as shown in Figure 6.3.

The top graph in Figure 6.4 shows the $q = 0$ excitons necessary for agreement of the experimental and theoretical β versus density curves in Figure 6.3. From this

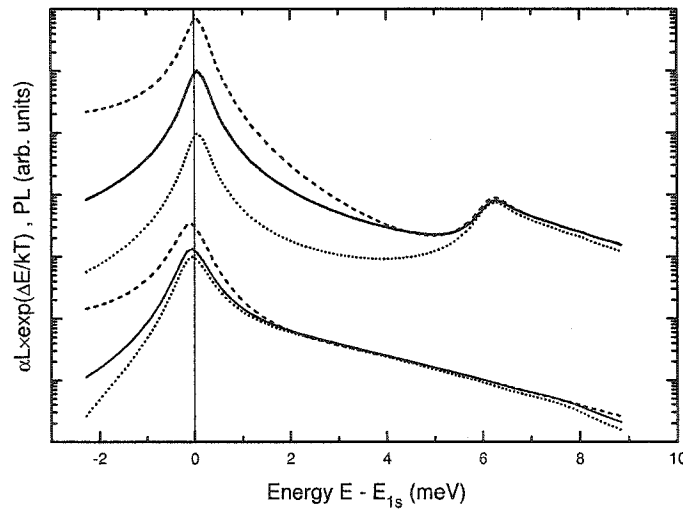


Figure 6.2: Theoretical photoluminescence spectra for two carrier densities ($5.0 \times 10^8 \text{ cm}^{-2}$, top and $1.3 \times 10^{10} \text{ cm}^{-2}$, bottom) and a carrier temperature of 16 K: pure plasma (dotted) and including excitons (solid). The exciton contributions used are as shown in Figure 6.4. The KMS result (dashed) is obtained by multiplying the computed nonlinear αL by the Boltzmann factor.

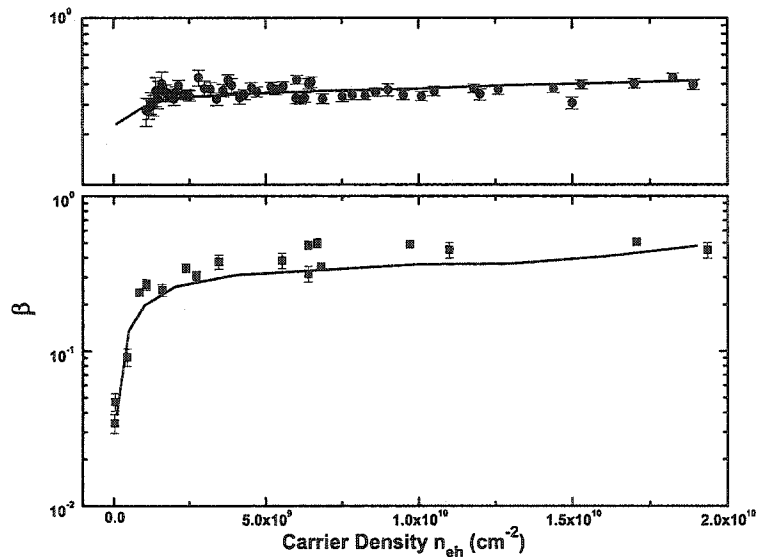


Figure 6.3: β versus carrier density. As in Figure 6.1, the full squares refer to experimental values taken at 1 ns after nonresonant excitation at a lattice temperature of 4 K and the densities refer to densities at 1 ns. The solid line shows a theoretical fit including a $q = 0$ exciton contribution shown in the inset. Top: same for 50 K lattice temperature and extracted e-h plasma temperature of 50 ± 2 K; the theoretical curves are computed for a carrier temperature of 48 K.

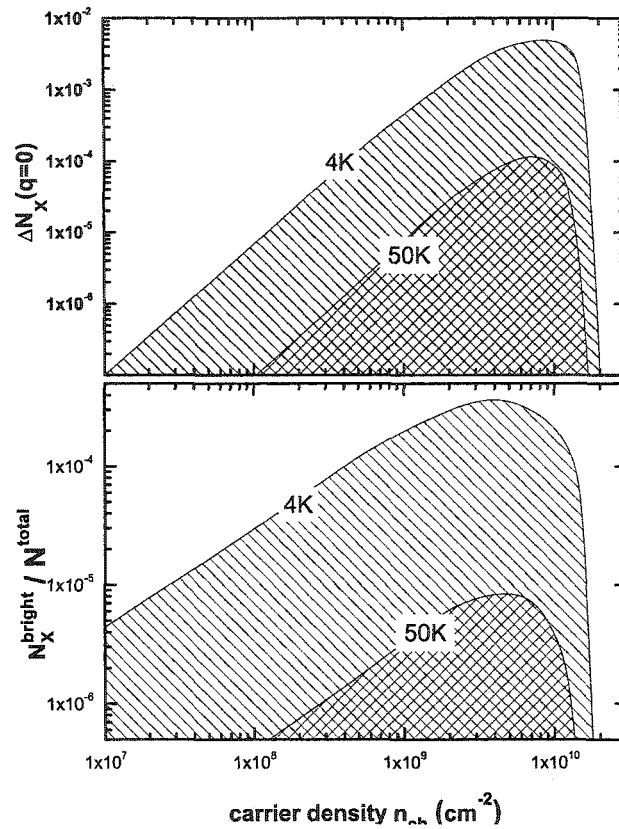


Figure 6.4: Top: Phase diagram of $q = 0$ excitonic contributions as a function of the carrier density on a double-logarithmic scale as used in the fit curve shown in Figure 6.3. Bottom: Phase diagram of bright excitons with $q < q_{\text{photon}}^{\text{max.}}$ as a function of the carrier density on a double-logarithmic scale as used in the fit curve shown in Figure 6.3 extracted from $\Delta N_X(q = 0)$ and Equation 6.2.

can be concluded that the 1s photoluminescence is dominated by the recombination radiation of excitons at low temperatures and for low and intermediate densities. With decreasing carrier density the contributing exciton fraction decreases roughly quadratically, as can be seen in the top graph in Figure 6.4.

Even under favorable conditions, the density of optically active excitons may only be a tiny fraction of the plasma density. It can be calculated by

$$N_X = \frac{1}{4\pi^2} \int_0^{+\infty} \Delta N_X(q) d^2q, \quad (6.1)$$

where $N_X(q)$ is the exciton momentum distribution. When assuming the distribution of excitons as constant for all $q \leq q_{\text{photon}}^{\text{max.}}$ and cylindrical symmetry, one can write

$$N_X^{\text{bright}} \simeq \frac{\Delta N_X(q=0)}{2\pi} \int_0^{q_{\text{photon}}^{\text{max.}}} q dq = \frac{\Delta N_X(q=0)(q_{\text{photon}}^{\text{max.}})^2}{4\pi}. \quad (6.2)$$

The maximum bright photon momentum $q_{\text{photon}}^{\text{max.}}$ is given by $q_{\text{photon}}^{\text{max.}} = \frac{2\pi}{\lambda_0}$. Therefore, $N_X^{\text{bright}} \approx 4.4 \times 10^8 \text{ cm}^{-2} \times \Delta N_X(q=0)$ for $\lambda_0 = 843 \text{ nm}$. This translates to $N_X^{\text{bright}} \approx 1.6 \times 10^6 \text{ cm}^{-2}$ or 0.04% of the density at about $n_{eh} = 4 \times 10^9 \text{ cm}^{-2}$; see bottom graph in Figure 6.4. This is the largest bright exciton fraction in the density range covered here. The number of bright excitons therefore is only a tiny fraction of the total carrier density; it is unknown whether the remaining carriers are bound (dark) excitons or plasma.

It is impossible to deduce any information about the center-of-mass distribution of the excitons from the interband photoluminescence experiments presented here. Photoluminescence is only sensitive to optically active excitons with small momentum. Dark excitons, with $q \geq q_{\text{photon}}$ cannot radiate; in addition, only photoluminescence close to normal can leave the semiconductor due to the large difference in refractive index with respect to air (vacuum). THz absorption measurements directly test the buildup of an excitonic population and are therefore more appropriate to access information about the total exciton number by monitoring induced absorption of the 1s to 2p transition in the far infrared [70]. Quantitative analysis of these spectra yield the absolute exciton fractions.

To get some more accessible figures for the exciton contributions, distribution functions can be postulated. Two exemplary cases are shown in Figure 6.5. When assuming a thermal distribution of 1s excitons at 4 K (solid), the maximum excitonic contribution shown in Figure 6.4 corresponds to a total excitonic fraction of 4%. However, if significant hole burning around $q = 0$ is present, this number would be much larger. The fast radiative lifetime of optically active 1s excitons depletes the distribution for small q (dashed). If the hole in this non-thermal distribution is 10%, the exciton fraction would increase to 40%. In an ideal structure, that is without disorder, the non-thermal distributions and therefore the depth of the hole, can be

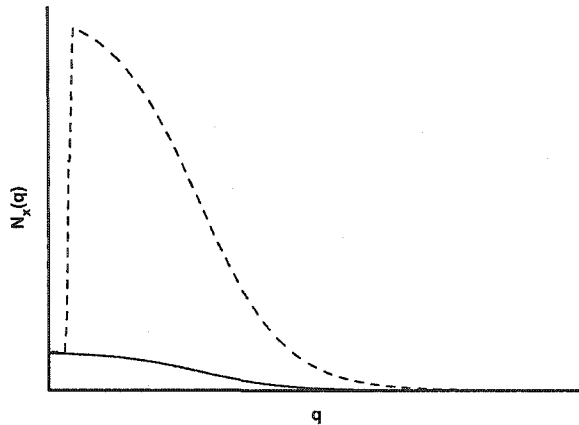


Figure 6.5: Possible distribution functions for excitons. The value of $N_X(q)$ given in Figure 6.4 corresponds to the y-axis crossing of the distribution. No hole burning (solid); hole burning down to 10% (dashed).

calculated [68, 69, 70]. However in real samples, disorder destroys perfect momentum conservation and more momentum states can contribute to the emission.

Exciton formation after nonresonant excitation should be most efficient at intermediate densities. Due to kinetic arguments, at low densities the probability for electron-hole collisions is small. For large densities the Fermionic nature of the constituents comes into play. Exciton binding is hampered by phase space filling effects and screening of the attractive Coulomb interaction.

As shown above, especially towards lower density tiny bright exciton densities dramatically enhance the 1s emission. Consequently, depending upon temperature and density, excitonic luminescence can be almost entirely from the plasma or almost entirely from excitons.

The generally accepted mechanism for exciton formation is three-particle interaction, especially via acoustic phonon assisted processes. An electron and hole can dump excess energy and momentum into the lattice via acoustic phonon interaction; for large enough excess energies also via LO phonons. However, acoustic phonons also play an important role in cooling the hot plasma. This changes its distribution and hence the emission probability for each energy; cooler temperatures favor lower energies. Hence an increase in the 1s photoluminescence may not only track creation

of 1s excitons but can also be caused by cooling. This, together with the conclusions reached in the previous chapter of this dissertation, show that photoluminescence is not an unambiguous tool to study exciton dynamics for all carrier densities and lattice temperatures and has to be treated accordingly.

Even though photoluminescence studies cannot resolve the question concerning the total exciton number and the detailed exciton distribution function, the results clearly show an increased importance of excitons at low lattice temperatures and intermediate and low carrier densities. This observation is in qualitative agreement with exciton formation studies in quantum wires [31].

CHAPTER 7

CONCLUSIONS AND OUTLOOK

Photoluminescence experiments are conducted across a large region of the parameter space of carrier density and lattice temperature. Carefully conducted nonlinear absorption measurements under identical conditions are used for density calibration at the respective times. A carrier temperature T is extracted from the slope of the continuum photoluminescence. At 4 K the carrier temperature T always exceeds the lattice temperature T_L , i.e. the carriers never equilibrate with the lattice. For elevated lattice temperatures > 30 K, the carrier temperature approaches the lattice temperature within the first 100 ps after excitation; i.e. rapid equilibration occurs.

For analysis a factor β is defined as a measure for the 1s peak height corrected for carrier temperature, oscillator strength, and linewidth. The latter causes β to be very robust; different samples with varying broadening, both homogeneous and inhomogeneous, give similar results. The β analysis offers a tool allowing one to estimate the amount of excitons contributing to emission of photoluminescence at the 1s resonance. However, quasi-equilibrium conditions are a mandatory prerequisite for evaluation of the theory to be valid.

The β factor is smaller than 0.5 for all experiments with nonresonant excitation. Accordingly, the thermal equilibrium KMS relation for which $\beta = 1$ is never satisfied. Even if an incoherent excitonic population forms, it is smaller than postulated by the KMS relation at each given temperature; the exciton formation rate is slower than the cooling.

For resonant excitation and 4 K lattice temperature, a β factor larger than 1 is found; more excitons than necessary for thermal equilibrium are present in the system after the fast initial polarization decay. For 30 K lattice temperature, however, the time dynamics of β , as well as of the 1s and continuum-edge luminescence, are

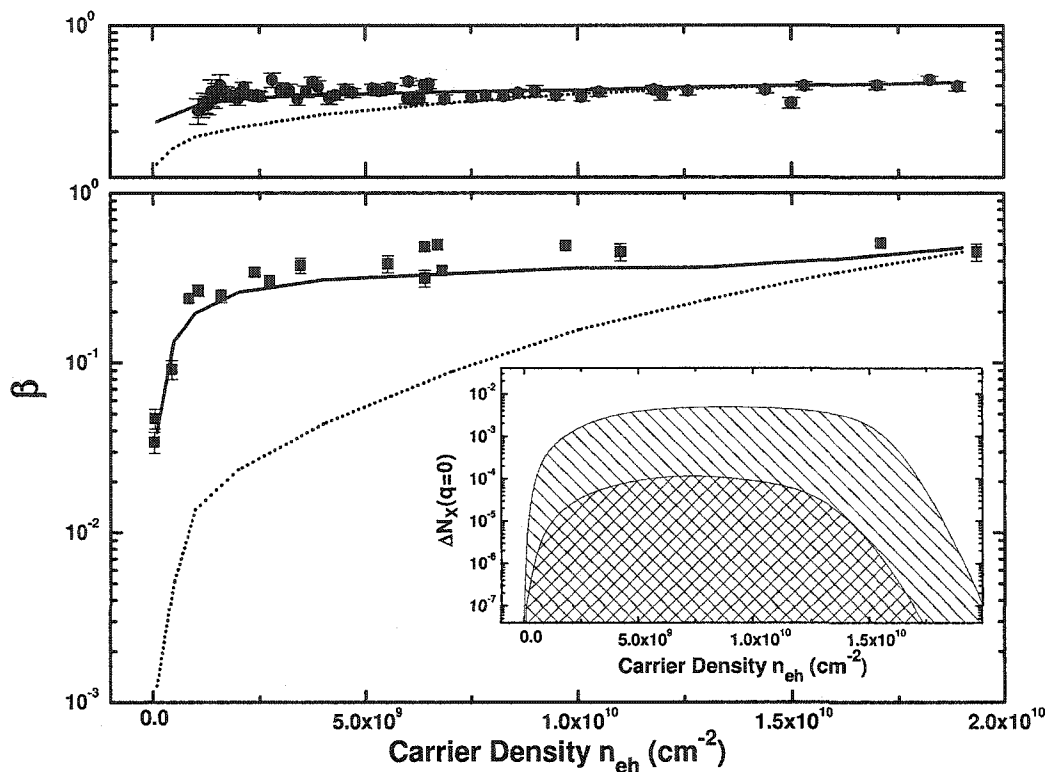


Figure 7.1: Factor β versus carrier density. Full squares refer to experimental values taken at 1 ns after nonresonant excitation at a lattice temperature of 4 K. The densities refer to densities at 1 ns. The theoretical values (dotted line) are calculated using pure e-h plasma theory with carrier temperatures of 14 K for small and 18 K for elevated carrier densities. The solid line shows a theoretical fit using the luminescence formula 2.4 including a $q = 0$ exciton contribution as shown in the inset. Top: the same for 50 K lattice temperature, but data points for all time delays are shown. The extracted e-h plasma temperature is (50 ± 2) K; the theoretical curves are computed for a carrier temperature of 48 K. Inset: Phase diagram of $q = 0$ excitonic contributions as a function of the carrier density.

similar to the nonresonant excitation case. Enough acoustic phonons are present for the excitonic system to become more plasma-like.

The density dependence of β after nonresonant excitation is shown in Figure 7.1; the experimental values are shown as squares. In a first step, these are compared to a pure plasma calculation shown as the dotted curves. The remaining deviations at intermediate and lower carrier densities at 4K lattice temperatures are explained by the presence of incoherent excitons. When these are added into the theory, the experimental values are well described by the full calculation. The inset shows the excitonic contributions necessary to produce the fit. $\Delta N_X(q=0)$ gives the $q=0$ contribution. When calculating the bright excitonic contribution by integrating the exciton momentum distribution $N_X(q)$ for $q \leq q_{\text{photon}}^{\text{max}}$ a maximum bright exciton fraction of less than 0.04% is found.

Exciton formation after nonresonant excitation is most efficient at intermediate densities. Due to kinetic arguments, at low densities the probability for electron-hole collisions is small. For large densities the Fermionic nature of the constituents comes into play. Exciton binding is hampered by phase space filling effects and screening of the attractive Coulomb interaction.

The β analysis, like all photoluminescence based techniques, is only sensitive to optically active excitons with small photon momenta q . To get a definite answer on the questions of exciton formation, it would be necessary to perform additional THz experiments. Their quantitative analysis together with a detailed PL and α L analysis can offer those answers. Accordingly, a region in parameter space can be identified, where excitons not only dominate emission, but also constitute the majority - if not all - of the carriers. Here one can only conclude that the maximum total exciton fraction is less than 4% if radiative decay does not result in a hole in the exciton center-of-mass distribution around zero in-plane momentum. But a hole deep enough that the total exciton fraction is 100% cannot be ruled out.

The appearance of the 1s-exciton resonance in luminescence is ubiquitous and independent of the existence of bound excitons. Due to its large oscillator strength,

it always dominates the spectrum in emission. This is similar to the behavior in absorption, and indeed the mathematical description of luminescence, Equation 2.4, resembles the Elliott formula for absorption. Under suitable conditions excitons form after nonresonant excitation, and a regime of low temperature and intermediate density is identified as most favorable.

In conclusion, by carefully mapping out the parameter space of carrier density and lattice temperature, conditions are identified under which the photoluminescence emission at the 1s resonance after nonresonant excitation into the continuum can be dominated by plasma or excitons. Only for low and intermediate densities at low temperatures, do excitonic populations exist in sufficient numbers to be the main contributor to the emission. In all other cases, namely elevated lattice temperatures and high densities ($> 2 \times 10^{10} \text{ cm}^{-2}$) at low temperatures, the emission is plasma dominated. Even when the 1s emission is monitoring bright excitons, the number of bright excitons is tiny; also the total number of excitons may be much smaller than the plasma density, i.e. the plasma may determine the dynamics.

These results are in agreement with the THz results claiming an excitonic population after 1 ns for elevated carrier densities of $1 \times 10^{10} \text{ cm}^{-2}$. The main advantage of photoluminescence-based techniques is the increased sensitivity; THz experiments are very much limited to high carrier densities due to presently available equipment limitations.

In light of the findings presented in this thesis prior photoluminescence experiments have to be partially reinterpreted. Claims towards excitonic Bose-Einstein condensation may monitor plasma-related phenomena. Photoluminescence studies at densities above $2 \times 10^{10} \text{ cm}^{-2}$, which is still well below transparency, do not allow for a purely excitonic interpretation.

APPENDIX A
LIST OF DATA

Photoluminescence and Absorption Measurements DBR 42, 20 MQW

Date	Pump Excess Energy (ΔE)	Pump Power	Repetition Rate	Lattice Temperature	Comment
030728	1s+13.2 meV	137.0 μ W	1 MHz	4 K	
030401	1s+13.2 meV	3.4 μ W	1 MHz	4 K	
030403	1s+13.2 meV	26.0 μ W	1 MHz	4 K	
030421	1s+13.2 meV	137.0 μ W	1 MHz	4 K	
030422	1s+13.2 meV	70.0 μ W	1 MHz	4 K	
030423	1s+13.2 meV	180.0 μ W	1 MHz	4 K	
030424	1s+13.2 meV	46.0 μ W	1 MHz	4 K	
030426	1s+13.2 meV	26.0 μ W	1 MHz	4 K	
030427	1s+13.2 meV	1.0 μ W	1 MHz	4 K	
030428	1s+13.2 meV	3.6 μ W	1 MHz	4 K	α L OK
030505	1s+13.2 meV	3.5 μ W	1 MHz	4 K	
030506	1s+13.2 meV	6.8 μ W	2 MHz	4 K	α L OK
030508	1s+13.2 meV	3.5 μ W	1 MHz	4 K	
030508b	1s+13.2 meV	6.8 μ W	2 MHz	4 K	comparison
030510	1s+13.2 meV	1.9 μ W	2 MHz	4 K	
030511	1s+13.2 meV	1.0 μ W	2 MHz	4 K	
030513a	1s+13.2 meV	150.0 μ W	2 MHz	4 K	
030513b	1s+13.2 meV	70.0 μ W	2 MHz	4 K	
030513c	1s+13.2 meV	490.0 μ W	2 MHz	4 K	

Date	Pump Excess Energy (ΔE)	Pump Power	Repetition Rate	Lattice Temperature	Comment
030514a	1s+13.2 meV	60.0 μ W	2 MHz	4 K	
030514b	1s+13.2 meV	50.0 μ W	2 MHz	4 K	
030515a	1s+13.2 meV	40.0 μ W	2 MHz	4 K	
030515b	1s+13.2 meV	490.0 μ W	2 MHz	4 K	
030515c	1s+13.2 meV	300.0 μ W	2 MHz	4 K	α L OK
030517a	1s+13.2 meV	25.0 μ W	2 MHz	4 K	
030517b	1s+13.2 meV	10.0 μ W	2 MHz	4 K	
030518b	1s+13.2 meV	490.0 μ W	2 MHz	4 K	
030518c	1s+13.2 meV	0.7 μ W	2 MHz	4 K	
030520a	1s+13.2 meV	250.0 μ W	2 MHz	30 K	
030520b	1s+13.2 meV	20.0 μ W	2 MHz	30 K	
030522a	1s+13.2 meV	5.0 μ W	2 MHz	30 K	
030523a	1s+13.2 meV	500.0 μ W	2 MHz	30 K	
030524a	1s+13.2 meV	2.0 μ W	2 MHz	30 K	
030525a	1s+13.2 meV	80.0 μ W	2 MHz	30 K	
030526a	1s+13.2 meV	400.0 μ W	2 MHz	30 K	
030528a	1s+13.2 meV	20.0 μ W	2 MHz	4 K	
030529a	1s+13.2 meV	20.0 μ W	2 MHz	30 K	
030530a	1s+13.2 meV	20.0 μ W	2 MHz	50 K	
030531a	1s+13.2 meV	20.0 μ W	2 MHz	70 K	
030601a	1s+13.2 meV	20.0 μ W	2 MHz	80 K	
030602a	1s+13.2 meV	20.0 μ W	2 MHz	90 K	
030606a	1s	25.0 μ W	2 MHz	30 K	
030607a	1s	25.0 μ W	2 MHz	4 K	
030608b	1s	25.0 μ W	2 MHz	15 K	

Date	Pump Excess Energy (ΔE)	Pump Power	Repetition Rate	Lattice Temperature	Comment
030626a	1s+13.2 meV	200.0 μ W	2 MHz	80 K	
030626b	1s+13.2 meV	20.0 μ W	2 MHz	80 K	
030626c	1s+13.2 meV	6.25 μ W	2 MHz	80 K	
030626d	1s+13.2 meV	62.5 μ W	2 MHz	80 K	
030801a	1s+37.6 meV	100.0 μ W	2 MHz	4 K	
030801b	1s+37.6 meV	10.0 μ W	2 MHz	4 K	
030801c	1s+32.1 meV	200.0 μ W	2 MHz	4 K	
030801d	1s+32.1 meV	20.0 μ W	2 MHz	4 K	
030801e	1s+24.3 meV	10.0 μ W	2 MHz	4 K	
030801f	1s+24.3 meV	100.0 μ W	2 MHz	4 K	
030801g	1s+19.4 meV	30.0 μ W	2 MHz	4 K	
030801h	1s+19.4 meV	300.0 μ W	2 MHz	4 K	
030801i	1s+8.8 meV	300.0 μ W	2 MHz	4 K	
030801j	1s+8.8 meV	30.0 μ W	2 MHz	4 K	
030626a	1s+13.2 meV	600.0 μ W	2 MHz	60 K	
030626b	1s+13.2 meV	200.0 μ W	2 MHz	60 K	
030626c	1s+13.2 meV	6.0 μ W	2 MHz	60 K	
030626d	1s+13.2 meV	20.0 μ W	2 MHz	60 K	
030626c	1s+13.2 meV	60.0 μ W	2 MHz	60 K	

Photoluminescence and Absorption Measurements DBR 55, SQW

Date	Pump Excess Energy (ΔE)	Pump Power	Repetition Rate	Lattice Temperature	Comment
030619a	1s+13.2 meV	490.0 μ W	2 MHz	4 K	
030619b	1s+13.2 meV	40.0 μ W	2 MHz	4 K	
030619c	1s+13.2 meV	20.0 μ W	2 MHz	4 K	
030619d	1s+13.2 meV	10.0 μ W	2 MHz	4 K	

Photoluminescence and Absorption Measurements DBR 55, 4MQW

Date	Pump Excess Energy (ΔE)	Pump Power	Repetition Rate	Lattice Temperature	Comment
030623a	1s+13.2 meV	420.0 μ W	2 MHz	4 K	
030623a	1s+13.2 meV	40.0 μ W	2 MHz	4 K	

CW Photoluminescence, lattice at 4 K

Date	Pump Excess Energy (ΔE)	Pump Power Range	Sample	Number of wells
030710a	1s+13.8 meV	1 μ W – 10 mW	DBR 13	30
030711a	1s+13.8 meV	300 nW – 10 mW	DBR 18	10
030712c	1s+13.8 meV	1 μ W – 10 mW	DBR 18	10
030712c	1s+17.1 meV	1 μ W – 10 mW	DBR 18	10
030711b	1s+14.1 meV	300 nW – 10 mW	DBR 42	20
030812	1s+14.1 meV	1 μ W – 10 mW	DBR 42	20
030715	1s+14.1 meV	10 μ W – 10 mW	1a1124	10

Absorption Measurements DBR 42, 20 MQW (Blue Shift)

Date	Pump Excess Energy (ΔE)	Pump Power	Repetition Rate	Lattice Temperature	Comment
030610a	1s+13.2 meV	500.0 μ W	2 MHz	4 K	1800l/mm
030610b	1s+13.2 meV	200.0 μ W	2 MHz	4 K	1800l/mm
030610c	1s+13.2 meV	10.0 μ W	2 MHz	4 K	1800l/mm
030610d	1s+13.2 meV	100.0 μ W	2 MHz	4 K	1800l/mm
030611a	1s+13.2 meV	400.0 μ W	2 MHz	4 K	1800l/mm
030611b	1s+13.2 meV	30.0 μ W	2 MHz	4 K	1800l/mm
030611c	1s+13.2 meV	300.0 μ W	2 MHz	4 K	1800l/mm
030611d	1s+13.2 meV	3.0 μ W	2 MHz	4 K	1800l/mm
030611e	1s+13.2 meV	30.0 μ W	2 MHz	4 K	1800l/mm
030611f	1s+13.2 meV	1.0 μ W	2 MHz	4 K	1800l/mm
030612a	1s+13.2 meV	500.0 μ W	2 MHz	4 K	1800l/mm
030612b	1s+13.2 meV	500.0 μ W	2 MHz	15 K	1800l/mm
030612c	1s+13.2 meV	500.0 μ W	2 MHz	30 K	1800l/mm
030807a	1s+13.2 meV	500.0 μ W	2 MHz	4 K	600l/mm
030807b	1s+13.2 meV	100.0 μ W	2 MHz	4 K	600l/mm
030807c	1s+13.2 meV	300.0 μ W	2 MHz	4 K	600l/mm
030807d	1s+13.2 meV	30.0 μ W	2 MHz	4 K	600l/mm

REFERENCES

- [1] Q. T. Vu; H. Haug; W. A. Hügel, S. Chatterjee, and M. Wegener, **85**, 3508 (2000).
- [2] O.D. Mücke, T. Tritschler, M. Wegener, U. Morgner and F.X. Kärtner, *Phys. Rev. Lett.* **87**, 057401 (2001).
- [3] H. Haug and S.W. Koch, “*Quantum Theory of the Optical and Electronic Properties of Semiconductors*”, 3rd edition, World Scientific, Singapore (1994).
- [4] H. Haug, and C. Klingshirn, “*Optical Properties, Part 1*”, C. Klingshirn, editor, in Landolt-Brnstein: Numerical Data and Functional Relationships in Science and Technology - New Series, Condensed Matter, Semiconductor Quantum Structures, Springer-Verlag, Berlin (2001).
- [5] M. Cardona, *J. Appl. Phys.* **32**, 2151 (1961).
- [6] R. Dingle, in “*Advances in Solid State Physics, Vol. XV*”, H. J. Queisser, Editor, Pergamon/Vieweg, Braunschweig (1975).
- [7] R.C. Miller, D. A. Kleinman, W. T. Tsang, and A. C. Gossard, *Phys. Rev. B* **24**, 1134 (1981).
- [8] J. Kusano, Y. Segawa, Y. Aoyagi, S. Namba, and H. Okamoto, *Phys. Rev. B* **40**, 1685 (1989).
- [9] T.C. Damen, J. Shah, D.Y. Oberli, D.S. Chemla, J.E. Cunningham, and J.M. Kuo, *Phys. Rev. B* **42**, 7434 (1990).
- [10] R. Eccleston, R. Strobel, W. W. Rhle, J. Kuhl, B. F. Feuerbacher, and K. Ploog, *Phys. Rev. B* **44**, 1395 (1991).
- [11] P.W.M. Blom, P.J. van Hall, C. Smit, J.P. Cuypers, and J.H. Wolter, *Phys. Rev. Lett.* **71**, 3878 (1993).
- [12] R. Kumar, A.S. Vengurleka, S.S. Prabhu, J. Shah, and L.N. Pfeiffer, *Phys. Rev. B* **54**, 4891 (1996).

REFERENCES – *Continued*

- [13] M. Gulia, F. Rossi, E. Molinari, P. E. Selbmann, and P. Lugli, *Phys. Rev. B* **55**, 16049 (1997).
- [14] S. Nüsse, P. Haring Boliva, H. Kurz, V. Klimov, and F. Levy, *Phys. Rev. B* **56**, 4578 (1997).
- [15] J. Feldmann, G. Peter, E. O. Göbel, P. Dawson, K. Moore, C. Foxon, and R. J. Elliott, *Phys. Rev. Lett.* **59**, 2337 (1987).
- [16] B. Deveaud, F. Clérot, N. Roy, K. Satzke, B. Sermage, and D.S. Katzer, *Phys. Rev. Lett.* **67**, 2355 (1991).
- [17] M. Kira, F. Jahnke, and S.W. Koch, *Phys. Rev. Lett.* **81**, 3263 (1998).
- [18] G. Khitrova, and H.M. Gibbs; F. Jahnke, M. Kira, and S.W. Koch, *Rev. Mod. Phys.* **71**, 1591 (1997).
- [19] R. A. Kaindl, D. Hägele, R. Lövenich, and D.S. Chemla, *Quantum Electronics and Laser Sciences Conference (QELS 2002)*, Postdeadline Paper, QPD11, Optical Society of America, Washington D. C. (2002).
- [20] R. A. Kaindl, M. A. Carnahan, D. Hägele, R. Lövenich, and D. S. Chemla, *Nature* **423**, 734 (2003).
- [21] R. A. Kaindl, M. A. Carnahan, D. Hägele, R. Lövenich, and D. S. Chemla, *Quantum Electronics and Laser Sciences Conference (QELS 2003)*, Technical Digest, Postconference Edition, QFD5, Optical Society of America, Washington D. C. (2003).
- [22] R. A. Kaindl, D. Hägele, M. A. Carnahan, R. Lövenich, and D. S. Chemla, *Phys. Stat. Sol.* **238**, 451 (2003).
- [23] M. A. Carnahan, R. A. Kaindl, D. Hägele, R. Lövenich, and D. S. Chemla, *Quantum Electronics and Laser Sciences Conference (QELS 2003)*, Postdeadline Paper, QPD11-1, Optical Society of America, Washington D. C. (2003).

REFERENCES – *Continued*

- [24] R. Chari, I. Galbraith, J. Phillips, S. Pellegrini, C.J. Dent A.K. Kar, G.S. Buller, C.R. Pidgeon, D.G. Clarke, B.N. Murdin, J. Allam, A. F. G. van der Meer, and G. Strasser, *Quantum Electronics and Laser Sciences Conference (QELS 2002)*, Postdeadline Paper, Optical Society of America, Washington D. C. (2002).
- [25] G.R. Hayes, and B. Deveaud, *Phys. Stat. Sol. A* **190**, 637 (2002).
- [26] W. Hoyer, “*Quantentheorie zu Excitonenbildung und Photolumineszenz in Halbleitern*”, Dissertation, Phillips-Universität Marburg, Marburg (2003).
- [27] D.F. Dubois, in “*Lectures in Theoretical Physics IX C. Kinetic Theory*”, edited by W. E. Brittin, A. O. Barut, and M. Guenin, Gordon and Breach, New York (1967).
- [28] M. Kira, F. Jahnke, S.W. Koch, J.D. Berger, D.V. Wick, T.R. Nelson, Jr., G. Khitrova, and H. M. Gibbs, *Phys. Rev. Lett.* **79**, 5170 (1997).
- [29] M. Kira, F. Jahnke, W. Hoyer, and S.W. Koch, “*Quantum theory of spontaneous emission and coherent effects in semiconductor microstructures*”, *Prog. in Quant. Electr.* **23**, 189 (1999).
- [30] W. Hoyer, M. Kira and S. W. Koch, *Phys. Stat. Sol. B* **234**, 195 (2002).
- [31] W. Hoyer, M. Kira and S. W. Koch, *Phys. Rev. B* **67**, 155113 (2003).
- [32] H. Stolz, *Einführung in die Vielelektronentheorie der Kristalle*, Bertelsmann Universitätsverlag, Düsseldorf (1975).
- [33] R. J. Elliott, *Phys. Rev.* **108**, 1384 (1957).
- [34] H. F. Hess, E. Betzig, T. D. Harris, L. N. Pfeiffer, K. W. West, *Science* **264**, 1740 (1994).

REFERENCES – *Continued*

- [35] J.R. Guest, T.H. Stievater, X. Li, J. Cheng, D.G. Steel, D. Gammon, D.S. Katzer, D. Park, C. Ell, A. Thränhardt, G. Khitrova, and H.M. Gibbs, *Phys. Rev. B* **65**, 241310 (2002).
- [36] C. Weisbuch, R.C. Miller, R. Dingle, A.C. Gossard, and W. Wiegmann, *Solid State Commun.* **37**, 219 (1981).
- [37] G. Bastard, C. Delalande, M.H. Meynadier, P.M. Frijlink, and M. Voos, *Phys. Rev. B* **29**, 7042 (1984).
- [38] W. Langbein, J.M. Hvam, and R. Zimmermann, *Phys. Rev. Lett.* **82**, 1040 (1999).
- [39] S. Adachi, *“Physical Properties of III-V Semiconductor Compounds”*, John Wiley & Sons, New York (1992).
- [40] *“Properties of Lattice-Matched and Strained Indium Gallium Arsenide”*, P. Bhattacharya, Editor, in *Electronic Materials Information Services (EMIS) Data review Series*, INSPEC, the Institution of Electrical Engineers, London (1993).
- [41] M. Hübner, J.P. Prineas, C. Ell, P. Brick, E. S. Lee, G. Khitrova, H. M. Gibbs, and S. W. Koch, *Phys. Rev. Lett.* **83**, 2841 (1999).
- [42] J.P. Prineas, J. Shah, B. Grote, C. Ell, G. Khitrova, H.M. Gibbs, and S.W. Koch, *Phys. Rev. Lett.* **85**, 3041 (2000).
- [43] J.P. Prineas, C. Ell, E. S. Lee, G. Khitrova, H. M. Gibbs, and S.W. Koch, *Phys. Rev. B* **61**, 13863 (2000).
- [44] B. Grote, C. Ell, S.W. Koch, G. Khitrova, H.M. Gibbs, J.P. Prineas, and J. Shah, *Phys. Rev. B* **64**, 045330 (2000).
- [45] R. Kubo, *J. Phys. Soc. Japan* **12**, 570 (1957).
- [46] P.C. Martin, and J. Schwinger, *Phys. Rev.* **115**, 1342 (1959).

REFERENCES – *Continued*

- [47] R. F. Schnabel, R. Zimmermann, D. Bimberg, H. Nickel, R. Lösch, and W. Schlapp, *Phys. Rev. B* **46**, 9873 (1992).
- [48] W. Hoyer, M. Kira, S. W. Koch, P. Brick, S. Chatterjee, C. Ell, G. Khitrova, and H. M. Gibbs, *OSA Trends in Optics and Photonics (TOPS) 57 Quantum Electronics and Laser Sciences Conference (QELS 2001)*, Technical Digest, Post-conference Edition, Optical Society of America, Washington D. C. (2001).
- [49] P. Brick, “*Coherent Optical Nonlinearities in Semiconductor Microstructures*”, Ph.D. Dissertation, Optical Sciences Center, The University of Arizona, Tucson (2001).
- [50] C. F. Klingshirn, “*Semiconductor Optics*”, corrected printing Springer-Verlag, Berlin (1997).
- [51] Supplied by W. Ceislik of Hamamastu Inc. (1999).
- [52] N. Peyghambarian, H. M. Gibbs, J. L. Jewell, A. Antonetti, A. Migus, D. Hulin, and A. Mysyrowicz, *Phys. Rev. Lett.* **53**, 2433 (1984).
- [53] D. Hulin, A. Mysyrowicz, A. Antonetti, A. Migus, W. T. Masselink, H. Morkoç, H. M. Gibbs, and N. Peyghambarian, *Phys. Rev. B* **33**, 4389 (1986).
- [54] D. R. Wake, J. P. Wolfe, and H. Morkoç, *Phys. Rev. B* **46**, 13452 (1992).
- [55] G. Manzke, Q. Y. Peng, K. Henneberger, U. Neukirch, K. Hauke, K. Wundke, J. Gutowski, and D. Hommel, *Phys. Rev. Lett.* **80**, 4943 (1998).
- [56] W. H. Knox, C. Hirlimann, D. A. B. Miller, J. Shah, D. S. Chemla, and C. V. Shank, *Phys. Rev. Lett.* **56**, 1191 (1986).
- [57] W. H. Knox, D. S. Chemla, G. Livescu, J. E. Cunningham, and J. E. Henry, *Phys. Rev. Lett.* **61**, 1290 (1988).
- [58] K. Leo, W. W. Rühle, H. J. Queisser, and K. Ploog, *Phys. Rev. B* **37**, 7121 (1988).

REFERENCES – *Continued*

- [59] H. W. Yoon, D. R. Wake, and J. P. Wolfe, *Phys. Rev. B* **54**, 2763 (1996).
- [60] D. Y. Oberli, D. R. Wake, M. V. Klein, J. Klem, T. Henderson, and H. Morkoç, *Phys. Rev. Lett.* **59**, 696 (1987).
- [61] L. Bányai, D. B. T. Thoi, E. Reitsamer, H. Haug, D. Steinbach, M. U. Wehner, M. Wegener, T. Marschner, and W. Stolz, *Phys. Rev. Lett.* **75**, 2188 (1995).
- [62] E. W. van Stryland, M. A. Woodall, H. Vanherzeele, and M. J. Soileau, *Opt. Lett.* **10**, 490 (1985).
- [63] A. Vinattieri, J. Shah, T. C. Damen, D. S. Kim, L. N. Pfeiffer, M. Z. Maialle, and L. M. Sham, *Phys. Rev. B* **50**, 10868 (1994).
- [64] W. Chow, M. Kira, and S. W. Koch, *Phys. Rev. B* **60**, 1947 (1999).
- [65] K. Siantidis, V. M. Axt, and T. Kuhn, *Phys. Rev. B* **65**, 035303 (2001).
- [66] A. Thränhardt, S. Kuckenburg, A. Knorr, T. Meier, and S. W. Koch, *Phys. Rev. B* **62**, 2706 (2000).
- [67] A. Thränhardt, S. Kuckenburg, A. Knorr, P. Thomas, and S. W. Koch, *Phys. Rev. B* **62**, 16802 (2000).
- [68] C. Piermarocchi, F. Tassone, V. Savona, A. Quattropani, and P. Schwendimann, *Phys. Rev. B* **53**, 15834 (1996).
- [69] I.-K. Oh, J. Singh, A. Thilagan, and A. S. Vengurleka, *Phys. Rev. B* **62**, 2045 (2000).
- [70] M. Kira, W. Hoyer, T. Stroucken, and S. W. Koch, *Phys. Rev. Lett.* **87**, 176401 (2001).